
Electronic Thesis and Dissertation Repository

9-12-2018 1:00 PM

Mapping Debris Disks at extreme contrast: near-IR Polarimetric Differential Imaging with the Gemini Planet Imager.

Juan Sebastian Bruzzone
The University of Western Ontario

Supervisor
Metchev, Stanimir A.
The University of Western Ontario

Graduate Program in Astronomy
A thesis submitted in partial fulfillment of the requirements for the degree in Doctor of Philosophy
© Juan Sebastian Bruzzone 2018

Follow this and additional works at: <https://ir.lib.uwo.ca/etd>



Part of the [Stars, Interstellar Medium and the Galaxy Commons](#)

Recommended Citation

Bruzzone, Juan Sebastian, "Mapping Debris Disks at extreme contrast: near-IR Polarimetric Differential Imaging with the Gemini Planet Imager." (2018). *Electronic Thesis and Dissertation Repository*. 5917. <https://ir.lib.uwo.ca/etd/5917>

This Dissertation/Thesis is brought to you for free and open access by Scholarship@Western. It has been accepted for inclusion in Electronic Thesis and Dissertation Repository by an authorized administrator of Scholarship@Western. For more information, please contact wlsadmin@uwo.ca.

Abstract

Debris disks are gas-poor evolved circumstellar disks that show decreased near- to mid-infrared thermal excess emission because of lack of material close to the star. Regarded as massive analogues to the Main Asteroid or Kuiper Belts in the Solar System, these often young dust-rich disks comprise second-generation dust created by disruptive collisions of planetesimals and the decay products of asteroids and comets. Of the dozen or so directly imaged planets to date many share a distinctive characteristic: they reside in stellar systems known to also possess circumstellar dust. High-angular resolution characterization of debris disks, whose morphology is thought to be affected by embedded orbiting planets, offers an important pathway for probing planet-disk interaction.

I used polarimetric differential imaging (PDI) to characterize debris disks at 0.042'' resolution with the Gemini Planet Imager (GPI) on the Gemini South 8 m telescope. For the first project, I determined the photometric response of polarimetric observations with the GPI leading to the flux calibration of the instrument. In my second and third project, I demonstrated the utility of PDI with radiative transfer modeling tools to characterize the morphology and grain properties of two debris disks at solar system scales. I reported the first PDI observations of the inner Kuiper Belt-analog HD 141569A disk and revealed the presence of an spiral arm. I also determined the existence of a putative unseen innermost disk inwards of 30 AU around HD 141569A through the analysis of the predicted thermal emission of the disk. Finally, I mapped the structure of the 82 AU ring-shaped HD 157587 debris disk. Our multi-wavelength high-contrast polarimetry reveals that even this unusually old (> 1 billion years) debris disk contains short-lived small grains: evidence of an active collisional cascade in this system. The combined power of extreme contrast ($\sim 1 : 1,000,000$ at 1 arc second), high angular resolution, and differential polarimetry with the Gemini Planet Imager reveals previously unseen disk structures, and is of great value for studying dynamically perturbed disks.

Keywords: debris disks, polarimetry, direct imaging

Co-Authorship Statement

This Thesis is comprised of three independent manuscripts (Sections 2, 3, and 4). I am second author on the first manuscript, and the lead author on the latter two. The first has been published as Hung, Bruzzone et al. (2016, SPIE, 9908, 99083A), the second has been submitted and already been peer-reviewed for the *Astronomical Journal*, and the third is to be submitted.

The first manuscript presents a combined study of two independent calibrations of the flux response of the Gemini Planet Imager in polarimetry mode: one by lead-author Li-Wei Hung at UCLA, and one by me at UWO. My own write-up of the calibration was distributed as an internal report to the Gemini Planet Imager Exoplanet Survey (GPIES) collaboration, and is reproduced in full in Appendix A. Regarding the published version of the calibration in Hung, Bruzzone et al. (2016), my contribution included:

1. the creation and testing of a Gemini Planet Imager Data Reduction Pipeline (GPI DRP) primitive (a script) to perform aperture photometry on the auxiliary GPI satellite spots faint off-axis images of the bright occulted on-axis star designed for photometric and astrometric calibration;
2. use of the primitive to calibrate the polarimetric flux response of GPI to the previously established spectroscopic response;
3. measurement of the overall instrument throughput;
4. assessing the variations of the GPI satellite spot brightness for the purpose of photometric calibration.

I designed the primitive to comply with the coding structure of the GPI DRP. The definition of the apertures (size and location) was written by Jason Wang with hard-coded values such as position, separation and size. My work started writing a script that would instead derive such values from design principles of the instrument, such as the grid spacing of the apodizer in *H* band. The script allowed to consistently perform aperture photometry within the DRP. My

study showed for the first time the biases between the two available flux extraction algorithms in polarimetry mode. This highlighted how extraction algorithms impacted flux measurements and the relative calibration with spectroscopy mode. I also showed the first measurement of instrument throughput and provided a comprehensive test of satellite spot flux variability in polarimetry mode. Other features of the script I wrote were adapted as stand-alone scripts within the DRP. As example, a script to perform companion photometry in polarimetry mode. This was used to compute satellite:companion flux ratios. Sections 2.0, parts of Section 3.2 and 3.3, and Section 4 in that paper (Chapters 2.2, 2.2.3, 2.3.3 and 2.4 in this Thesis) are based on my work.

My contribution to the GPI DRP and the GPI polarimetry mode calibration is acknowledged through co-authorship on 7 other peer-reviewed papers from the GPIES collaboration. The following authors contributed to Chapter 1: Stanimir Metchev provided comments.

The following authors contributed to Chapter 2: Jason Wang wrote the satellite spot aperture shapes. Maxwell Millar-Blanchaer provided the initial setup and substantial guidance explaining polarimetric observations with GPI in detail. M. M-B. also tested versions of the code and helped troubleshoot issues with data reduction. Li-Wei Hung derived the photometry calibration into Jy. Stanimir Metchev provided guidance throughout the duration of the project.

The following authors contributed to Chapter 3: Stanimir Metchev provided extensive guidance and insightful comments throughout the duration of the project. Gaspard Duchene provided the executable version of MCFOST and the SED fitting code. G.D. also provided insightful discussions that enriched the project. Maxwell Millar-Blanchaer provided comments and suggestions. Jason Wang wrote the pyKLIP module. James Graham revised an earlier manuscript and provided insightful comments.

The following authors contributed to Chapter 4: Stanimir Metchev provided guidance and part of the analysis generating the photometry of the HD 157587 disk. Gaspard Duchene provided the executable version of MCFOST. Thomas Esposito provided guidance setting up the Markov-Chain Monte Carlo code with MCFOST and Schuyler Wolf wrote the python module

that generates MCFOST files. Pauline Arriaga provided guidance with pyKLIP+ADI. Jason Wang and Eric Nielsen provided comments on the astrometry of the point-source candidates. The following authors contributed to Chapter 5: Stanimir Metchev provided comments.

Acknowledgments

I would like to thank my supervisor, Prof. Stanimir Metchev for his patience and much guidance throughout the past four years. The constant pressure and high expectations made me understand the sort of caliber required to become a much better scientist. I would also want to thank fellow members of the GPI team: Maxwell Millar-Blanchaer, Gaspard Duchene, Jason Wang, Schuyler Wolff, Thomas Esposito and Pauline Arriaga for their help. I would like to extend my gratitude to my friends at UWO, past and current office-mates: Quanzhi Ye, Robert Weryk, Edward Stokan, Dilini Subasingue, Maryam Tabeshian, Richard Bloch, Megan Tannock and Paulo Miles-Paez. I want to thank the team at Saint Joseph's Diabetes Support Program for their support these past three years. Thanks to Dr. Beth Urek for her advice and long discussions. Last but not least, this would have not been possible without the love of my life, Carolina, who encouraged me to keep going forward, gracias mi vida.

Para mamá, mi viejo y Mauri.

Contents

Certificate of Examination	i
Abstract	i
Co-Authorship Statement	ii
List of Figures	xii
List of Tables	xv
List of Appendices	xvi
List of Abbreviations and Symbols	xvi
1 Background Material	1
1.1 Introduction	1
1.2 Unresolved Observations of Debris Disks	4
Fundamental Parameters	4
Estimates versus Observations	7
1.3 Evolution of Debris Disks	7
1.3.1 From Protoplanetary Disks to Debris Disks	7
1.3.2 Dust from Planet Formation Processes	10
1.4 Disk Morphologies and the Use of Spatially Resolved Polarimetry	11
1.4.1 Disk Morphology	11

1.4.2	Polarimetry	15
1.4.3	Stokes Parameters, Stokes Vector and Mueller Formalism	15
1.4.4	Differential Polarimetry	18
1.4.5	Insight into Physical Properties from Polarimetry	19
1.5	Observational Methods I	22
1.5.1	Coronagraphic Observations	22
1.5.2	Speckle noise	23
1.5.3	Adaptive Optics (AO) Design	24
	Wavefront Sensing	24
	Deformable Mirrors	26
1.5.4	ExAO implementations: GPI	28
1.6	Observational Methods II: Polarimetry with High-contrast Imaging	30
1.6.1	Polarimetry with GPI: Polarization signal	30
1.7	Questions for this Thesis	32
2	Photometric Calibration of the GPI in Polarimetry Mode	38
2.1	Introduction	39
2.2	Satellite Spot Flux Measurement in Polarimetry Mode	41
2.3	Calibration Using the Satellite Spots Directly	43
2.3.1	Calibration Method	43
2.3.2	Calibration Uncertainty	44
2.3.3	GPI Data Reduction Pipeline Implementations	47
2.3.4	Photometry of HD 19467 B	47
2.3.5	Photometry of Beta Pictoris b	48
2.3.6	Detection throughput Correction	51
2.4	Calibration Using Spectroscopic Observations	52
2.4.1	Calibration Method	53
2.4.2	Scaling Factor	54

2.5	Summary and Future Work	56
2.6	Acknowledgments	57
3	The HD 141569A debris ring with GPI Polarimetry	60
3.1	Introduction	61
3.2	Observations	63
3.3	Results	65
3.3.1	Polarized Intensity H-band Image	65
3.3.2	Total Intensity H-band Image	67
3.4	Disk Modeling	68
3.4.1	Parameterization of the Dust Model	68
3.4.2	Polarized Scattered Light Modeling and Best Fit Estimates	71
3.4.3	Comparison of the Scattered Light Model to the SED	76
3.5	Discussion	78
3.5.1	Morphology of the HD 141569A Inner Disk in Polarized Scattered Light: Comparison to Previous Observations	78
3.5.2	The Arc-like Structure: Spiral Arm?	80
3.5.3	Disk Opening Angle	83
3.5.4	Independent Constraint on the Minimum Grain Size from Polarimetry	84
3.5.5	An Unseen Innermost (Fourth) Ring	85
3.6	Conclusion	86
3.6.1	Acknowledgments:	87
4	Collisional Cascade on the old HD 157587 debris disk	92
4.1	Introduction	93
4.2	Observations	95
4.2.1	Observations in Polarimetry Mode	95
4.2.2	Observations in Spectroscopy Mode	97

4.3	Results	98
4.3.1	Polarized Intensity Images	98
4.3.2	Total Intensity Images	100
4.3.3	Disk Colors	102
4.4	Disk Modeling	104
4.4.1	Parametrization of the Dust Model	104
4.4.2	Modeling Procedure and Best-Fit Estimates	106
4.4.3	A Second Family of Solutions	109
4.5	Discussion	112
4.5.1	Disk Brightness Asymmetries	112
4.5.2	Small and Large Grains	112
4.5.3	A Bright Old Debris Disk	114
4.6	Conclusion	115
4.6.1	Acknowledgments	115
5	Conclusions.	121
5.1	Thesis Summary	123
5.2	Future Work	126
5.2.1	Photometric Calibration of GPI in the <i>J</i> and <i>K1</i> bands in Polarimetry Mode	126
5.2.2	Debris Disk Observations	127
A	Appendix.	128
A.1	Methodology	128
A.2	Results	133
A.2.1	Satellite Spot and Companion pol:spec total flux ratios	133
	BOX and PSF	133
	Pol:Spec ratios	134

Interpolating Bad Pixels in Cube: OLD and NEW Methods	140
A.2.2 Flat Fields	144
Short term variability of total Satellite Spot Fluxes	146
A.3 Conclusions	147
Curriculum Vitae	151

List of Figures

1.1	Fraction of sun-like stars with NIR excesses.	8
1.2	The evolution of disk mass.	10
1.3	HR 4796A with SPHERE.	12
1.4	HR 4796A with GPI polarimetry.	12
1.5	The HD 131835 and HD 35841 disks seen through GPI polarimetry	13
1.6	Hubble observations of debris disks.	13
1.7	GPI disk observations	14
1.8	Scattered-induced polarization Vs. scattering angle.	20
1.9	Polarization dependence with grain properties.	21
1.10	The Lyot coronagraph.	23
1.11	Schematics of a Shack-Hartmann sensor.	25
1.12	AO system loop.	27
1.13	The GPI Apodizer.	28
1.14	Schematics of the GPI polarimeter.	30
2.1	HD 118666 with GPI polarimetry.	41
2.2	Companion:satellite spot flux ratio of HD 19467	45
2.3	Photometrically calibrated measurements of HD 19467 B observations.	49
2.4	<i>H</i> -band photometry of β Pictoris b.	50
3.1	The HD 141569A disk in linear polarization with GPI polarimetry.	66
3.2	SNR maps of the HD 141569A disk.	67
3.3	pyKLIP+ADI reduction the HD 141569A disk in total intensity.	67

3.4	Modeling of the inner HD 141569A dust ring with MCFOST.	72
3.5	Radial profiles of the Stokes Q_r and best-fit models of HD 141569A.	74
3.6	Normalized probability density distributions.	75
3.7	Measured data points and predicted MCFOST SEDs.	77
3.8	Revealing a southern arc on the 44 AU ring around HD 141569A.	82
4.1	The HD 157587 disk with GPI polarimetry in the J , H and $K1$ bands.	98
4.2	SNR maps of the HD 157587 in the J,H and $K1$ bands.	100
4.3	pyKLIP+ADI reductions of the HD 157587 disk at J,H and $K1$	100
4.4	Photometry maps of the HD 157587 disk at J , H and $K1$	102
4.5	Modeling the HD 157587 disk with MCFOST.	106
4.6	Marginalized posterior probability distributions.	108
4.7	Modeling the HD 157587 disk with large ($\sim 30\mu\text{m}$ – $70\mu\text{m}$) grains.	110
4.8	Best-fit linear combination parameter.	110
4.9	The best-fit linear combination of models.	111
5.1	H -band satellite spot apertures in J -band apodizer.	126
A.1	Satellite spot apertures in GPI polarimetry mode.	131
A.2	Reduced GPI podc cube of laboratory data.	132
A.3	Flux variability of HIP 70931b.	136
A.4	Average total satellite spot flux Vs. stellar H band magnitude in polarimetry mode.	139
A.5	Average total satellite spot flux Vs stelalr H band magnitude in spectroscopy mode.	142
A.6	Satellite spot flux Vs 2MASS fluxes.	143
A.7	Raw GCAL Flat mean flux in spectroscopy mode.	145
A.8	Mean flux of reduced GCAL Flats in spectroscopy mode.	146
A.9	GPI photometry in spectroscopy and polarimetry mode.	148

A.10 GPI photometry in spectroscopy and polarimetry mode.	149
A.11 GPI photometry in spectroscopy and polarimetry mode.	150

List of Tables

1.1	Blackbody debris disk radius Vs. observed radius.	7
2.1	GPI satellite spot flux ratios in polarimetry and spectroscopy mode.	55
2.2	Companion flux ratios in polarimetry and spectroscopy mode.	55
3.1	Disk model parameters and best-fit values.	69
4.1	HD 157587 disk Stokes colors.	103
4.2	Disk model parameters and best-fit values.	104
A.1	Science targets and laboratory observations with GPI in polarimetry and spectroscopy mode. Total pol:spec ratios of the total satellite spot fluxes with σ as the standard deviation of the measurements. We included values retrieved from the two extraction algorithm available in polarimetry mode, BOX and PSF	135
A.2	Science targets observed with GPI polarimetry.	137
A.3	Science targets and laboratory measurements with GPI spectroscopy and polarimetry.	140
A.4	Relative standard deviation of satellite spot fluxes in spectroscopy and polarimetry mode.	147

List of Abbreviations and Symbols

ADI	Angular Differential Imaging
ALMA	Atacama Large Millimeter Array
AO	Adaptive Optics
AOWFE	Adaptive Optics Wavefront Error
APLC	Apodized-pupil Lyot coronagraph
CCD	Charge-Coupled Device
CIAO	Coronagraphic Imager with Adaptive Optics
CPU	Central Processing Unit
DIMM	Differential Image Motion Monitor
DM	Deformable Mirror
DRP	Data Reduction Pipeline
FWHM	full width at half maximum
GCAL	Gemini Facility Calibration Unit
GPI	Gemini Planet Imager
GPIES	Gemini Planet Imager Exoplanet Survey
HiCIAO	High-contrast Coronagraphic Imager with Adaptive Optics
HOWFS	High-Order Wavefront Sensor
HST	Hubble Space Telescope
HWP	half-wave plate
IFS	Integral Field Spectrograph
IFSD	Integral Field Spectrograph Dewar
IR	Infrared
IRAS	InfraRed Astronomical Satellite
ISO	Infrared Space Observatory
KBO	Kuiper Belt Object

KLIP	Karhunen-Love Image Processing
LOCI	Locally Optimized Combination of Images
LOWFS	Low-Order Wavefront Sensor
MagAO	Magellan Adaptive Optics
MASS	Multi-Aperture Scintillation Sensor
mas	milliarcsecond
NE	north-eastern
NICI	Near-Infrared Camera Imager
NICMOS	Near-Infrared Camera and Multi-Object Spectrograph
NIR	near-infrared
NSF	National Science Foundation
PDI	Polarimetric Differential Imaging
P-R	Poynting-Robertson
PODC	Polarimetry Data Cube
PSF	Point Spread Function
RMS	root mean square
SED	Spectral Energy Distribution
SHWFS	Shack-Hartmann Wavefront Sensor
SPDC	Spectroscopy Data Cube
SPHERE	Spectro-Polarimetric High-contrast Exoplanet REsearch
SW	south-western
WISE	Wide-field Infrared Survey Explorer
ExAO	Extreme Adaptive Optics

Chapter 1

Background Material

1.1 Introduction

Circumstellar disks surrounding many pre-main sequence stars comprise one of the most sought-after topics in current astronomy research. Gas- and dust-rich disks are created as the inevitable consequence of angular momentum conservation during the star formation process, carrying the ingredients within to form planets. Models and observations suggest that the gas component of these protoplanetary disks clears in a few millions of years leaving planetesimals that constitute an early generation of the dusty disks we want to study. These second generation disks arise as the decay of planetesimals, asteroids and comets through various mechanisms, and their study help constrain models of planetary formation as useful snapshots at different stages of the evolution of young planetary systems. Unseen companions can be inferred from the morphology of the disks materialized as gaps shepherded by planets, warps and density enhancements. In this thesis we will focus on the dusty disks surrounding young stars and will distinguish them from the protoplanetary disks. These dust-rich disks are known as debris disks.

The first extrasolar debris disk was detected in Vega in 1983 ([Aumann et al., 1984](#)) with the Infrared Astronomical Satellite (IRAS) as a strong excess in thermal emission beyond $12\mu\text{m}$.

Since then, the majority of debris disks around stars were revealed as an excess of thermal emission in the far and mid-IR in the spectral energy distribution (SED) of the stars, consequence of the warm dust heated typically around 50-120 K. This of course did not require the disks to be resolved, and proved for decades to be one important tool for diagnostic of these systems.

The excesses identified in a handful of bright nearby stars in 1983 prompted the discovery of disk-like structures around β Pictoris in scattered light, setting a precedence for the first resolved debris disk in coronagraphic observations (Smith & Terrile, 1984). What followed was more than 500 stars surveyed with a significant number of these Vega-like sources harboring debris disk (Oudmaijer et al., 1992; Mannings & Barlow, 1998). Efforts gained momentum as new space-borne observatories were deployed covering the near and far-IR: NICMOS at Hubble, The Infrared Space Observatory (ISO; Kessler et al., 1996), The Spitzer Space Telescope (Spitzer; Werner et al., 2004), (Akari; Murakami et al., 2007), (Herschel; Pilbratt et al., 2010) and The Wide-field Infrared Survey Explorer (WISE; Wright et al., 2010)). On the ground, instruments like (SCUBA; Holland et al., 1999) and (SCUBA-2; Holland et al., 2013) were commissioned to look at the sub-millimeter part of the spectrum.

Work in this field continued but it was not until a few years back that astronomers started successfully imaging nearly a dozen of these debris disks in scattered light providing a different pictorial description of these objects, (Kalas, 2005; Kalas et al., 2007). In recent years, we have seen new high-angular resolution instruments proving the feasibility to image debris disks: (ALMA; ALMA Partnership et al., 2015) in sub-millimeter and The Near Infrared Camera at Gemini South (NICI; Liu et al., 2010), the Coronagraphic Imager with Adaptive Optics (CIAO; Murakawa et al., 2004) at Subaru, followed later by HiCIAO (Suzuki et al., 2010) and MagAO at Las Campanas (Morzinski et al., 2014) in the near IR. Since 2014 however, two new instruments were commissioned that are certainly game changers. The Gemini Planet Imager (GPI; Macintosh et al., 2008) on Gemini South 8m telescope and the Spectro Polarimetric High contrast Exoplanet REsearch (SPHERE; Beuzit et al., 2008) at VLT represent the-state-of-the-

art of modern capabilities to image young gas giant planets and debris disks. Both instruments are spectro polarimeters that can operate as coronagraphs or direct imaging devices featuring extreme adaptive optic (ExAO) systems. Polarimetry of nearby debris disks is a natural extension of previous high-contrast imaging work, and offers an important advantage. Light from the host star is randomly polarized, hence no polarization state is preferred. However, light scattered by the dust grains acquires a linear polarization state and simultaneous observations of both its components lies at the core of modern techniques of high-contrast imaging with coronagraphs. Instruments such as CIAO, HiCIAO and The Extreme Polarimeter (ExPo; [Rodenhuis et al., 2012](#)) at William Herschel Telescope are just a few examples preceding GPI and SPHERE. As of May 2018, around 96¹ debris disks have been resolved between visible and millimeter wavelengths. Of these, about two dozen have been resolved through differential high-contrast polarimetry, which is the most sensitive approach to spatially resolving tenuous amounts of optically thin circumstellar dust.

Debris disks are analogues of the population of planetesimals and interplanetary dust particles in the Solar System. These range from 2000 km down to a few microns in size, and carry clues to the early evolution of the Solar System (e.g. [Wood, 1988](#); [Lissauer, 1993](#); [Bottke et al., 2005](#); [Morbidelli et al., 2007](#)). Most of the small rocky and icy bodies, in the form of asteroids and comets, reside within 50 AU from the Sun in the Main Asteroid and Kuiper Belts. These are the source of the smaller dust grains that comprise the Solar System zodiacal dust cloud.

Zodiacal dust is short lived. Radiation pressure and Poynting-Robertson drag (P-R) induce rapid changes in the orbits of the dust particles ([Robertson, 1937](#); [Burns et al., 1979](#)). Radiation pressure blows out the smallest (usually sub-micron) grains on time scales of tens to hundreds of years, while P-R drag decreases the semi-major axes and eccentricities of larger grains on time scales of hundreds of thousands of years. As all of the known debris disks are older, with ages of at least a few million years (e.g. [Zuckerman & Song, 2004](#)), this confirms that the observed dust grains are being replenished, through the collisional destruction of larger

¹McCabe, C., Jansen, I., Stapelfeldt, K. (n.d.) Catalog of Circumstellar Disks, retrieved on July 06, 2018 from <https://www.circumstellardisks.org/>

planetesimals (Backman & Paresce, 1993).

The rest of this Introduction is organized as follows. Section 1.2 offers a fundamental perspective on the thermal emission from debris disks without considering resolved imaging. Measuring the unresolved excess thermal emission in the spectral energy distributions (SEDs) of debris-disk harboring stars remains the main approach to detecting and studying the broader population of debris disks with telescopes such as Spitzer and WISE (e.g. Chen et al., 2006; Hillenbrand et al., 2008; Patel et al., 2014). In Section 1.3 basic concepts of protoplanetary disk formation and evolution are introduced as a preamble to understand the dynamics of debris disks. We present the overall morphology of debris disks and introduce the fundamentals of scattering-induced polarization in Section 1.4. A brief description of modern high-resolution AO systems is covered in Section 1.5 with an emphasis in polarimetry observations with GPI in Section 1.6.

1.2 Unresolved Observations of Debris Disks

Fundamental Parameters

For many years, the study of the SEDs was the main tool available to detect the presence of debris disk. The SEDs of debris disks can be well approximated as single-temperature black bodies, thus providing the opportunity to test simple models depending on few parameters. We adopt a simplified model for debris disks with two parameters, temperature T and fractional luminosity f , where the latter is defined as $f = \frac{L_d}{L_\star}$ with L_d and L_\star the dust and star luminosity respectively. Both parameters can be obtained in a simple way following Equations 1.1 and 1.2

$$T = \frac{2898}{\lambda_{d,\max}} \text{ K} \quad (1.1)$$

$$f = \frac{F_{\nu,d,\max} \lambda_{\star,\max}}{F_{\nu,\star,\max} \lambda_{d,\max}} \quad (1.2)$$

where $\lambda_{d,\max}$, $\lambda_{\star,\max}$, $F_{\nu,d,\max}$ and $F_{\nu,\star,\max}$ are the wavelength in microns and flux at the maxima in the emission spectra of the disk and star respectively. Debris disks have low fractional luminosities, much lower than protoplanetary disks, meaning that they must be optically thin to stellar radiation. Debris disks are defined as having fractional luminosities of $f < 10^{-2}$, [Lagrange et al. \(2000\)](#) or disk:star $24\mu\text{m}$ flux ratios of less than 100 ([Sicilia-Aguilar et al., 2006](#); [Hernández et al., 2007](#)).

The assumption of single temperature dust grains sometimes is not adequate to describe the SED of some disks and in those cases, the presence of dust at multiple temperatures seems the best way to describe observations (e.g. [Chen et al., 2006](#); [Hillenbrand et al., 2008](#)). High-resolution imaging shows that in some systems, like η Corvi, dust is mainly located at two or more radii with separations of an order of magnitude ([Wyatt et al., 2005](#); [Duchêne et al., 2014](#)). Observations suggest that many debris disks are ring like, supporting this view of a simplified model to describe dust with a single temperature. Even though the number of observed debris disks spanning several orders of magnitude in radius is growing, the SED still resembles a single-temperature black body because there is a reduced contribution to the total infrared luminosity from dust that is close-in and distant to the star.

To derive the disk radius and mass, let's assume that this optically thin dust is uniformly distributed in a torus of radius r and width dr , and a vertical opening angle $2I$. Assuming that dust behaves as a black body, the radius of the disk can be estimated with

$$r_{bb} = (278.3/T)^2 L_{\odot}^{0.5}, \quad (1.3)$$

where L_{\odot} is Sun's luminosity, T the temperature in Kelvins and r_{bb} in astronomical units. With this, we can find the cross-sectional area σ in AU^2 of dust in the disk

$$\sigma = 4\pi r_{bb}^2 f. \quad (1.4)$$

Following [Beckwith et al. \(2000\)](#), the flux density F_{ν} from a disk viewed face-on, at a distance

d is given by

$$F_\nu = \frac{1}{d^2} \int_{r_0}^R B(T(r)) (1 - e^{-\tau_\nu(r)}) 2\pi r dr \quad (1.5)$$

with r_0 and R the disk inner and outer radius, $B_\nu(T(r))$ is Planck's function at temperature $T(r)$ and $\tau_\nu(r)$ is the opacity of dust at distance r . We express the optical depth $\tau_\nu(r)$ in terms of opacity κ_ν and surface density $\Sigma(r)$ as $\tau_\nu(r) = \kappa_\nu \Sigma(r)$. Now, for an optically thin disk, $\tau_\nu < 1$ with dust at a single temperature T we can approximate Equation 1.5 as

$$F_\nu \approx \frac{\kappa_\nu B_\nu(T)}{d^2} \int_{r_0}^R \Sigma(r) 2\pi r dr = \frac{\kappa_\nu B_\nu(T)}{d^2} M_{\text{disk}}, \quad (1.6)$$

thus Equation 1.6 gives an estimate of the mass of the dusty disk M_{disk} provided we know the flux density of the disk F_ν and opacity κ_ν in advance.

Unless the disk is resolved, we have no information regarding the size of the disk other than the approximate radius r_{bb} from Equation 1.3. In that case, we can still predict the flux density F_ν of the dusty disk using the cross-sectional area in Equation 1.4,

$$F_\nu \propto B_\nu(T) f r_{bb}^2 d^{-2}. \quad (1.7)$$

[Williams & Andrews \(2006\)](#) introduce a factor X_λ^{-1} in Equation 1.7 to account for the fall-off in the emission spectrum of debris disks. The fall-off factor X_λ is proportional to λ^{-1} for $\lambda \gtrsim 200\mu\text{m}$ while $X_\lambda = 1$ otherwise. From these considerations, we can estimate the mass of disk,

$$M_{\text{disk}} = 12.6 f r_{bb}^2 k_\nu^{-1} X_\lambda^{-1}, \quad (1.8)$$

in units of Earth's mass and the assumed opacity $k_\nu = 45 \text{ AU}^2 \text{ kg}^{-1}$ (e.g. $0.17 \text{ m}^2 \text{ kg}^{-1}$) corresponds to millimeter- to centimeter-sized dust. See [Semenov et al. \(2003\)](#) for a detailed study of modeled dust opacities of debris disks.

Estimates versus Observations

It is worth checking the radii returned using Equation 1.1 and Equation 1.3 for single-temperature debris disk. Table A.2 shows that the calculated disk sizes are lower estimates by a factor $\sim 2-3$ of the observed sizes. The problem with the estimated disks sizes is that we did not incorpo-

Star	Spectral Type	$L(L_{\odot})$	T (K)	r_{bb} AU	Obs. r (AU)
Fomalhaut	A3	16.6	65	75	~ 140
HR 4796	A0	21	110	30	~ 70
HD 181327	F6	3.3	75	25	~ 90
q1 Eri	F8	1.6	60	27	~ 75
HD 15115	F2	3.1	65	32	~ 90
HD 207129	G2	1.3	50	35	~ 160

Table 1.1: Estimated blackbody disk radius r_{bb} versus observed radius r for a list of debris disks.

rate information about the physical properties of the grains. Grains are poor emitters at the wavelengths where we observe the peak of the SED of the disk. The estimated temperatures are also lower estimates of the temperature of the disk. A detailed treatment incorporating the scattering and absorption efficiency and albedo as a function of wavelength is needed. Models incorporating Mie theory deal with this problem and as we will see, polarimetry of debris disk will be useful in modeling the scattering properties of dust grains in this regime of sizes.

1.3 Evolution of Debris Disks

1.3.1 From Protoplanetary Disks to Debris Disks

Gas-rich protoplanetary disks are observed surrounding the youngest stars and it is a common byproduct of stellar formation. Protoplanetary disks are a mixture of surviving interstellar grains and nebula condensates with high angular momentum matter collapsing to form a disk. Measurements of interplanetary dust and primitive meteorites suggest grain sizes of 0.05 - 100

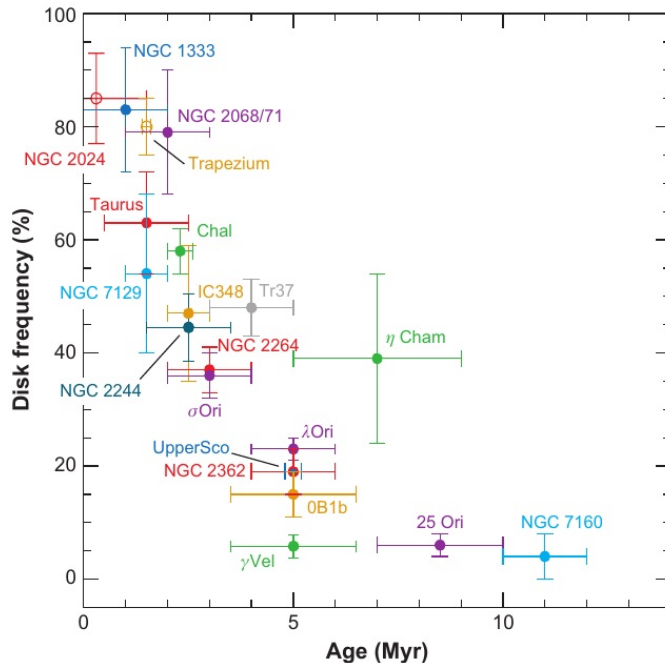


Figure 1.1 Fraction of sun-like stars with near-IR excess as a function of time, (Hernández et al., 2007). Adapted from Wyatt (2008).

μm with an approximate dust:gas mass ratio of the disk of 0.01 (Lissauer, 1993). Submillimeter observations and CO linewidths, suggest a wide range in dust masses and disk sizes.

Grain sizes in the optically thin disk can be estimated from observations in the millimeter regime. At long wavelengths, $h\nu \ll k_B T$, and thus the Rayleigh-Jeans approximation $B_\nu(T) \sim 2k_B T \frac{\nu^2}{c^2}$ can be used to transform Equation 1.7 into:

$$F_\nu \sim 2k_B T M_{\text{disk}} \kappa_\nu \frac{\nu^2}{d^2 c^2}. \quad (1.9)$$

Assuming that opacity follows $\kappa_\nu \propto \nu^\beta$, we have $F_\nu \propto \nu^{2+\beta}$. This implies that observations can be used to constrain the dependence of dust opacity with wavelength. Observations of interstellar dust suggest $\beta \sim 2$, whereas that $\beta \sim 1$ for protoplanetary dust, (Draine, 2006). The authors show that for solid dust particles following a power-law size distribution $dn/ds \propto s^{-p}$, $\beta \sim 1$ would indicate grain growth by agglomeration.

One way of studying the evolution of these protoplanetary disks is to look for the near-IR

and mid-IR emission of the disk. Observations in the near-IR are indicative of dust very close to the star, at distances much smaller than 1 AU. Most sun-like stars older than 6 Myr show no near-IR disk emission while for early type stars, few have protoplanetary disks by 5 Myr, see Figure 1.1.

The near-IR excess ratio, which indicates the presence of dust very close to the star, is observed to decrease with age. There is no clear mechanism driving the depletion of dust at distances much smaller than 1 AU, however observations suggest grain growth and settling to the midplane and viscous accretion onto the star as possible mechanisms (Calvet et al., 2005; Sicilia-Aguilar et al., 2006; Hernández et al., 2007).

In absence of turbulence, dust settling onto the midplane of protoplanetary disks is believed to occur in about 10^5 yr at 1 AU from a sun-like star. A more rigorous treatment shows that in the presence of turbulence, dust settling will only occur after substantial dust growth. (Armitage & Valencia, 2010).

The disappearance of the inner dust is often considered synonymous with the disappearance of the gas of the disk, which is a rapid process compared to stellar lifetime as suggested by the reduced number of stars with intermediate levels of near-IR excesses. However it is interesting to note that few stars bearing disks without near-IR excesses, do show mid-IR emission from dust at a few astronomical units. These systems are described as transitional disks, where dust is being clear from the inside-out while substantial dust is found at a few AU. Hernández et al. (2007) finds transitional disks in 10% of stars in the Herbig Ae/Be mass range ($> 2M_{\odot}$) and in $\sim 35\%$ T Tauri mass range ($1-0.1 M_{\odot}$).

The origin of the dust that populates debris disks is crucial to better understand planetary formation processes. Whether the observed dust is primordial as remnant of the protoplanetary dust, originated as a second generation population from planetesimal interactions or a mixture of both, it is certainly important to constrain these hypothesis with models and observations.

Submillimeter observations of protoplanetary disks and debris disks up to ages of 1Gyr indicate a clear contrast in disk masses. Figure 1.2 shows that protoplanetary disks have between

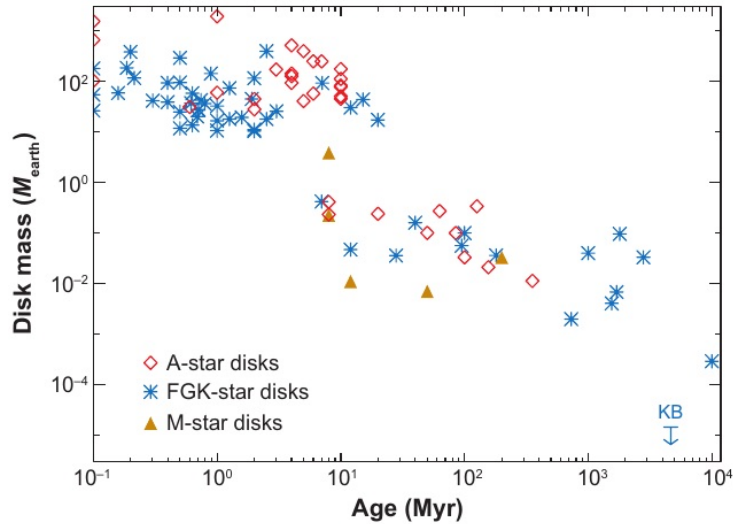


Figure 1.2 The evolution of disk mass from submillimeter observations, adapted from Wyatt (2008).

two and four orders of magnitude more mass in dust than debris disk in a rapid transition < 10 Myr, (Wyatt, 2008). Old debris disks suggest that dust should be replenished over timescales larger than 100 Myr possibly as the consequence of a population of planetesimals larger than 1 km that produces dust through disruptive collisions. However, young disks do not fit such requirements therefore the youngest debris disk may be comprised of remnant protoplanetary dust. Nevertheless, constant dust levels in protoplanetary disks imply the existence of a mechanism to replenish the dust, as it is expected that the growth of dust in protoplanetary disks to occur rapidly.

1.3.2 Dust from Planet Formation Processes

The mechanisms driving the formation of planetesimals from objects of near a kilometer in size is fairly well understood. Once objects grow through sticky collisions up to a size of a few kilometers, they enter into a stage of fast growth known as runaway growth. Gravitational attraction enables young planetesimals to accrete mass faster with a cross-sectional area $\sigma_g \propto R^4$ for objects larger than a few kilometers. This period of frenzy accretion is then followed by

a slower growth. This new period known as oligarchic growth, is a consequence of the change in the dispersion velocity of the planetesimals induced by the largest object. When objects reach dwarf-planet sizes, the interaction between the largest objects becomes chaotic, where close encounters and diffusion in semimajor axis kicks in (Lissauer, 1993).

Models suggest that Mars-sized planetary embryos have enough mass to disrupt the population of small planetesimals (< 100 km) increasing their dispersion in velocities, Kenyon & Bromley (2002). Authors show that the stirring induced by the large objects starts a collisional cascade, $\beta = 1$, of the small planetesimals creating dust, and this production of dust peaks within a few Myr when the large objects reach ~ 2000 km in size. This in principle could be observed as a $24\mu\text{m}$ excess with current instruments, however it depends on the parameters of the model. For example, having a good handle on some of the input parameters, such as the initial gas content and amount of primordial dust in the system, is often difficult and it is part of the inherited complexity in model validation.

1.4 Disk Morphologies and the Use of Spatially Resolved Polarimetry

1.4.1 Disk Morphology

Resolved debris disks suggest a rich variety of complex morphologies such as warps, spirals, gaps, offsets, and asymmetries. Some disks seen edge-on resemble a needle-like shape, as in a razor-thin edge. The observed morphology can be the result of hidden planets interacting with the disk. For instance, a rough estimate of the size r of the gap opened by a Jupiter-mass planet with semimajor axis a , and mass $10^{-3}M_{\odot}$ can be approximated as $r = a \pm 3r_R$ where $r_R = a\left(\frac{\mu}{3}\right)^{1/3}$ is the Roche radius.

Figures 1.3, 1.4, 1.5 and 1.6 show some of the typical features of debris disks in scattered light and polarimetry. Figure 1.3 provides a clear example of the image quality of SPHERE

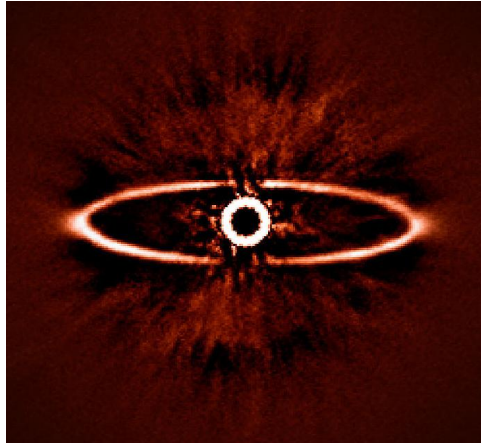


Figure 1.3 HR 4796A in H-band, first light of SPHERE, ESO/J.-L. Beuzit et al. /SPHERE Consortium.

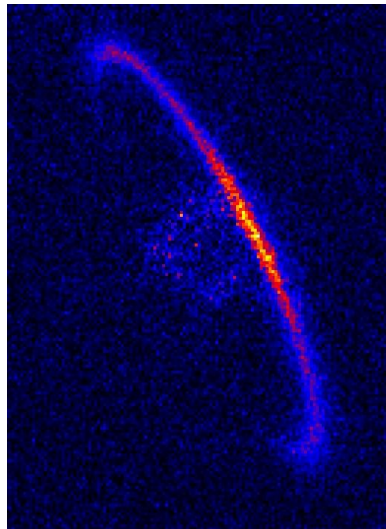


Figure 1.4 HR 4796A in H-band, first light of GPI in linearly polarized intensity, (Perrin et al., 2015).

in remarkable detail revealing the HR 4796A disk ($i = 76^\circ$). Figure 1.4 also shows the superb performance of GPI in polarimetry mode detecting the HR 4796A disk, with an exquisite subtraction of the residual halo of the coronagraph. Figure 1.5 shows detections with GPI polarimetry of two debris disks, the HD 131835 (Hung et al., 2015) and HD 35841 (Esposito et al., 2018) disks. Like the HR 4796A disk, the HD 131835 and HD 35841 debris disks are observed at high inclinations, 75° and $i \sim 85^\circ$ respectively, and may thus indicate a bias

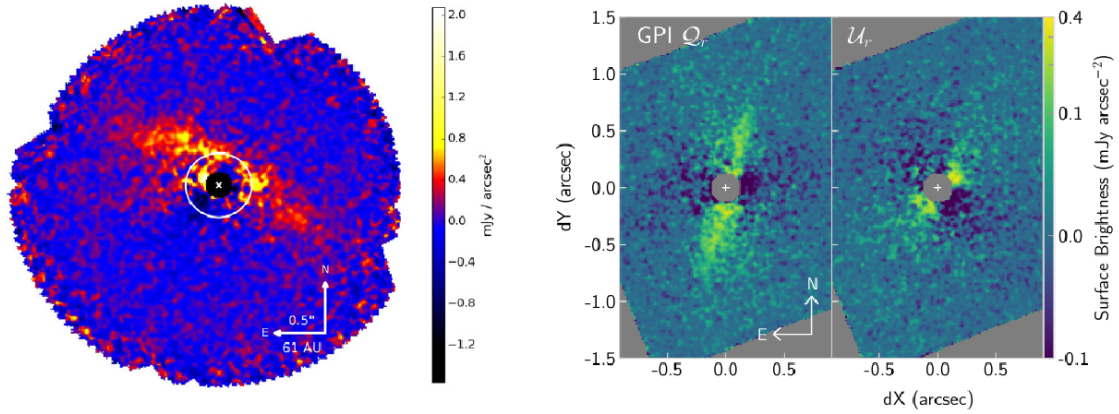


Figure 1.5 GPI polarimetry observations of highly inclined debris disks. Right: the HD 131835 disk ($i = 75^\circ$)(Hung et al., 2015). Left: HD 35841($i \sim 85^\circ$) (Esposito et al., 2018).

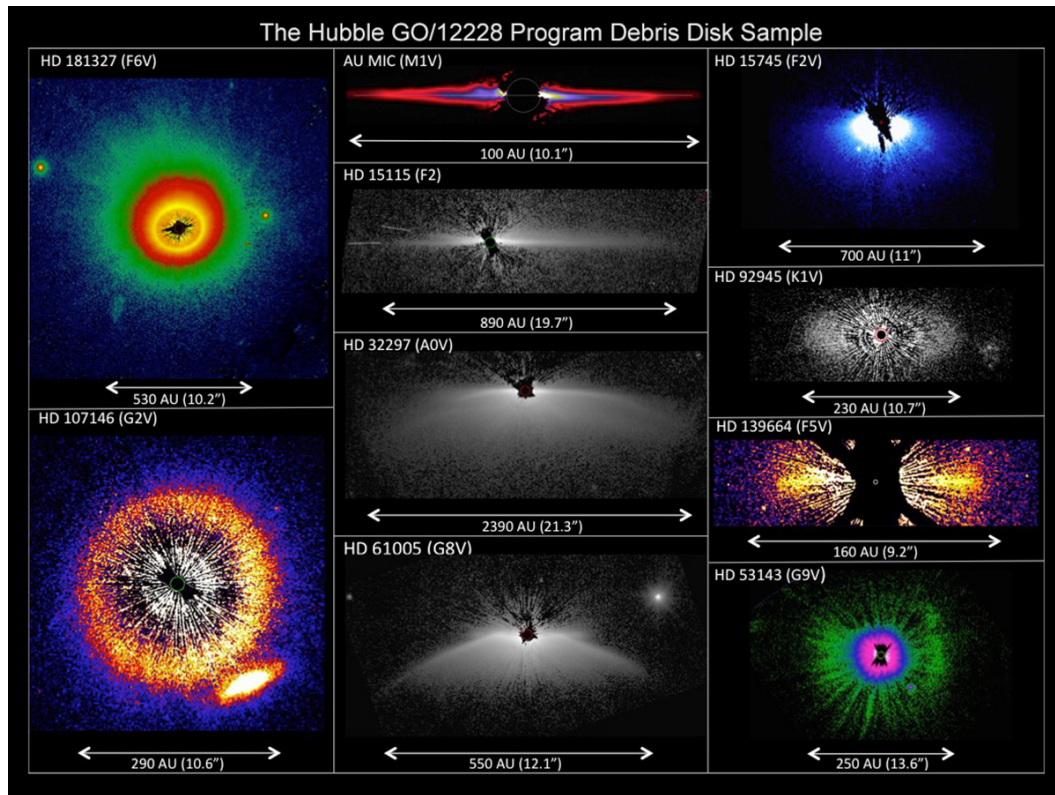


Figure 1.6 Hubble views of debris disks in scattered light, Image Credit: NASA/ESA, G. Schneider (University of Arizona), and the HST/GO 12228 Team.

favouring the detection of highly inclined disks. Furthermore, 23 of the 25 disks detected with GPI polarimetry, including the ones presented in this thesis: HD 141569A ($i \sim 60^\circ$), and HD

157587, ($i = 72^\circ$), have inclinations above 60° with just two disk detections with inclinations between 30° and 50° (Figure 1.7, Thomas Esposito, private communication). The detection of disks with moderate to high inclinations suggest that strong macroscopic polarization from optically-thin debris disks is favoured for this range of viewing geometries. Such trend in polarization emission with viewing geometry is related to the polarization dependence with scattering angle and thus, related to physical properties of the constituent scattering particles populating these disks. This is an ongoing investigation and the results will be published in an upcoming GPI debris disk survey paper led by Thomas Esposito.

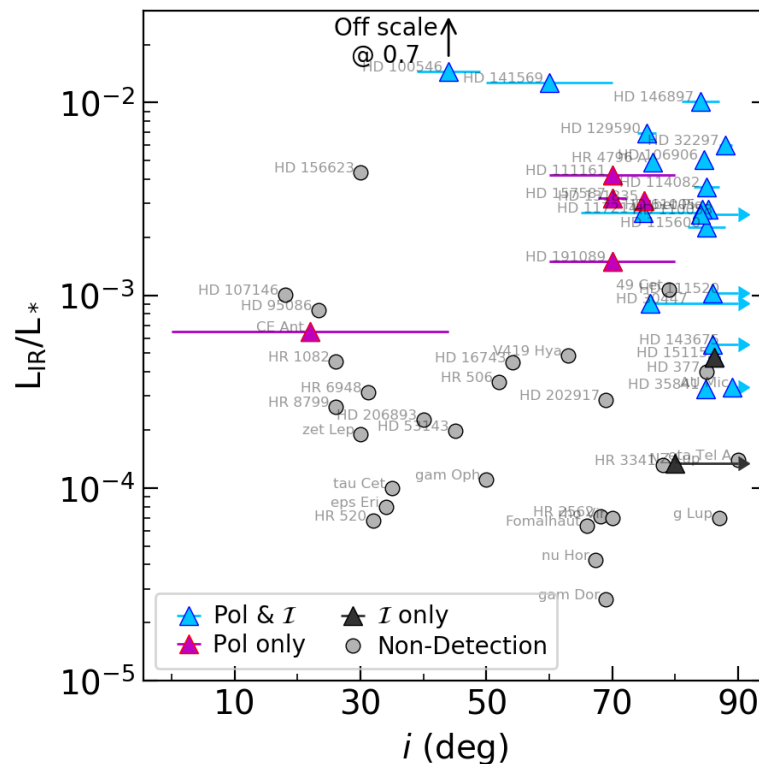


Figure 1.7 Fractional luminosity vs disk inclination of disk observations with GPI. (Thomas Esposito, private communication). This will be included in an upcoming GPI debris disk survey publication.

1.4.2 Polarimetry

The use of polarimetry to study debris disk has taken off recently in light of the advances in high-resolution imaging with AO instruments. Polarimetry allows us to suppress the residual starlight that plagues most advanced AO systems reducing their performance in contrast. The undesired residual light surrounding the central star in AO systems, often referred as speckles, creates a bright halo that buries any faint contribution from circumstellar material. Polarization excels in this regard offering a simple procedure to reduce the glare having dramatic improvements in contrast and sensitivity, helping to identify faint astrophysical sources. Resolving faint disks brings the possibility to set limits on disk size, and infer the presence of planets as evidenced by gaps and warps.

Polarization is also a rich source of information of astrophysical properties and complements photometric and spectroscopic studies of debris disks. Astrophysical observations deal with superposition of a very large number of elementary electromagnetic waves and are sensitive to macroscopic polarization. Light from a star is not polarized as photons are randomly scattered in the photosphere. However, the incident light² scattered by dust grains is linearly polarized and this comprises the astrophysical source of polarization. Polarimetry allows to determine physical properties of the scatterers, such as size and structure from this linearly polarized light. This is a very valuable capability to gain insight into physical processes through which dust and planetesimals assemble to form planets.

1.4.3 Stokes Parameters, Stokes Vector and Mueller Formalism

The polarization state of electromagnetic radiation can be characterized in terms of the orientation and norm of the electric field vector $\mathbf{E}(t, z)$. Astronomical observations deal with light intensities, thus it is useful to express the polarization states in terms of characteristic intensities

²It is assumed for the sake of simplicity that the incident light propagates along a well-defined direction, ignoring thus multiple scattering and absorption events.

known as the Stokes parameters

$$\begin{aligned}
 I &= \langle E_x^2 \rangle + \langle E_y^2 \rangle \\
 Q &= \langle E_x^2 \rangle - \langle E_y^2 \rangle \\
 U &= 2\langle E_x E_y \cos \delta \rangle \\
 V &= 2\langle E_x E_y \sin \delta \rangle
 \end{aligned}
 \tag{1.10}$$

where $E_{x,y} = E_{x,y}(t)$, $\delta = \phi_2 - \phi_1$ is the difference of arbitrary phases ϕ_1 and ϕ_2 and $\langle \rangle$ denotes the time average³. By definition, I is the intensity of the wave, Q quantifies the difference in intensities in x and y direction probing thus the linear polarization. Similarly, U also probes the linear polarization, quantifying two field components diagonal at angles of 45° and 135° . Lastly, V corresponds to the circular polarization.

The Stokes parameters can be used to find the degree of linear polarization m_L and angle χ ,

$$\begin{aligned}
 m_L &= \frac{\sqrt{Q^2 + U^2}}{I} \quad m_L \in [0, 1] \\
 \chi &= \frac{1}{2} \arctan_2\left(\frac{U}{Q}\right) \quad \chi \in [0, \pi]
 \end{aligned}$$

with χ measured in the QU plane.

By construction, the Stokes parameters assume that the source of radiation and the observer share a common non-rotating frame of reference. This is not often the case in astronomical observations, were the telescope field of view constantly rotates due to Earth's rotation. Using complex exponential notation we can arrive to an equivalent representation of the Stokes parameters in the frame of reference of the source in the sky. Considering E_H and E_V as the horizontal and vertical components of the electric field respectively in the plane of reference of

³Time averages are calculated over times much larger than $2\pi/\omega$ where ω is the angular frequency.

the telescope and ψ the parallactic angle counted from north to east, we then have

$$\begin{aligned}
 2\langle E_V E_V^* \rangle &= I + Q \cos 2\psi + U \sin 2\psi \\
 2\langle E_H E_H^* \rangle &= I - Q \cos 2\psi - U \sin 2\psi \\
 2\langle E_V E_H^* \rangle &= -Q \sin 2\psi + U \cos 2\psi - iV \\
 2\langle E_H E_V^* \rangle &= -Q \sin 2\psi + U \cos 2\psi + iV
 \end{aligned} \tag{1.11}$$

where i is the imaginary number and the operator $*$ denotes complex conjugation.

The Stokes parameters can be expressed in terms of a four dimensional vector, the Stokes vector \mathbf{S}

$$\mathbf{S} = \begin{bmatrix} I \\ Q \\ U \\ V \end{bmatrix} \equiv \mathbf{TC} \tag{1.12}$$

with the coherency vector \mathbf{C} as

$$\mathbf{C} = \begin{bmatrix} \langle E_x E_x^* \rangle \\ \langle E_x E_y^* \rangle \\ \langle E_y E_x^* \rangle \\ \langle E_y E_y^* \rangle \end{bmatrix} \tag{1.13}$$

and the matrix

$$\mathbf{T} = \begin{bmatrix} 1 & 0 & 0 & 1 \\ 1 & 0 & 0 & -1 \\ 0 & 1 & 1 & 0 \\ 0 & -i & i & 0 \end{bmatrix} \tag{1.14}$$

For light propagating through an instrument, the polarization states will be modified as light meets the different components of the optical system, thus changing the Stokes parameters.

Modifications of the polarized state can be expressed as modifications of the Stokes vectors as

$$\mathbf{S}' = \mathbf{M}\mathbf{S} \quad (1.15)$$

where \mathbf{M} is the 4×4 Mueller matrix. Modifications of the Stokes vector within any particular instrument can be expressed as the consecutive multiplication of several Mueller matrices, one for each component along the optical path. The following examples

$$\begin{bmatrix} 1 & 0 & 0 & 0 \\ 0 & 1 & 0 & 0 \\ 0 & 0 & -1 & 0 \\ 0 & 0 & 0 & -1 \end{bmatrix} \quad (1.16)$$

and

$$\begin{bmatrix} 1 & 0 & 0 & 0 \\ 0 & \cos 2\beta & \sin 2\beta & 0 \\ 0 & -\sin 2\beta & \cos 2\beta & 0 \\ 0 & 0 & 0 & -1 \end{bmatrix} \quad (1.17)$$

describe reflection and rotation by an angle β respectively, with several matrices often used to account for all reflections and rotations for each instrument.

1.4.4 Differential Polarimetry

One crucial advantage of the use of polarimetry in high-resolution instruments is the ability to significantly reduce the amount of speckle contamination. Even in the most advanced AO systems, there is a residual halo of uncorrected diffracted starlight surrounding the central star. Unlike HST, with its exquisite PSF stability, most instruments have a large collection of speckles, time-varying realizations of the star's PSF. Although a collection of methods exists to mitigate its effects (ADI, LOCI, KLIP), they are designed to improve the sensitivity of point-

like sources and could lead to unpleasant results when applied to extended sources like disks.

However, dealing with a polarized signal means that we can exploit a positive aspect of the atmospheric turbulence. Atmospheric turbulence is not dependent on polarization, thus the speckles for the orthogonal components of the electric field are identical. Therefore, by imaging both orthogonal components of polarization simultaneously, the speckle halo can be effectively suppressed in difference images, leaving just the polarized signal.

Differential polarimetry allows to suppress the speckle halo in difference images taken simultaneously attaining improvements up to $200\times$ in linearly polarized intensity (Perrin et al., 2015). To achieve simultaneous observations a polarizer prism is used (often a Wollaston prism) that splits the incoming light into two polarized beams. There are several other options to choose from, and is a matter of engineering needs. With information about the relative orientation of the frame of reference on the sky and telescope, along with optical configuration of the instrument, the astrophysical polarization can be measured.

1.4.5 Insight into Physical Properties from Polarimetry

Radiation scattered by circumstellar particles with sizes comparable to the wavelength of incident radiation becomes linearly polarized. The direction of polarization of the electric vector of this scattered radiation is perpendicular to the scattering plane, a plane that contains the incident and scattered rays (Tinbergen, 1996; Hough, 2006). Information about the size and index of refraction of material scattering the radiation can be found from the wavelength dependence of the linear polarization, whereas the degree of linear polarization will depend on the inclination of the disk (Tinbergen, 1996; Hough, 2006; Perrin et al., 2009a).

Observations in scattered light are sensitive to scatterers with size parameter $x = \frac{2\pi r}{\lambda} \sim 1$, thus primarily at $r \leq 1\mu\text{m}$ for optical and near-IR. Scattering of radiation by spherical particles with sizes comparable to the wavelength of incident light is described by Mie theory. In this approximation, calculations and laboratory experiments can be used to infer the polarization dependence with scattering angle and properties of the grains. Figure 1.8 indicates that in

general, polarization is highest close to 90° where compact grains with sizes smaller relative to the wavelength polarize light greatly. In contrast, for larger compact grains the polarization is less strong (Perrin et al., 2009a). Porous grains however show large degrees of polarization across all sizes.

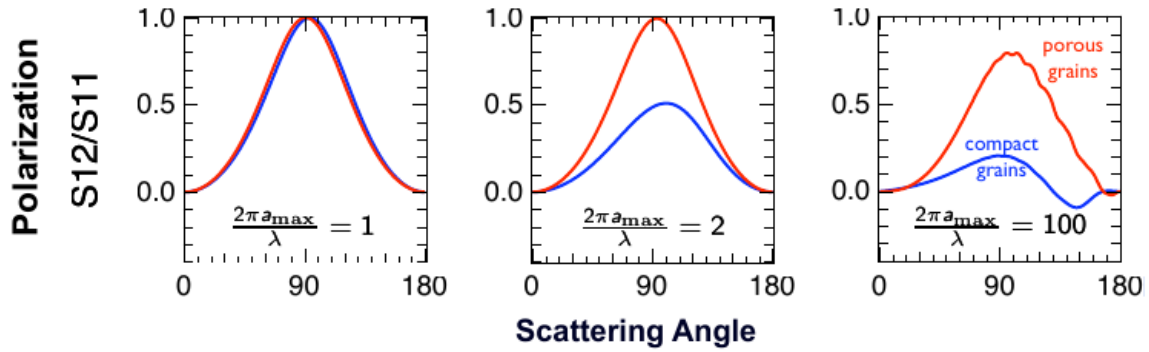


Figure 1.8 Model of scattered-induced polarization as a function of scattering angle and particle properties (Perrin et al., 2009a).

An empirical model given by the Henyey-Greenstein function (Henyey & Greenstein, 1941) is often used to mimic the angular dependence of light scattering by small particles. The Henyey-Greenstein function $p(\theta)$ is

$$p(\theta) = \frac{1}{4\pi} \frac{1 - g^2}{(1 + g^2 - 2g \cos \theta)^{3/2}} \quad (1.18)$$

where θ is the deviation from the forward direction and the anisotropic factor $g \in [-1, 1]$. This function can be viewed as the probability to get a scattering event in a particular direction,

$$\int \int_{4\pi} p(\theta) d\Omega = 1. \quad (1.19)$$

In this view, $g = \langle \cos \theta \rangle$ is the expectation value of the cosine of the scattering angle, $\cos \theta$, with $g = 0$ resulting in isotropic scattering. Considering the case of forward scattering, $\theta = 0$

and backward scattering, $\theta = \pi$, the forward:backward scattering ratio is

$$\frac{p(0)}{p(\theta)} = \left(\frac{1+g}{1-g} \right)^3. \quad (1.20)$$

Therefore $g > 0$ forward scattering is dominant, while for $g < 0$, backscattering predominates.

In the presence of non-spherical, porous grains, we need information about both degree of forward scattering and maximum polarization to disentangle the physical properties of the particles. Such grains, expected to form after collision aggregation, display the ability to polarize light greatly, even for grains much larger than the wavelength of light, thus mimicking the behavior of small compact grains. However, large porous grains are in most cases strong forward-scatterers, hence having larger values of the anisotropic factor g . Figure 1.9 provides an example of induced polarization for typical dust grains of different composition and porosities.

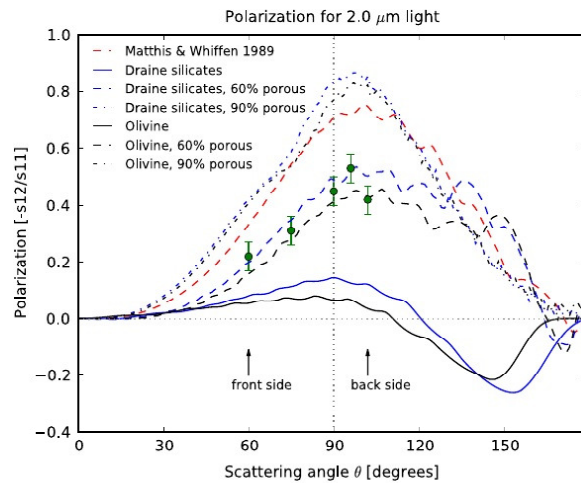


Figure 1.9 Example of how polarization depends on grain properties and scattering angle. (Perin et al., 2009b). The ratio S_{11}/S_{12} indicates the amount of linear polarization is plotted as a function of scattering angle based on Mie theory.

1.5 Observational Methods I

1.5.1 Coronagraphic Observations

Direct imaging of exoplanets and debris disks is a fast developing subject in current astronomical research and relies on achieving the following goals ([Macintosh et al., 2008](#)):

- Suppress starlight to attain contrast levels of 10^{-7}
- Offer reliable sensitivity at very small inner working angles. For instance, 0.13 arcsec for regions up to 5 AU for 40 pc star
- Achieve diffracted-limited resolution in the mid-IR in world-class ground observatories
- Gather spectra of young warm exoplanets with moderate resolution.
- A working platform to perform polarimetry to probe the polarization signatures of young planetary systems.

High-contrast sensitivity depends on controlling the residual starlight rather than achieving larger apertures whereby the primary issue is the residual starlight contaminating the regions close to the star. Such contamination comes as light due to optical diffraction, light due to imperfect optics and a contribution from the propagation of the light through the turbulent atmosphere. Even in an ideal case of a perfect, diffraction-limited instrument, the Point Spread Function (PSF) of a star is an Airy function that spreads a significant amount of power to its vicinity, making it difficult to subtract the light of the star and enhance the presence of a dim companion. A factor of 10^{-4} of the peak brightness at a few angular resolution elements will be sufficient to drop a faint object below background levels.

Coronagraphy is one of the current techniques adopted in several surveys to remove diffracted light with proven results ([Oppenheimer et al., 2001](#); [Macintosh et al., 2008](#)), [Beuzit et al. \(2008\)](#), [Perrin et al. \(2015\)](#)) just to name a few. Figure 1.10 shows a schematic and simplified view of a coronagraph. In this design, two masks are used to suppress starlight. The first mask

is placed in the focal plane with an obstruction of 1.5 to $3 \lambda/D$ in radius. This blocks most of the light from the star, but still some of the light is diffracted around it. After forming an image of the telescope pupil, a second mask is placed in the beam to suppress the light that concentrates in the outer and inner rings. The Lyot stop further increases the occulting spot and reduces the telescope aperture simply to block the enhanced rings that arise from the diffraction after the first occulter.

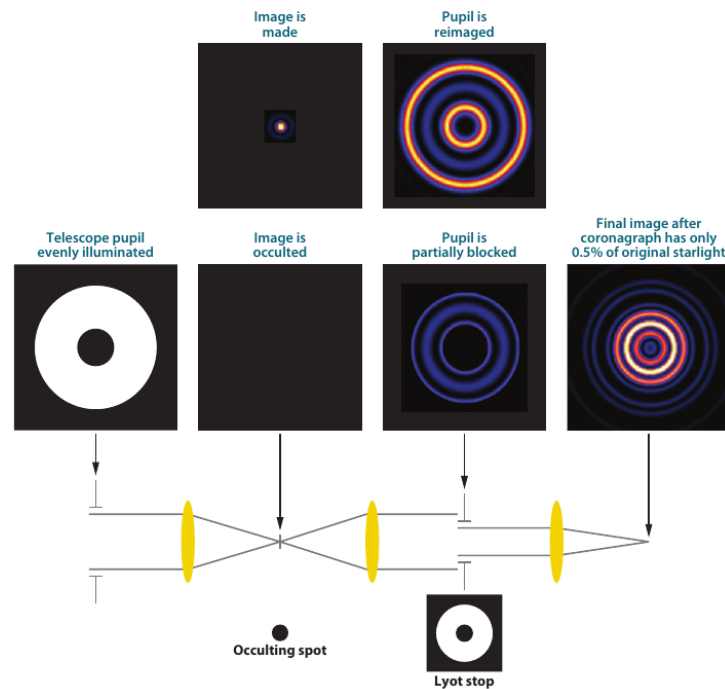


Figure 1.10 Schematic view of the Lyot coronagraph. Adapted from (Sivaramakrishnan et al., 2001).

1.5.2 Speckle noise

Turbulence in the Earth's atmosphere limits the performance of astronomical telescopes. This significantly deteriorates the resolution power of ground-based telescopes reducing their performance to no better than an 8 inch backyard telescope. Plane waves arriving from astronomical sources propagate through the turbulent atmosphere where variations in the index of refraction distort the wavefront, spreading out the light of the source in a fuzzy blob when im-

aged in the focal plane of the instrument. The strength of turbulence is often described by the Fried Parameter r_0 (Fried, 1966), where r_0 is often defined as the largest distance, as measured on the telescope mirror, over which the phase of the incoming wavefront is well-correlated. Typical values of $r_0 \sim 10$ and 15 cm at $0.5\mu\text{m}$.

Speckles are the biggest challenge for any high-contrast observer and arise when a point-like source of radiation is observed in any optical system. Consider a wavefront of light from an unresolved star. This wavefront in a perfect situation would be the mathematical approximation a portion of the incoming spherical wave. Once detected at the telescope, any minuscule deviation (RMS $\sim \lambda/10$) in the wavefront away from the ideal plane wave representation, will perturb the PSF of the star in the image plane. Such perturbations manifest themselves as an unpredictable, time-varying collection of faint spots ($\sim 3 \times 10^{-2}$ of the central star) at arbitrary locations throughout the image, each with different intensity. This *speckle noise* is thus a realization of tiny phase differences in the incoming radiation field and is a major problem in high-contrast imaging. In general, speckle lifetimes are of the order of few milliseconds setting thus the pace at which AO systems should compensate to successfully reconstruct the corrupted wavefront.

1.5.3 Adaptive Optics (AO) Design

We present a much simplified description with the fundamentals of AO design pertinent to some of the current platforms designed to image exoplanets and debris disk.

Wavefront Sensing

AO is a technique for correcting optical distortions to dramatically improve image quality and enables astronomical telescopes to attain their theoretical performance of $\sim 1.22\frac{\lambda}{D}$. The power of any AO system is characterized by the Strehl ratio it produces and is defined as the ratio of the peak intensity of the PSF to that of a perfect optical system. Diffraction-limited images are achieved with $\text{Strehl} > 0.8$ and so-called XAO systems often achieve Strehl ratios ~ 0.90

in the mid- and near-IR.

Before attempting to improve and restore the image quality of the system, a procedure must be devised to probe the aberrations in the wavefront that arrives to the telescope. One of such implementations is the Shack-Hartmann wavefront sensor (SHWFS [Hartmann, 1900](#); [Shack, 1971](#)). This sensor comprises a large collection of minuscule lenses in a grid conjugated with the pupil plane of the telescope. Each lens will probe a small region of the incoming wavefront and thus producing an image with a collection of PSFs that are recored in a fast detector. The aberrations in the wavefront would be recorded as a displacement in the PSF from the lenses. Figure 1.11 depicts a schematic cartoon of this device.

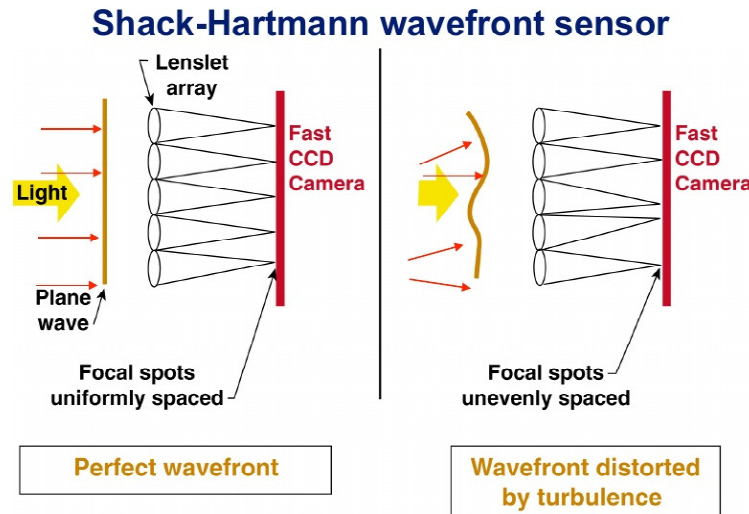


Figure 1.11 Simplified representation of a Shack-Hartmann wavefront sensor. The displaced PSFs track the aberrations in the wavefront in a fast CCD camera, Lawrence Livermore National Laboratory and NSF Center for Adaptive Optics.

The SHWFS is used as a proxy of the wavefront error in phase $\phi(x, y)$ of the incoming light.

$$\begin{aligned}\Delta y &= \frac{\partial \phi}{\partial y}(x, y) \frac{f}{p} \\ \Delta x &= \frac{\partial \phi}{\partial x}(x, y) \frac{f}{p}\end{aligned}$$

(1.21)

where the displacements Δx and Δy are a function of the derivatives of $\phi(x, y)$ for a lens of focal distance f and a detector of pixel size p . Thus the motion of the spots is proportional to the slope of the wavefront over the subaperture. SHWFS measures the average derivative of the wavefront and this is used as input to reconstruct the wavefront. The FWHM of a spot is $\sim \lambda/D$ and design considerations imply that $f < \frac{D^2}{2\lambda}$ for lenses of diameter D . Typically, $f = 2$ millimeters for a $200\mu\text{m}$ diameter lens at $\lambda = 0.5\mu\text{m}$.

Deformable Mirrors

With a wavefront sensing device in place, AO systems use one or more deformable mirrors (DMs) to physically correct the incoming wavefront. These mirrors are often comprised by a large collection of subapertures driven by actuators than can individually change their position very rapidly thus changing the overall shape of the mirror. There are different kind of DMs, each one with their own specifications to suit the observational requirements of a particular program. A commonly used design involves a collection of square elements with three degrees of freedom, piston, tip and tilt. Basic requirements for good DMs can be summarized as follows

- Hysteresis of actuators with displacements of several microns. Example: Boston Micro-machines Corp. deformable mirrors with strokes of $4\mu\text{m}$.
- Rapid response, in the order of 1000 cycles per second, a fraction of the coherence time
- Low power dissipation. Heat induces seeing effects. Low voltages preferred, $\sim 200\text{V}$.
- Relative small sizes are not a problem. Size is related with number of actuators and could be costly. However, the Lagrange invariant implies that for a 30 m telescope DM size of about 30 cm.

DMs are conjugated with the telescope pupil and are placed before the wavefront sensor therefore a system control can be used to correct the wavefront imperfections. The size of the actuators depend on the typical value of r_0 since subapertures of size $\sim r_0$ are desired.

Often thousands of actuators are packed into most DMs. For instance, GPI incorporates a DM with $64 \times 64 = 4096$ actuators in its High Order Wavefront Unit. These small units are rather expensive with current prices of $\sim \$1000$ per degree of freedom or $\$100,000$ per 1000 actuators.

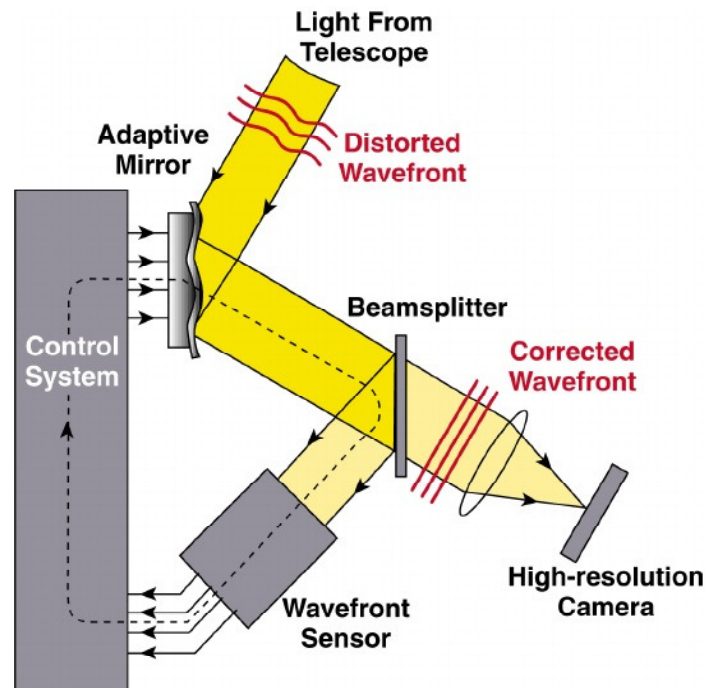


Figure 1.12 Cartoon with the fundamentals of AO system design, Lawrence Livermore National Laboratory and NSF Center for Adaptive Optics.

A schematic representation of the fundamentals of AO systems is presented in Figure 1.12. The system is operated within an open loop (feed forward) control, where phase errors are monitored. Once the system achieves nominal values, the loop is closed (feedback control). The system needs to operate at a rate of hundreds or thousand cycles per second. In each cycle, matrix reconstruction algorithms are employed to reconstruct the wavefront phase from the average derivatives measured in the fast detector. The number of calculations becomes prohibitive, often $\propto O(n^2)$ for large number n of actuators thus requiring high-end CPU computers.

1.5.4 ExAO implementations: GPI

GPI, (Macintosh et al., 2008), is one of the novel instruments recently commissioned at Gemini South and materializes the latest efforts to directly image exoplanets and debris disks. GPI is a high-resolution integral field spectro-polarimeter (IFS) that combines coronagraphic observations with an XAO system with five bandpass filters: Y, J, H, K1 and K2 covering the mid-IR range and its selection was motivated by the needs of exoplanet spectroscopy. Home of the Gemini Planet Imager Exoplanet Survey (GPIES), this instrument already returned its newly discovered exoplanet 51 Eri b (Macintosh et al., 2015) and a new debris disk imaged in HD106906 (Kalas et al., 2015).

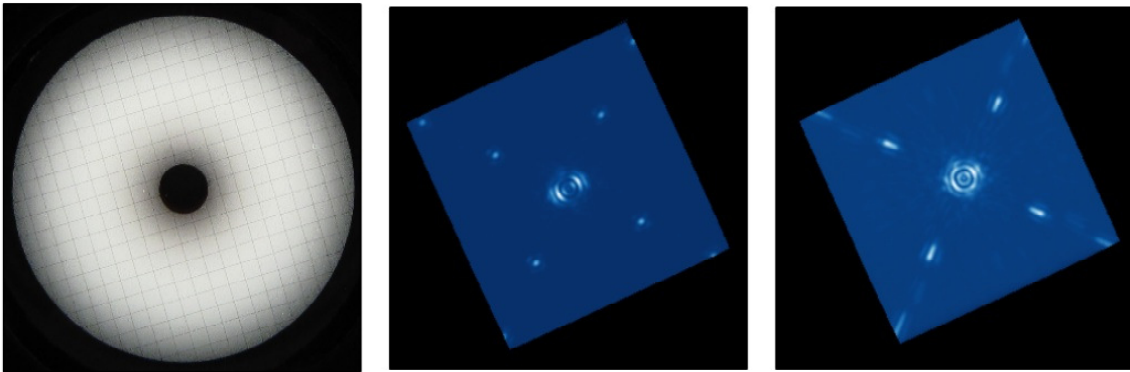


Figure 1.13 GPI Apodizer with imprinted grid patten in H-band(left). Image in spectroscopy mode with the four fiducial satellite spots visible (center). Polarimetry observation with fiducial satellite spots smeared-out in H-band (right) (Wang et al., 2014).

Controlling and reducing the amount of speckle noise is one of GPI main directives to achieve the goals set for high-contrast imaging of exoplanets. For this purpose, an apodized-pupil Lyot coronagraph (APLC) combines a classic Lyot coronagraph with a moderate apodization. The size of the hard-edged occulter in the Lyot mask is $5\lambda/D$. Another important feature in GPI's design, is grid pattern imprinted onto the apodizer. This allows to create four satellite spots as the first order diffraction points. This fiducial spots enable astrometric and photometric measurements that otherwise will not be possible due to the fact that the central star is behind the occulter. Figure 1.13 shows the apodizer with the grid pattern and images with the fiducial

satellite spots in spectroscopy and in polarimetry mode.

[Maire et al. \(2014\)](#) shows that ratio of the total flux of the occulted star and the satellite spots provide a difference in magnitude $\Delta m = 9.39 \pm 0.11$ in H-band. In consequence satellite spots fluxes are dimmer and correspond to 10^{-4} of the flux of the occulted star. This value defines the grid ratio in H-band allowing photometric measurements of exoplanets.

In order to achieve high Strehl ratios, GPI operates two Boston Micromachines Corp. DMs to control low and high order wavefront aberrations feeding two SHWFS in the near infrared. The Low Order Wavefront Sensor (LOWS) sports a 7×7 *woofer* DM with $4\mu\text{m}$ stroke with 1 millisecond updates in tip and tilt. The HOWFS includes a 64×64 DM with the same specifications in stroke.

GPI is a lenslet-based IFS where a grid of lenslets is used in the focal plane to dissect the image creating an array of spectra. Individual spectra are 16 pixels long and separated by 4.5 pixels. This enables an extraction method using a 3×1 box to retrieve the spectra. The Integral Field Spectrograph Dewar (IFSD) houses the science instrument with two prisms enabling the spectrometry and polarimetry modes. Spectral resolution with this instrument is $R = \Delta\lambda/\lambda = 45$ at H-band. The individual spectra are extracted and a spectroscopy cube (SPDC) is assembled with spatial and wavelength axes (x, y, λ) . Each SPDC image file has dimensions of $281 \times 281 \times 36$ with the dispersion axis at the end.

These considerations in instrument design, allow GPI to offer inner working angles of 0.2 arcsec with contrast of 11 magnitudes ($5\text{-}\sigma$ level) at 0.4 arcsecs within a 2.8×2.8 arcsec field of view at 14.166 milliarcsec resolution ([Macintosh et al., 2008](#); [Perrin et al., 2015](#); [De Rosa et al., 2015](#)).

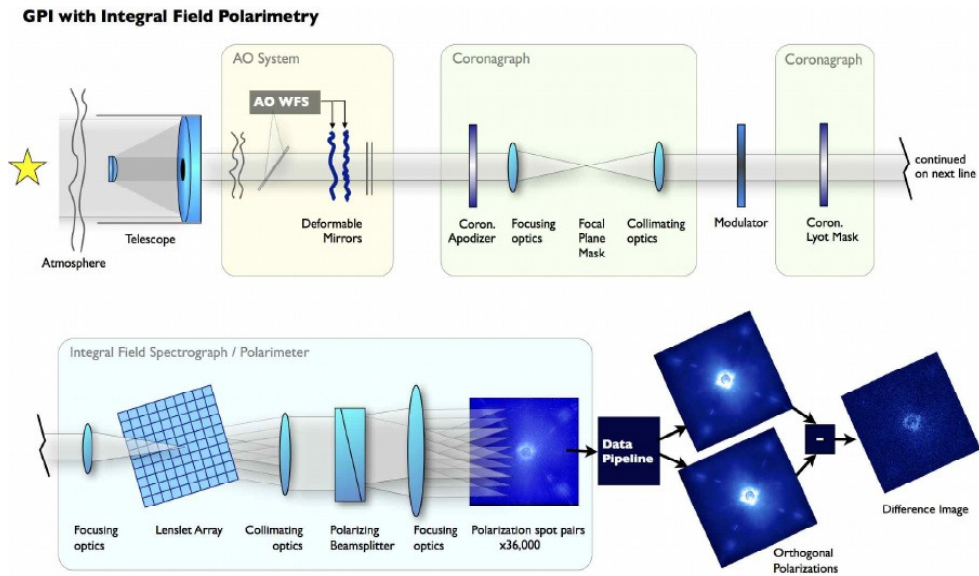


Figure 1.14 Schematic representation of GPI architecture for polarimetry observations (Perrin et al., 2015).

1.6 Observational Methods II: Polarimetry with High-contrast Imaging

1.6.1 Polarimetry with GPI: Polarization signal

High-resolution instruments like GPI allow to exploit the potential of polarimetry for PSF subtraction and to image faint debris disks. With inner working angles of 0.2 arcsec at 14.166 milliarcsec resolution, GPI allows to probe the inner regions of nearby systems up to nearly 10 AU, right into the location of the frost line for sun-like stars. We will focus on the most relevant features of this instrument as a preamble before introducing the flux calibration in polarimetry mode observations.

Spectroscopy and polarimetry observing modes of GPI share most of the optical architecture of this instrument. Spectroscopy observations are achieved with a disperser prism whereas in Polarimetry mode, a Wollaston prism is used separate the light into two orthogonal channels. Both prisms are located within the IFSD, located at the end of the optical path that leads light

to the detector. Figure 1.14 shows a simplified schematic representation of GPI design. Prisms are mounted onto two separate holders on top of a Prism Slide Mechanism where a main control interface is used to switch between them. In polarimetry mode, modulation is achieved with a half wave plate mounted in the Calibration Interferometer Enclosure, located before the Lyot Mask.

Operating as a dual-channel polarimeter, the Wollaston prism and the lenslet grid imprints a chessboard pattern in the science detector where each microlens PSF contains information of the orthogonal polarization states. There are currently two algorithms available to extract these PSFs and assemble a polarimetry cube (PODC). Each PODC file is $281 \times 281 \times 2$ with 2 disperser dimensions, one for each polarization channel.

With the requirements to observe exoplanets as one of the main science goals, GPI is fixed with respect to the telescope pupil. This means that the field of view is constantly rotating due to Earth's rotation, enabling techniques such as Angular Differential Imaging (ADI, [Marois et al., 2006](#)) to be used to significantly reduce the speckle halo. On the other hand, the rotation complicates the reduction steps in polarimetry, as the parallactic angle will be different across a sequence.

Equation 1.11 shows that the Stokes parameters will change as the field of view rotates with respect to the telescope pupil, hence images need to be rotated to a common frame of reference before attempting differential polarimetry. To overcome these difficulties, a set of Mueller matrices describing the optical architecture of GPI are used in a least square method to compute the polarization signals for each image. Following Section 1.4 and [Perrin et al. \(2015\)](#), we can write the Mueller matrix for GPI as the product of the following individual matrices:

$$\begin{aligned}
 M_{GPI}(\theta, \phi, \psi) = & M_{Woll\pm} M_{IFS} M_{Rot}(-\theta) \\
 & M_{WP}(\phi) M_{Rot}(\theta) \\
 & M_{AO-ter-tel} M_{sky}(\psi)
 \end{aligned}$$

where $M_{sky}(\psi)$ involves the parallactic angle ψ , $M_{AO-ter-tel}$ describes the reflections at the telescope primary and secondary mirrors, the tertiary fold, and reflections on the AO system DMs, $M_{Rot}(\theta)$ the rotations to the HWP, the $M_{HWP}(\phi)$ for the HWP at retardance ϕ , M_{IFS} deals with the entry to the IFSD and lastly $M_{Woll\pm}$ involves the Wollaston prism with the two polarization channels.

With a complete knowledge of M_{GPI} and N measurements, we can find the Stokes vector (I,Q,U,V) by solving

$$\mathbf{I} = \mathbf{M}_{GPI} \cdot \mathbf{S} \quad (1.22)$$

where \mathbf{S} is the Stokes Datacube. In this procedure, N observations from a science sequence are used after being rotated to match the same frame of reference in the sky. The Stokes Datacube can be transformed to the radial Stokes parameters $(I, Q, U, V) \rightarrow (I, Q_r, U_r, V)$. In this way, Q_r contains the linearly polarized flux at each pixel that is aligned perpendicular, $Q_r > 0$ or parallel, $Q_r < 0$ to the vector connecting that pixel to the central star. The term U_r holds the flux aligned at $\pm 45^\circ$, and since it is expected for scattered-induced polarization to be perpendicular to the scattering plane, all the flux should be contained in Q_r leaving U_r as a noise map. This is key for detecting faint optically-thin debris disks as stellar residual speckle halo will be effectively removed in differential polarimetric observations with GPI.

1.7 Questions for this Thesis

The morphology of debris disks relates to fundamental questions of planetary formation processes such as the evolution in time of the dust mass in disks, how planet and disks interact and the mechanisms of planetary formation as a whole. Characterizing debris disks is therefore of interest as they offer snapshots of the early evolutionary stages of planetary systems. As discussed above, detecting debris disks in scattered light is challenging and thus very specific techniques are required to accomplish this task. In this thesis, we probe these questions by studying the morphology of two debris disk with GPI PDI.

In Chapter 2, a new method to perform the photometric calibration of observations with GPI is presented. We developed a primitive in the GPI DRP to measure the stellar flux in GPI observations in polarimetry mode. This feature is part of the GPI DRP and became available to the GPI user community. Flux-calibrated polarimetry data is essential for debris disk characterization and it is used in the following debris disks studies presented here.

Chapter 3 comprises the study of the 5 Myr old HD 141569A transitional disk with GPI PDI and highlights the power of GPI in revealing the disk in polarimetry for the first time. We characterize the multi-ring architecture of this disk and reveal the existence of an spiral arm within 50 AU. We show how ray-tracing modeling can be used to infer the presence of yet another disk presently unseen in scattered light.

In Chapter 4 we study the $\gtrsim 1$ Gyr old 83 AU HD 157587 debris ring with multi band PDI with GPI. This disk is likely an old debris disk making it an excellent case of study as there is just a handful of such old disks. In this chapter we expanded previous work on this system by simultaneously fitting observations at *J*, *H* and *K1* filters with ray-tracing modeling. With an updated GAIA DR2 astrometry, we conclude that this unusually bright debris ring may be caused by an on-going collisional cascade.

We conclude this thesis in Chapter 5, where we provide a summary of the work presented here and briefly outline future work.

Bibliography

ALMA Partnership, Fomalont, E. B., Vlahakis, C., et al. 2015, ApJ, 808, L1

Armitage, P. J., & Valencia, D. 2010, Physics Today, 63, 63

Aumann, H. H., Gillett, F. C., Beichman, C. A., et al. 1984, ApJ, 278, L23

Backman, D. E., & Paresce, F. 1993, in Protostars and Planets III, ed. E. H. Levy & J. I. Lunine, 1253–1304

- Beckwith, S. V. W., Henning, T., & Nakagawa, Y. 2000, *Protostars and Planets IV*, 533
- Beuzit, J.-L., Feldt, M., Dohlen, K., et al. 2008, in *Proc. SPIE*, Vol. 7014, *Ground-based and Airborne Instrumentation for Astronomy II*, 701418
- Botke, W. F., Durda, D. D., Nesvorný, D., et al. 2005, *Icarus*, 175, 111
- Burns, J. A., Lamy, P. L., & Soter, S. 1979, *Icarus*, 40, 1
- Calvet, N., D'Alessio, P., Watson, D. M., et al. 2005, *ApJ*, 630, L185
- Chen, C. H., Sargent, B. A., Bohac, C., et al. 2006, *ApJS*, 166, 351
- De Rosa, R. J., Nielsen, E. L., Blunt, S. C., et al. 2015, *ApJ*, 814, L3
- Draine, B. T. 2006, *ApJ*, 636, 1114
- Duchêne, G., Arriaga, P., Wyatt, M., et al. 2014, *ApJ*, 784, 148
- Esposito, T. M., Duchêne, G., Kalas, P., et al. 2018, *AJ*, 156, 47
- Fried, D. L. 1966, *Journal of the Optical Society of America (1917-1983)*, 56, 1372
- Hartmann, J. 1900, *ApJ*, 11, 400
- Heney, L. G., & Greenstein, J. L. 1941, *ApJ*, 93, 70
- Hernández, J., Hartmann, L., Megeath, T., et al. 2007, *ApJ*, 662, 1067
- Hillenbrand, L. A., Carpenter, J. M., Kim, J. S., et al. 2008, *ApJ*, 677, 630
- Holland, W. S., Robson, E. I., Gear, W. K., et al. 1999, *MNRAS*, 303, 659
- Holland, W. S., Bintley, D., Chapin, E. L., et al. 2013, *MNRAS*, 430, 2513
- Hough, J. 2006, *Astronomy and Geophysics*, 47, 3.31
- Hung, L.-W., Duchêne, G., Arriaga, P., et al. 2015, *ApJ*, 815, L14

- Kalas, P. 2005, *ApJ*, 635, L169
- Kalas, P., Duchene, G., Fitzgerald, M. P., & Graham, J. R. 2007, *ApJ*, 671, L161
- Kalas, P. G., Rajan, A., Wang, J. J., et al. 2015, *ApJ*, 814, 32
- Kenyon, S. J., & Bromley, B. C. 2002, *AJ*, 123, 1757
- Kessler, M. F., Steinz, J. A., Anderegg, M. E., et al. 1996, *A&A*, 315, L27
- Lagrange, A.-M., Backman, D. E., & Artymowicz, P. 2000, *Protostars and Planets IV*, 639
- Lissauer, J. J. 1993, *ARA&A*, 31, 129
- Liu, M. C., Wahhaj, Z., Biller, B. A., et al. 2010, in *Proc. SPIE*, Vol. 7736, *Adaptive Optics Systems II*, 77361K
- Macintosh, B., Graham, J. R., Barman, T., et al. 2015, *Science*, 350, 64
- Macintosh, B. A., Graham, J. R., Palmer, D. W., et al. 2008, in *Proc. SPIE*, Vol. 7015, *Adaptive Optics Systems*, 701518
- Maire, J., Ingraham, P. J., De Rosa, R. J., et al. 2014, in *Proc. SPIE*, Vol. 9147, *Ground-based and Airborne Instrumentation for Astronomy V*, 914785
- Mannings, V., & Barlow, M. J. 1998, *ApJ*, 497, 330
- Marois, C., Lafrenière, D., Doyon, R., Macintosh, B., & Nadeau, D. 2006, *ApJ*, 641, 556
- Morbidelli, A., Tsiganis, K., Crida, A., Levison, H. F., & Gomes, R. 2007, *AJ*, 134, 1790
- Morzinski, K. M., Close, L. M., Males, J. R., et al. 2014, in *Proc. SPIE*, Vol. 9148, *Adaptive Optics Systems IV*, 914804
- Murakami, H., Baba, H., Barthel, P., et al. 2007, *PASJ*, 59, S369
- Murakawa, K., Suto, H., Tamura, M., et al. 2004, *PASJ*, 56, 509

- Oppenheimer, B. R., Golimowski, D. A., Kulkarni, S. R., et al. 2001, *AJ*, 121, 2189
- Oudmaijer, R. D., van der Veen, W. E. C. J., Waters, L. B. F. M., et al. 1992, *A&AS*, 96, 625
- Patel, R. I., Metchev, S. A., & Heinze, A. 2014, *VizieR Online Data Catalog*, 221
- Perrin, M. D., Duchene, G., Graham, J. R., et al. 2009a, in *American Institute of Physics Conference Series*, Vol. 1158, *American Institute of Physics Conference Series*, ed. T. Usuda, M. Tamura, & M. Ishii, 17–22
- Perrin, M. D., Schneider, G., Duchene, G., et al. 2009b, *ApJ*, 707, L132
- Perrin, M. D., Duchene, G., Millar-Blanchaer, M., et al. 2015, *ApJ*, 799, 182
- Pilbratt, G. L., Riedinger, J. R., Passvogel, T., et al. 2010, *A&A*, 518, L1
- Robertson, H. P. 1937, *MNRAS*, 97, 423
- Rodenhuis, M., Canovas, H., Jeffers, S. V., et al. 2012, in *Proc. SPIE*, Vol. 8446, *Ground-based and Airborne Instrumentation for Astronomy IV*, 84469I
- Semenov, D., Henning, T., Helling, C., Ilgner, M., & Sedlmayr, E. 2003, *A&A*, 410, 611
- Shack, R. V. 1971, *J. Opt. Soc. Am.*, 61, 648
- Sicilia-Aguilar, A., Hartmann, L., Calvet, N., et al. 2006, *ApJ*, 638, 897
- Sivaramakrishnan, A., Koresko, C. D., Makidon, R. B., Berkefeld, T., & Kuchner, M. J. 2001, *ApJ*, 552, 397
- Smith, B. A., & Terrile, R. J. 1984, *Science*, 226, 1421
- Suzuki, R., Kudo, T., Hashimoto, J., et al. 2010, in *Proc. SPIE*, Vol. 7735, *Ground-based and Airborne Instrumentation for Astronomy III*, 773530
- Tinbergen, J. 1996, *Astronomical Polarimetry*, 174

- Wang, J. J., Rajan, A., Graham, J. R., et al. 2014, in Proc. SPIE, Vol. 9147, Ground-based and Airborne Instrumentation for Astronomy V, 914755
- Werner, M. W., Roellig, T. L., Low, F. J., et al. 2004, ApJS, 154, 1
- Williams, J. P., & Andrews, S. M. 2006, ApJ, 653, 1480
- Wood, J. A. 1988, Annual Review of Earth and Planetary Sciences, 16, 53
- Wright, E. L., Eisenhardt, P. R. M., Mainzer, A. K., et al. 2010, AJ, 140, 1868
- Wyatt, M. C. 2008, ARA&A, 46, 339
- Wyatt, M. C., Greaves, J. S., Dent, W. R. F., & Coulson, I. M. 2005, ApJ, 620, 492
- Zuckerman, B., & Song, I. 2004, ARA&A, 42, 685

Chapter 2

Gemini planet imager observational calibration XII: photometric calibration in the polarimetry mode

A version of this manuscript was published as Hung, Bruzzone et al. (2016, SPIE, 9908, 99083A)

The Gemini Planet Imager (GPI) is a high-contrast instrument specially designed for direct imaging and spectroscopy of exoplanets and debris disks. GPI can also operate as a dual-channel integral field polarimeter. The instrument primarily operates in a coronagraphic mode which poses an obstacle for traditional photometric calibrations since the majority of on-axis starlight is blocked. To enable accurate photometry relative to the occulted central star, a diffractive grid in a pupil plane is used to create a set of faint copies, named satellite spots, of the occulted star at specified locations and relative intensities in the field of view. We describe the method we developed to perform the photometric calibration of coronagraphic observations in polarimetry mode using these fiducial satellite spots. With the currently available data, we constrain the calibration uncertainty to be $< 13\%$, but the actual calibration uncertainty is likely to be lower. We develop the associated calibration scripts in the GPI Data Reduction Pipeline,

which is available to the public. For testing, we use it to photometrically calibrate the HD 19467 B and β Pic b data sets taken in the H -band polarimetry mode. We measure the calibrated flux of HD 19467 B and β Pic b to be 0.078 ± 0.011 mJy and 4.87 ± 0.73 mJy, both agreeing with other measurements found in the literature. Finally, we explore an alternative method which performs the calibration by scaling the photometry in polarimetry mode to the photometrically calibrated response in spectroscopy mode. By comparing the reduced observations in raw units, we find that observations in polarimetry mode are 1.03 ± 0.01 brighter than those in spectroscopy mode.

2.1 Introduction

In less than two years of its regular operations, the high-contrast instrument Gemini Planet Imager (GPI, [Macintosh et al., 2014](#)) has discovered a new exoplanet ([Macintosh et al., 2015](#)) and numerous resolved debris disks ([Currie et al., 2015](#); [Hung et al., 2015a](#)). GPI, specially designed for direct imaging and spectroscopy of exoplanets and debris disks, can also operate as a dual-channel integral field polarimeter. The instrument primarily operates with a coronagraph in place, enabling high-contrast observations at inner working angles as low as $0''.15$. Traditional coronagraphy, however, poses an obstacle for photometric calibrations since the majority of the on-axis starlight is blocked. To photometrically calibrate images in the polarimetry mode with a coronagraph in place, we present two methods that do not rely on directly measuring the stellar flux.

Satellite spots provide a means for accurate photometry and astrometry relative to the occulted central star. Satellite spots are a set of faint copies of the occulted star created by a diffractive grid superimposed on the apodizer in the pupil plane ([Sivaramakrishnan & Oppenheimer, 2006](#); [Wang et al., 2014](#)). These satellite spots have fixed relative intensities compared to the central star and fall at specified locations in the field of view. Photometric and astrometric calibration of coronagraphic observations in spectroscopy mode have been developed using

these fiducial satellite spots (Wang et al., 2014; Maire et al., 2014). This method is currently the predominant way to calibrate spectroscopic observations of GPI. A major difference is that in polarimetry mode, the satellite spots are not diffraction-limited PSFs but are smeared out radially into rod shapes due to their chromaticity. Therefore, although this calibration method is based on the same principle as what is currently being used in spectroscopy mode, a separate set of data processing procedures is needed for performing the photometric calibration on broadband polarimetric images instead of spectral cubes. Here we present two methods we developed to perform the photometric calibration of coronagraphic observations in polarimetry mode. The first method relies on using the satellite spots directly, using a procedure analogous to what is done in spectroscopy mode. The second method relies on scaling the observations in polarimetry mode to the photometrically calibrated response in spectroscopy mode. Both of these methods directly or indirectly use the satellite spots. An advantage for using the first method is that it can be applied to the science images in polarimetry mode directly; this method does not rely on any additional images for calibration. The second method will be convenient for users who already have calibrated images of the same target in spectroscopic mode. When applicable, using both methods on the same data set can offer a consistency check on the photometric calibration processes and potentially get more precise calibrated products. In this report, we first describe how we measure the flux of the satellite spots through aperture photometry in Sec. 2. Then, we present the method and characterize the uncertainty for performing the photometric calibration of coronagraphic observations in polarimetry mode directly using the satellite spots in Sec. 3. Next, we explore an alternative calibration method through characterizing the flux ratio between the polarimetry and spectroscopy observing modes in Sec. 4. Finally, we summarize our findings and propose how we might lower the calibration uncertainty with future observations in Sec. 5.

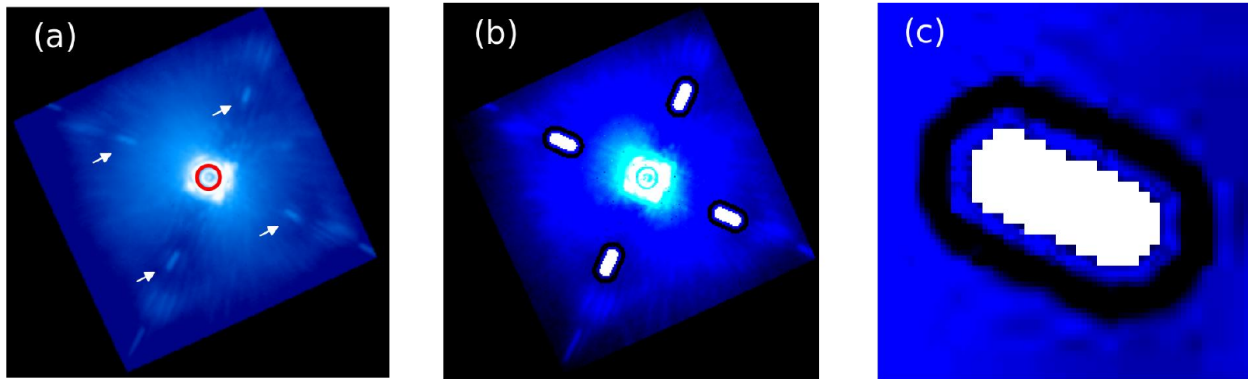


Figure 2.1 Reduced H -band images of HD 118666 observed with the coronagraph in polarimetry mode. (a) The red circle indicates the position and the size of the focal plane mask. The white arrows point to the satellite spots from the first-order diffraction. The satellite spots are smeared out radially into rod shapes due to their scaling with λ/D over the filter bandpass. (b) The white solid patches show the apertures used for measuring the flux of the satellite spots. The narrow black regions around the white apertures are used to estimate the background noise. (c) An enlarged view of the apertures used for the satellite spot (white) and for the background (black).

2.2 Satellite Spot Flux Measurement in Polarimetry Mode

To measure the fluxes of the satellite spots in images taken with the coronagraph in polarimetry mode, we first need to reduce the images. The raw polarimetry data were reduced using the GPI Data Reduction Pipeline (DRP, Perrin et al., 2014). Polarimetry data were dark subtracted, cleaned for correlated noise (Ingraham et al., 2014) interpolated over bad pixels in the two-dimensional (2D) detector image, corrected for flexure (Draper et al., 2014), assembled into data cubes with the third dimension comprising the two orthogonal polarization states, and divided by a low spatial frequency polarized flat field. The default unit for the reduced data cubes is in analog-to-digital Unit (ADU) coadd¹. Fig. 2.1 (a) shows an example of a reduced polarimetry image. The satellite spots and the focal plane mask are marked by white arrows and a red circle. To extract the position and the flux of the satellite spots, we develop the primitive Measure Satellite Spot Flux in Polarimetry in the GPI DRP, and we describe the methodology below and the application in Sec. 3.3. We determine the location of the satellite spots in the field of view according to the known diffraction properties of the pupil plane

grating. The stars position is measured through the DRP primitive Measure Star Position for Polarimetry using a Radon transform-based technique (Wang et al., 2014) which makes use of the satellite spots but does not directly output their positions. With the stars position known, the radial position of the satellite spots at a particular wavelength λ will fall at an angular distance of λ/d relative to the occulted star, where d is the distance between the grid lines imprinted on the apodizer. In polarimetry mode, the satellite spots are not diffraction-limited PSFs but are smeared out radially into rod shapes due to their wavelength dependence and the broadband nature of the polarimetry mode. We determine the radial extent of the satellite spots by considering the band pass of the filter in use. The azimuthal position of the satellite spots is determined by measuring the mean angular position of satellite spots from a collection of the observed targets in spectral mode. Next, we use aperture photometry with background subtraction to measure the flux of the satellite spots. Fig. 2.1 (b) shows the apertures used for measuring the source flux (white patches) and for measuring the background (narrow black regions around the white apertures). The satellite-spot aperture consists of a rectangle capped with semi-circles on each end of the long axis. The length of the rectangle is defined by the satellite spot positions at the minimum and maximum wavelengths of the observed band. The radius of the semicircle (half the width of the rectangle) is chosen to be slightly greater than the FWHM of the satellite spots in spectral mode. In the example H-band image, the length of the rectangle corresponds to 12 pixels, and the radius of the semicircle is chosen to be 4 pixels. To measure the background, we use a region that resembles a racetrack constructed using the annulus formed by two concentric but larger versions of the source aperture. For both the inner bound and outer bound of the racetrack, the length of the rectangle is still 12 pixels, but the radii of the end caps are 6 and 9 pixels for the inner and outer bounds of the annulus respectively. This aperture setting is referred as the [4,6,9] default setting later in the paper. We then apply the background correction to our measured flux of satellite spots.

2.3 Calibration Using the Satellite Spots Directly

2.3.1 Calibration Method

We take advantage of the well characterized satellite spot-to-star flux ratios to perform photometric calibration on the polarimetry data. This method is first described briefly in (Hung et al., 2015b), and here we provide a more detailed description. We can convert a reduced image D_i from the default unit in ADU coadd¹ into an image D_f with a physical unit (i.e., Jy) using

$$D_f = D_i \frac{RF_*}{S}, \quad (2.1)$$

where R , F_* , and S are the satellite spot-to-star flux ratio, the stellar flux in physical units (i.e., Jy), and the average flux of satellite spots in ADU coadd¹ respectively.

The satellite spot-to-star flux ratio depends on the specification of the apodizer used. The H-band measurements of the ratio and the corresponding magnitude difference are made with a combination of lab tests and the on-sky observations taken from the commission runs. When using the apodizers designed for Y , J , H , $K1$, and $K2$, a star will be ~ 5000 times brighter than the average brightness of its four satellite spots. The current best-estimated values for all apodizers are stored in the `apodizer_spec.txt` file which is included in the GPI DRP package for users to download. The stellar flux, F_* , is the flux, in a physical unit, of the central star observed through the filter. In the following study, we adopt the F_* values from Two Micron All-Sky Survey (2MASS) observations. Corrections between 2MASS and GPI magnitudes in J and H filters were found to be negligible (Macintosh et al., 2015). The average satellite spot flux S can be found by taking the mean of the four satellite spot fluxes measured using the method described in Sec. 2.

2.3.2 Calibration Uncertainty

Here we characterize the uncertainty associated with this calibration method. High-contrast imaging in scattered light often suffers from speckle noise. These speckles can affect the accuracy of photometric measurements and therefore introduce some systematic errors during the calibration process. It is well known that AO photometry is challenging and is subject to systematic biases due to the time-variable atmosphere (Lu et al., 2010). The variability in AO performance (Poyneer et al., 2014) can also affect the photometric calibration accuracy. To estimate the calibration uncertainty, we analyze the following data sets where a primary star and a companion are imaged in the same exposure with the primary star placed behind the occulter.

We estimate the GPI photometric calibration uncertainty in polarimetry mode by measuring the scatter of the flux ratio of the companion to the satellite spot. This scatter contains the uncertainty σ_R associated with the satellite spot-to-star flux ratio R described in Equation 2.1. This uncertainty should also capture the intrinsic variability of the satellite spots from them being coherent with the speckle noise. In spectroscopy mode, this intrinsic variability is estimated to be $\sim 7\%$ (Wang et al., 2014). Ideally, to measure σ_R with the on-sky data, we would measure the scatter of R over a series of exposures. However, since the observed star is placed behind the mask, it prevents us from measuring the stellar flux and satellite spot flux simultaneously. To get around this problem, we measure the companions flux and the average satellite spot flux in each image instead. We then compute the scatter of the companion-to-satellite spot flux ratio over a series of images. This approximation approach also provides us the advantage for capturing the uncertainty caused by speckle noise. GPI uses the angular differential imaging technique so the sky will appear to rotate in the field of view as a function of time. The speckles, on the other hand, do not rotate with respect to the field of view. Therefore, over a period of time, the companion could rotate in and out of the static speckles and provide a more complete characterization by capturing the uncertainties caused by speckle noise.

We use the existing data set on HD 19467 system to estimate the GPI photometric calibration uncertainty. The system hosts a T5.5 brown dwarf companion, HD 19467 B, at the

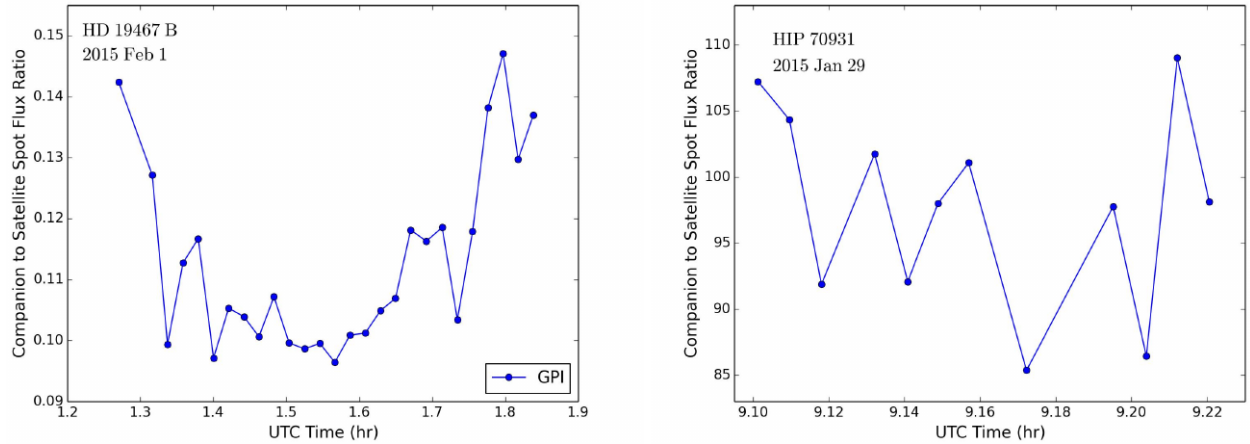


Figure 2.2 Left: Companion-to-satellite spot flux ratio of HD 19467. The blue dots are the GPI H-band measurements in polarimetry mode from this study. The flux ratio of the companion (HD 19467 B) to the average satellite spot is plotted for each image for the entire sequence. We estimate the GPI photometric calibration uncertainty in polarimetry mode to be 13% according to the scatter of this ratio. Right: Companion-to-satellite spot flux ratio of HIP 70931. The scatter of this ratio indicates the GPI photometric calibration uncertainty in polarimetry mode could be $< 7.5\%$. However, we note that this measurement might be corrupted since the companion in this data set is too bright that it falls on the nonlinear regime of the detector response.

separation of $\sim 1''.65$ from the primary G3V star (Crepp et al., 2014). On February 1, 2015, we obtained twenty-seven 60 seconds images of HD 19467 with GPI in the H – band polarimetry mode with the primary purpose of studying the polarization signal from the companion (Jensen-Clem et al., 2016). The coronagraph was placed to block the primary star. Polarized signal was not detected from that study, suggesting it is possible that the T-dwarf is cloudless or has the clouds distributed symmetrically with respect to the viewing angles. Since most of the variability in brown dwarfs is thought to be caused by the time variation of the cloud distribution, the null detection in polarized signal implies that the source is likely to be not highly variable. Here we use the same data set to study the photometric calibration uncertainty assuming the source is not variable.

Using the HD 19467 data set, we estimate the GPI photometric calibration uncertainty in polarimetry mode to be $< 13\%$, with the limitation coming from the variation in the photometry of the companion. We measure the average flux of the satellite spots in each image as described

in Sec. 2. To measure the flux of the companion, we use a circular aperture with a radius of 4 pixels. We then subtract the background estimated through the surrounding circular region between the inner and outer radii of 6 and 9 pixels. These aperture parameters are chosen to match the ones used for doing the photometry on the satellite spots. Fig. 2.2 shows the flux ratio measured in each image. Based on the scatter of the flux ratio of the companion to the average satellite spot for each image, we arrive at the same estimate for the GPI photometric calibration uncertainty found before. The current dominant source of error for estimating the calibration uncertainty comes from the photometry of the companion. Compared to the satellite spots, the companion is dimmer and suffers from the lower S/N. Although the photon noise for each measurement of the companion is only $\sim 1.3\%$, the flux measurements have variations of $\sim 12\%$ due to speckle noise. The effect of correlations can be clearly seen in Fig. 2.2. This uncertainty of the companion flux measurement is similar to the one estimated based on a ring of apertures around the parent star at the same separation as the companion in the Stokes I frame (Jensen-Clem et al., 2016). Compared to the $\sim 2\%$ variation of the average flux of the satellite spots, the flux variation of the companion is much higher. This large variation of the companion flux significantly affects the precision of measuring the companion-to-satellite spot flux ratio.

We examine another data set, HIP 70931, in hope to better constrain the calibration uncertainty. HIP 70931 is an A1V star with a companion at $\sim 0''.60$ (De Rosa et al., 2014). On January 1, 2015, we obtained twelve 15 second H -band images of HIP 70931 with the coronagraph in polarimetry mode using GPI. The companion in this system is much brighter and provides higher S/N. We process the data set the same way as described above and plot the companion-to-satellite spot flux ratio in Fig. 2.2. This data set indicates the calibration uncertainty is 7.5% . However, although not saturated, the companion is so bright that it falls on the nonlinear regime ($> 16,000$ ADU (Ingraham et al., 2014)) of the detector response. The sensitivity of a given pixel as a function of its filled well depth has not yet been fully characterized, and there is currently no primitive to apply a non-linearity correction in the pipeline.

The detector is linear to within $\sim 5\%$ over its entire range before it is saturated (private communication with Jeffrey Chilcote). Since the uncertainty caused by the nonlinear response of the detector could be non-negligible compared to the calibration uncertainty estimated from the HIP 70931 data set, we note that we conservatively adopt the upper limit of 13% measured from the HD 19467 data set as the photometric calibration uncertainty in the GPI polarimetry mode.

2.3.3 GPI Data Reduction Pipeline Implementations

We developed the primitives in the GPI DRP to perform photometric calibration in polarimetry mode. Users should first reduce the raw images into polarimetric data cubes with the star position measured, which can be done using the recipe Simple Polarization Datacube Extraction. Then, users can apply the Measure Satellite Spot Flux in Polarimetry primitive to extract the flux of the satellite spots. These measured values will then be stored in the header extension 1. Next, users can use the Calibrate Photometric Flux in Pol Mode primitive to convert the raw units in the reduced images to physical units. This primitive can be applied to the individual reduced files or the final Stokes cube. These primitives are available for users with the DRP version of 1.4.0 or newer (Perrin et al., 2016). A tutorial with examples is created on the GPI Data Pipeline Documentation website¹ to guide the users through a typical reduction.

2.3.4 Photometry of HD 19467 B

We examine the accuracy of our photometric calibration by comparing our photometrically calibrated brightness of HD 19467 B to the published value from an independent study. We first calibrate our data and perform aperture photometry with background subtraction as described in Sec. 3.2. No aperture correction is needed since the aperture setting used for the companion matches the one used for the satellite spots. Our GPI photometry measurements for each individual frames are plotted in Fig. 3. Using these simple aperture photometry values, we

¹<http://docs.planetimager.org/pipeline/>

measure the H -band brightness of HD 19467 B to be 0.078 ± 0.011 mJy, which is consistent with the published NIRC2 measurement of 0.0708 ± 0.0086 mJy (Crepp et al., 2014). The uncertainty σ_C of the companion flux C is calculated using the following equation:

$$\sigma_C = C \sqrt{\left(\frac{\sigma_I}{I}\right)^2 + \left(\frac{\sigma_R}{R}\right)^2 + \left(\frac{\sigma_S}{S}\right)^2 + \left(\frac{\sigma_{F_*}}{F_*}\right)^2}, \quad (2.2)$$

where I is the average of the measured brightness of the companion. σ_I can be characterized by dividing the scatter of I by \sqrt{n} , where n is the number of frames. The fractional uncertainty of I in this case is 2.3%. The dominant source of error comes from the term σ_R/R , where it represents the 13% calibration uncertainty upper limit as found in Sec. 3.2. We calculate σ_{F_*}/F_* using the 2MASS H -band stellar magnitude of 5.447 ± 0.036 (Cutri et al., 2003). The term σ_S is calculated by dividing the scatter of S by \sqrt{n} , and the term gives less than 1% of fractional uncertainty. Here we assume all sources of errors are independent but we note that this could cause us to overestimate the overall uncertainty σ_C , since currently both σ_I and σ_R are affected by the precision of the companion photometry. In Sec. 5 we discuss some future improvements that can be made to disentangle the uncertainties.

2.3.5 Photometry of Beta Pictoris b

We observed Pictoris b in polarimetry mode with the coronagraph in H band using GPI. The observations were taken on 2013 December 12 for the AO performance and optimization tests. We obtained forty-nine 60 second frames with waveplate angles rotating between 0° , $22^\circ.5$, 45° , and $67^\circ.5$. The total accumulated field rotation is 91° . The morphology of the debris disk and orbit of the planet has been studied in a great detail from these observations (Millar-Blanchaer et al., 2015). Here we reduce raw data and then use the photometric calibration primitives with the default [4,6,9] aperture setting to convert each image from the raw unit to a physical unit following the steps described in Sec. 3.3.

We perform the simple aperture photometry with background subtraction to measure the

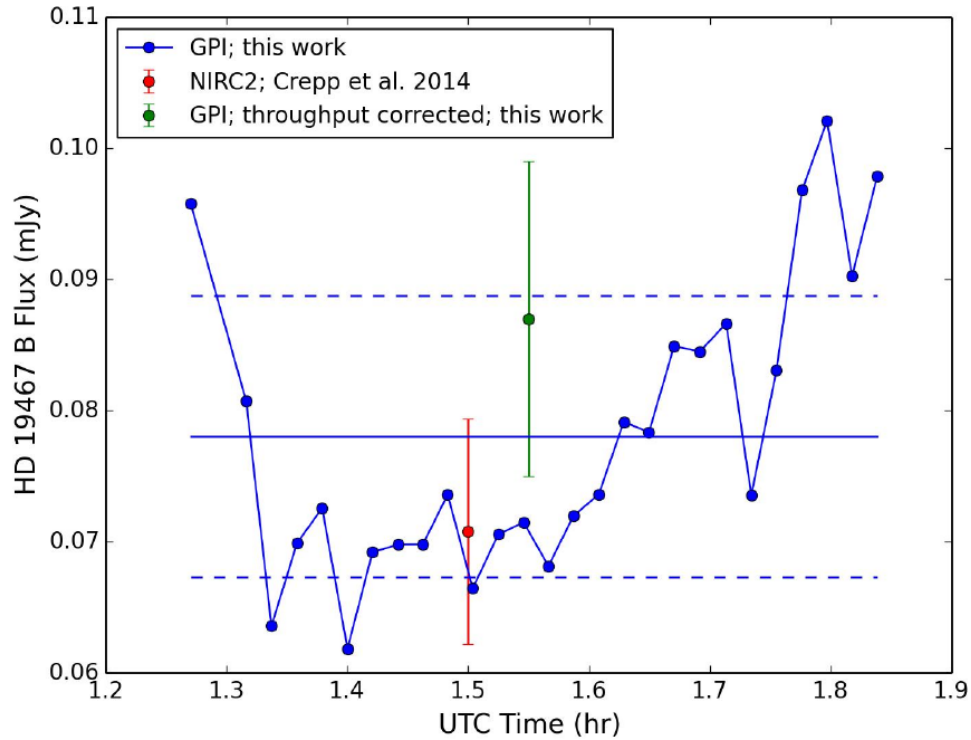


Figure 2.3 Photometrically calibrated measurements of HD 19467 B observations. The blue dots are the GPI H -band measurements in polarimetry mode from this study. The mean and the $1 - \sigma$ of the GPI measurements are presented as a solid and dash lines. The green point represents the detection throughput-corrected value. The throughput correction is not necessary for this data (see Sec. 3.6 for a detailed discussion). Our GPI measurements are consistent with the photometric measurement from NIRC2 at the Keck observatory (Crepp et al., 2014).

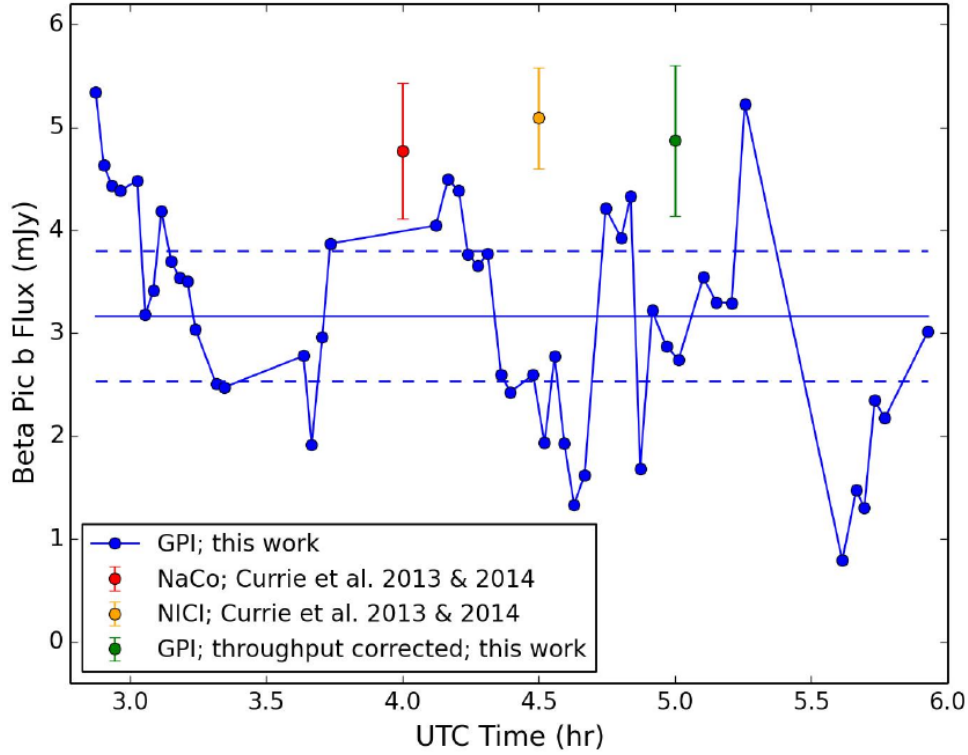


Figure 2.4 H -band photometry of β Pictoris b. The GPI data were taken on 2013 December 12. The blue points are the photometry measurement of the individual frames using the default aperture setting of [4,6,9] pixels in the GPI DRP. The horizontal lines represent the mean and 1σ values of the blue points.

brightness of β Pic b using the same procedures as described in Sec. 3.4. Our GPI photometry measurements for each individual frames are plotted in Fig. 4. Using these simple aperture photometry values, we measure the H -band brightness of β Pic b to be 3.17 ± 0.63 mJy, which is represented as the horizontal lines in Fig. 2.4. The uncertainty of our measurement is calculated using Equation 2.2. The fractional uncertainty of I in this case is 15%, and the term σ_R/R is set to be 13%. These first two terms are the dominant sources of error here. Since these two terms are not completely independent (as discussed in Sec. 3.4), the actual combined uncertainty could be smaller than what we estimate here. We calculate σ_{F_*}/F_* using the H -band stellar magnitude of 3.499 ± 0.007 (Morzinski et al., 2015). Each of the last two terms in the equation has less than 1% of fractional uncertainty.

The simple GPI photometry measurements seem to underestimate the flux of β Pic b when

compared to the values found in the literature. The VLT/NaCo (red point in Fig.2.4 and Gemini/NICI (yellow point) H -band measurements show that β Pic b has Δm of 9.83 ± 0.14 and 9.76 ± 0.18 (Morzinski et al., 2015; Currie et al., 2013) corresponding to the flux of $\sim 4.77 \pm 0.66$ and 5.09 ± 0.49 mJy. Our GPI measurement of 3.17 ± 0.63 mJy is inconsistent with these published values. We suspect that our measurements are suffering from the over estimated background values. The planets PSF is bright and extended, and the first airy ring can be seen in each image. A significant portion of the first airy ring overlaps with the background aperture, causing the over-estimated background value. To overcome this problem, we perform the following analysis to correct the detection throughput.

2.3.6 Detection throughput Correction

Our throughput corrected GPI flux measurement of β Pic b in H band is 4.87 ± 0.73 mJy, which agrees with other measurements found in the literature. As mentioned above, our simple photometry measurements seem to overestimate the background flux due to the overlap between the background aperture and the bright airy ring. Accurately measuring the background using the nearby region is difficult since the stellar halo light and speckles make the stellar PSF to have high spatial variations at this separation. Therefore, instead of trying to accurately characterize the background, we inject and then recover artificial point sources in the nearby regions to correct for the detection throughput. We extract the point source PSF from one of the stars in Theta Ori B using the data set taken in H band on January 31, 2015. We inject point-source PSFs with the same planet-star separation but at the position angles of $\pm 35^\circ$ from β Pic b in each frame. This position angle offset is selected to allow the PSF to be injected closest to the real planet but still have the non-overlapping apertures between to real and injected sources. We then use the aperture photometry to measure the brightness of the injected sources using the same aperture setting as what is used on β Pic b. We find that in order to have our averaged detected flux of the injected source to match that of the β Pic b, the injected source has to be 4.87 ± 0.73 mJy. We estimate the error by determining the range of the injected flux need to

match the error range of the uncorrected flux. This detection throughput corrected value agrees with other measurements from the literature, and this photometric calibration study showcases the performance of the method developed in this paper.

The detection throughput correction is not necessary for the photometry measurement of HD 19467 B. We perform the same correction process for this system except for injecting the artificial source at 90° (instead of $\pm 35^\circ$) away from the companion to keep it inside the field of view. The throughput-corrected value is 0.087 ± 0.012 mJy (green point in Fig. 2.3), which is consistent with the original value from the simple aperture photometry. With its diffraction rings buried in the background, we show that the detection throughput correction for our HD 19467 data set is not necessary.

We note that this detection throughput correction might be needed only when performing aperture photometry; it is not a problem of the flux calibration itself. This detection throughput analysis is mainly correcting for the errors from the background subtraction process when doing aperture photometry. As demonstrated above, not all photometry cases will need it; it is only necessary for the cases where getting the accurate background estimate is difficult while doing aperture photometry. For data sets with disks instead of planets, there is no need for a throughput correction for the disk surface brightness since no aperture photometry is involved. In addition, since disks are usually much more extended than a point source PSF, the surface brightness of a disk is less sensitive to the smearing effect of the PSF comparing to the point sources.

2.4 Calibration Using Spectroscopic Observations

Here we present an alternative approach to perform the photometric calibration. This method can be used on polarimetric data sets for targets which also have spectroscopic observations with GPI. This method works under the assumption that the data quality from the two modes is similar. Instead of calibrating using the satellite spots directly, this calibration method works

through scaling the polarimetric observations to the calibrated observations in spectroscopy mode.

2.4.1 Calibration Method

This method depends on two things: the photometric calibration in spectroscopy mode and the flux ratio between the reduced images in polarimetry and spectroscopy modes. The principle of this calibration method can be explained using the following equation:

$$D_f = D_i \times \frac{RF_{*,\text{spec}}}{S_{\text{spec}}} \times \frac{1}{P}, \quad (2.3)$$

where $F_{*,\text{spec}}$ is the host star spectrum, S_{spec} is the average satellite spot spectrum, and P is the polarimetry to-spectroscopy flux ratio. The photometric calibration in spectroscopy mode (Maire et al., 2014) has been developed for determining the first fraction in Equation 2.3. This process uses the satellite spots and is based on the same principle as in Sec. 3. For calibrating the spectral data cubes, the spectra $F_{*,\text{spec}}$ and S_{spec} are used instead of the broadband F_* and S fluxes. The corresponding reduction primitives and recipes are available in the GPI DRP². The photometric calibration process in spectroscopy mode will provide the conversion factor necessary for transforming the images in raw units to physical units.

Characterizing the second component, the polarimetry-to-spectroscopy flux ratio P , enables the meaningful comparison between the reduced images taken in these two modes. This characterization is necessary due to the potential difference stemming from different throughput and reduction processes between these two modes. Ideally, with the same integration time on the same target, we expect the total raw counts to be the same in spectroscopy and polarimetry modes. However, the light path in polarimetry mode is slightly different from the one in spectroscopy mode. For example, the polarimetry mode uses the half-wave plate and the Wollaston prism instead of the spectral prism. The difference in the light path can introduce some

²http://docs.planetimager.org/pipeline/usage/tutorial_spectrophotometry.html

small differences in throughput. In addition, different pipeline primitives are used to reduce the raw data due to the nature of the actions needed to extract the information from the raw images. This post processing process can also introduce some variations in the reduced images between the two modes. We provide a detailed discussion about estimating the value of P in the following section.

2.4.2 Scaling Factor

There are two extraction methods, BOX and PSF, available to assemble polarimetric data cubes in the GPI DRP (Millar-Blanchaer et al., 2016). The BOX method implements a 5×5 box centered at each polarimetry spot while the PSF method uses the empirically calibrated subpixel lenslet PSF model. Given the same input raw file, these two methods produce the data cubes with similar signal-to-noise ratio. However, the BOX method seems to produce polarimetric data cubes that are unexpectedly brighter than spectroscopic observations, making using this method less favorable. The extraction algorithm used for reducing the polarimetric data is therefore set to be the PSF option in this study. The PSF algorithm is also the default standard mode for reducing data in all pipeline recipe templates.

We examine this scaling factor between the reduced polarimetric and the spectroscopic images by comparing the flux of their satellite spots. The reduced polarimetric and spectroscopic cubes were collapsed to form the 2D broadband total intensity images. In the collapsed images, the satellite spots in the spectroscopic images become smeared, having the same rod-like appearance as the satellite spots in polarimetry mode. We then use the process described in Sec. 2 to perform the photometry of the satellite spots with the default aperture size setting of [4, 6, 9] in H band. Next, we compute the total flux of satellite spots for each image and then average over the sequence of images. These two mean values are then compared to measure the brightness ratio in polarimetry to spectroscopy mode. These calculations are all done in units of ADU. Table 2.1 lists the ratios we measured for eleven different targets. The weighted average of this ratio indicates the satellite spots in polarimetry mode are 1.02 ± 0.02 times

Name	Ratio	σ
49 Cet	1.11	0.09
ϵ Eri	1.09	0.09
V435 Car	0.99	0.05
HD 31392	1.10	0.13
γ Dor	1.11	0.26
γ Ophi	1.09	0.07
HD 74576	1.05	0.09
HD 826	0.97	0.11
HR 6948	1.05	0.10
HD 19467	0.98	0.05
HIP 70931 (March 2014)	1.07	0.08
HIP 70931 (Jan 2015)	1.02	0.06

Table 2.1: Satellite spot flux ratio of polarimetry to spectroscopy modes among eleven science targets observed in both modes with GPI. The uncertainty represents the standard deviation of the measurements.

Name	Ratio	σ
HD 19467 B	1.07	0.43
HIP 70931 B (March 2014)	1.06	0.02
HOP 70931 B (Jan 2015)	1.02	0.01

Table 2.2: Ratio of companion fluxes in polarimetry to spectroscopy modes. The uncertainty represents the standard deviation of the measurements.

brighter than the ones in spectroscopy mode.

Applying the same technique to the flux of the companion, HIP 70931 B, also provides the consistent result that the polarimetric images are slightly brighter than the spectroscopic images. In the data sets we examined earlier, HD 19467 and HIP 70931 each has a companion. Unlike the satellite spots, the companions in the collapsed 2D images still retain their point-source-like PSFs. We perform the aperture photometry on the companions and compare their brightness ratios in polarimetry to spectroscopy mode. The result is summarized in Table 2.2. The weighted average of this flux ratio is 1.03 ± 0.01 . This ratio, derived from comparing the flux of the companions, is consistent with the one derived using the satellite spots. We note that this result indicates the effect is either due to the difference in throughput or in datacube

extraction, not due to the way we measure the satellite spot flux.

2.5 Summary and Future Work

In this paper, we present the newly developed methods for performing photometric calibration of GPI coronagraphic data taken in polarimetry mode. Photometrically calibrating these images relies on using the satellite spots. We develop a new primitive in the GPI DRP (version 1.4.0 or newer) for measuring the flux of the satellite spots in polarimetry mode with aperture photometry. The first calibration method we present here uses the satellite spots directly. The principle of this method is based on computing the unit converting factor from the known satellite spot-to-star flux ratio, the known stellar flux in a physical unit, and the measured average flux of the satellite spots. With the current available data, we can constrain the associated photometric calibration uncertainty to be $< 13\%$. We use this method to photometrically calibrate the H -band polarimetric observations of HD 19467 B and β Pic b. Then we measure the calibrated flux of HD 19467 B and β Pic b to be 0.078 ± 0.011 and 4.87 ± 0.73 mJy respectively. Both of these measurements agree with other values found in the literature, showing that the photometric calibration method we develop here can produce consistent results with other observations. Finally, we present an alternative photometric calibration method. This calibration method works through scaling the polarimetric observations to the calibrated observations in spectroscopy mode. By comparing the observations in polarimetry to spectroscopy mode, we find that this scaling factor is 1.03 ± 0.01 , with the observations in polarimetry mode being brighter.

To lower the calibration uncertainty, higher S/N observations of a star-companion system are needed. The current upper limit for the photometric calibration uncertainty is 13% when using the satellite spots to photometrically calibrate the GPI coronagraphic observations in polarimetry mode. The current dominant source of error for estimating this calibration uncertainty comes from the photometry of the companion. Observing HD 8049 in polarimetry mode

might provide a better constraint to lower this calibration uncertainty. HD 8049 is a K2V star with a white dwarf companion (Zurlo et al., 2013). The flux ratio of this star-companion is ideal since we can expect to get good S/N ratio of the companion in a reasonable exposure time (~ 60 s) and not worry about saturating either the companion or the satellite spots. The separation of $1''.566 \pm 0''.006$ between the two bodies also conveniently locates the secondary near the edge of the field of view, far away from the halo light of the primary star. Future work on characterizing the photometric calibration uncertainty in polarimetry mode can be expended in other wavelengths. Our study here focuses on the data in H band since there are existing data we can use right away for this characterization work and H is the most commonly used filter in the GPI Exoplanet Survey. If new observations need to be taken for the calibration purpose, HD 8049 would again serve as an ideal system.

2.6 Acknowledgments

This research was supported in part by NASA cooperative agreements NNX15AD95G, NNX11AD21G, and NNX14AJ80G, NSF AST-113718, AST-0909188, AST-1411868, AST-1413718, and DE-AC52-07NA27344, and the U.S. Department of Energy by Lawrence Livermore National Laboratory under DE-AC52-07NA27344. Work by L.-W. Hung is supported by the National Science Foundation Graduate Research Fellowship number 2011116466 under Grant number DGE-1144087. This work is based on observations obtained at the Gemini Observatory, which is operated by the Association of Universities for Research in Astronomy, Inc., under a cooperative agreement with the NSF on behalf of the Gemini partnership: the National Science Foundation (United States), the National Research Council (Canada), CONICYT (Chile), the Australian Research Council (Australia), Ministerio da Ciencia, Tecnologia e Inovacao (Brazil), and Ministerio de Ciencia, Tecnologia e Innovacion Productiva (Argentina).

Bibliography

- Crepp, J. R., Johnson, J. A., Howard, A. W., et al. 2014, *ApJ*, 781, 29
- Currie, T., Lisse, C. M., Kuchner, M., et al. 2015, *ApJ*, 807, L7
- Currie, T., Burrows, A., Madhusudhan, N., et al. 2013, *ApJ*, 776, 15
- Cutri, R. M., Skrutskie, M. F., van Dyk, S., et al. 2003, *VizieR Online Data Catalog*, 2246
- De Rosa, R. J., Patience, J., Wilson, P. A., et al. 2014, *MNRAS*, 437, 1216
- Draper, Z. H., Marois, C., Wolff, S., et al. 2014, in *Proc. SPIE*, Vol. 9147, *Ground-based and Airborne Instrumentation for Astronomy V*, 91474Z
- Hung, L.-W., Fitzgerald, M. P., Chen, C. H., et al. 2015a, *ApJ*, 802, 138
- Hung, L.-W., Duchêne, G., Arriaga, P., et al. 2015b, *ApJ*, 815, L14
- Ingraham, P., Perrin, M. D., Sadakuni, N., et al. 2014, in *Proc. SPIE*, Vol. 9147, *Ground-based and Airborne Instrumentation for Astronomy V*, 91477O
- Jensen-Clem, R., Millar-Blanchaer, M., Mawet, D., et al. 2016, *ApJ*, 820, 111
- Lu, J. R., Ghez, A. M., Yelda, S., et al. 2010, in *Proc. SPIE*, Vol. 7736, *Adaptive Optics Systems II*, 77361I
- Macintosh, B., Graham, J. R., Ingraham, P., et al. 2014, *Proceedings of the National Academy of Science*, 111, 12661
- Macintosh, B., Graham, J. R., Barman, T., et al. 2015, *Science*, 350, 64
- Maire, J., Ingraham, P. J., De Rosa, R. J., et al. 2014, in *Proc. SPIE*, Vol. 9147, *Ground-based and Airborne Instrumentation for Astronomy V*, 914785
- Millar-Blanchaer, M. A., Graham, J. R., Pueyo, L., et al. 2015, *ApJ*, 811, 18

- Millar-Blanchaer, M. A., Perrin, M. D., Hung, L.-W., et al. 2016, in Proc. SPIE, Vol. 9908, Ground-based and Airborne Instrumentation for Astronomy VI, 990836
- Morzinski, K. M., Males, J. R., Skemer, A. J., et al. 2015, ApJ, 815, 108
- Perrin, M. D., Maire, J., Ingraham, P., et al. 2014, in Proc. SPIE, Vol. 9147, Ground-based and Airborne Instrumentation for Astronomy V, 91473J
- Perrin, M. D., Ingraham, P., Follette, K. B., et al. 2016, in Proc. SPIE, Vol. 9908, Ground-based and Airborne Instrumentation for Astronomy VI, 990837
- Poyneer, L. A., De Rosa, R. J., Macintosh, B., et al. 2014, in Proc. SPIE, Vol. 9148, Adaptive Optics Systems IV, 91480K
- Sivaramakrishnan, A., & Oppenheimer, B. R. 2006, ApJ, 647, 620
- Wang, J. J., Rajan, A., Graham, J. R., et al. 2014, in Proc. SPIE, Vol. 9147, Ground-based and Airborne Instrumentation for Astronomy V, 914755
- Zurlo, A., Vigan, A., Hagelberg, J., et al. 2013, A&A, 554, A21

Chapter 3

Imaging the 44 AU Kuiper Belt-analogue debris ring around HD 141569A with GPI polarimetry

A modified version of this chapter was submitted to the *Astronomical Journal*.

Authors: Juan Bruzzone, Stanimir Metchev, Gaspard Duchene, Maxwell Millar-Blanchaer, Ruobing Dong, Jason Wang, James R. Graham, Johan Mazoyer, Schuyler, Wolff, S. Ammons, Adam Schneider, Alexandra Greenbaum, Brenda Matthews, Pauline Arriaga, Vanessa Bailey, Travis Barman, Joanna Bulger, Jeffrey Chilcote, Tara Cotten, Robert De Rosa, Rene Doyon, Michael Fitzgerald, Katherine Follette, Benjamin Gerard, Stephen Goodsell, Pascale Hibon, Justin Hom, Li-Wei Hung, Patrick Ingraham, Paul Kalas, Quinn M. Konopacky, James Larkin, Bruce Macintosh, Jerome Maire, Franck Marchis, Christian Marois, Katie Morzinski, Eric Nielsen, Rebecca Oppenheimer, David Palmer, Rahul Patel, Jennifer Patience, Marshall Perrin, Lisa Poyneer, Laurent Pueyo, Abhijith Rajan, Julien Rameau, Fredrik Rantakyro, Dmitry Savransky, Anand Sivaramakrishnan, Inseok Song, Remi Soummer, Sandrine Thomas, J. Wallace, Kimberly Ward-Duong, and Sloane Wiktorowicz.

We present the first polarimetric detection of the inner disk component around the pre-main

sequence B9.5 star HD 141569A. Gemini Planet Imager H -band ($1.65\mu\text{m}$) polarimetric differential imaging reveals the highest signal-to-noise ratio detection of this ring yet attained and traces structure inwards to $0.''25$ (28 AU at a distance of 111 pc). The radial polarized intensity image shows the east side of the disk, peaking in intensity at $\sim 0.''40$ (44 AU) and extending out to $\sim 0.''9$ (100 AU). There is a spiral arm-like enhancement to the south, reminiscent of the known spiral structures on the outer rings of the disk. The location of the spiral arm is coincident with ^{12}CO J=3–2 emission detected by ALMA, and hints at a dynamically active inner circumstellar region. Our observations also show a portion of the middle dusty ring at ~ 220 AU known from previous observations of this system. We fit the polarized H -band emission with a continuum radiative transfer model. Our best-fit model favors an optically thin disk with a minimum dust grain size close to the blow-out size for this system: providing further evidence of on-going dust production in the inner reaches of the disk.

3.1 Introduction

Debris disks are established laboratories to study planet formation and evolution. Planetesimals and infant planets interact with the dusty disk, and create gaps, asymmetries, offsets and local enhancements through various dynamical mechanisms that help infer their presence (e.g., β Pictoris disk and planet, [Lagage & Pantin 1994](#), [Kalas & Jewitt 1995](#), [Lagrange et al. 2010](#)). Of special interest are those young disks (up to 40 Myr) transitioning between protoplanetary disks and debris disks that show a significant deficit in near-IR or mid-IR emission or with a detected cavity in scattered light (e.g., 49 Ceti, [Hughes et al. 2008](#), HD 21997, [Kóspál et al. 2013](#)). The study of this subset of transitional disks is attractive because of the implications for gas giant planet formation and gas-dust interaction models in nascent planetary systems.

The star HD 141569A ($V = 7.12$ mag, [Høg et al. 2000](#); $H = 6.86$ mag, [Cutri et al. 2003](#)) is a well-known transitional disk host. HD 141569A is a young 5 ± 3 Myr ([Weinberger et al., 2000](#)) B9.5V star ([Jaschek & Jaschek, 1992](#)) at a distance of 111 ± 5 pc ([Arenou et al., 2017](#))

with $L_{\text{IR}}/L_{\text{star}} \sim 8 \times 10^{-3}$ (Sylvester et al., 1996) and two low mass stellar companions, *B* and *C*, at roughly $9''$ (Weinberger et al., 2000). Early IRAS observations suggested an inner population of ~ 100 K circumstellar dust (Jaschek et al., 1986; Walker & Wolstencroft, 1988) at an estimated distance of 47–60 AU from the observed 12–100 μm excess.

The first high-contrast coronagraphic images in scattered light with HST/NICMOS at $\sim 1.6\mu\text{m}$ (F160W) revealed a bright dusty disk inclined at $53^\circ \pm 5^\circ$ and position angle (PA) of $355^\circ \pm 1^\circ$ (Augereau et al., 1999a; Weinberger et al., 1999). Weinberger et al. (1999) reported a disk extending out to $4''$ with two conspicuous nested rings peaking at $2''.0$ (220 AU) and $3''.3$ (360 AU; along the semi-major axis of the disk), separated by a $1''$ -wide gap devoid of scattering material. In this work, we refer to the 220 AU and 360 AU rings as the middle and outer rings, respectively. The brighter eastern side of the system is likely nearer to us under the assumption of preferentially forward scattering by dust (Weinberger et al., 1999). Subsequently, HST/STIS optical unfiltered coronagraphic observations (365–806 μm , 50CCD; Mouillet et al., 2001) and with the HST/Advanced Camera for Surveys (ACS), at 430 μm (F435W), at 590 μm (F606W) and 830 μm (F814W; Clampin et al., 2003) revealed asymmetries, and two prominent tightly wound spiral substructures: an inner arm between $1''.8$ – $2''.2$ (200 AU–240 AU) and an outer broad ring at $3''.0$ – $4''.0$ (330 AU–440 AU).

In a new analysis of archival Gemini/NICI and HST/NICMOS data, Mazoyer et al. (2016) report a split in two fine rings in the eastern part of the disk and show that the $2''$ ring shows a small $0''.03$ offset relative to the central star. High-contrast coronagraphic observations in the near-IR with VLT/SPHERE further revealed the presence of a third inner ring at ~ 44 AU (Perrot et al., 2016). This resolved inner disk component is also seen as an arc-like rim by Konishi et al. (2016) in optical broadband light with HST/STIS, and marginally detected by Currie et al. (2016) with Keck/NIRC2 at L_p . Mawet et al. (2017) confirm the detection of the inner disk around HD 141569A in L_p -band scattered light with a vortex coronagraph in Keck/NIRC2. Recent resolved 870 μm and 2.9 mm continuum ALMA observations (White et al., 2018) limit the presence of dust in this inner system out to about 55 AU.

We present the first *H*-band polarimetric observations of the 44 AU ring of HD 141569A (Section 3.2). We use polarimetric differential imaging (PDI) with the Gemini Planet Imager (GPI, [Macintosh et al., 2014](#)). PDI excels in high-contrast sensitivity to polarized circumstellar emission, as it eliminates the need of further PSF subtraction that can hamper the detection of extended emission. Our PDI observations reveal the ring at high SNR with the emission peaking at 44 AU and extending inwards to $0.''25$ (28 AU; Section 4.3). We model the linear polarized intensity image to derive the physical parameters of the disk (Section 4.4). We also compare the predicted thermal emission from our best-fit model against the SED from previous studies (Section 3.5). We present our conclusions in Section 3.6.

3.2 Observations

We observed HD 141569A on 2014 March 22 UT in polarimetry mode of *H* band during GPI commissioning at the Gemini South Telescope. We acquired 50 frames of 60 seconds each over 45° of parallactic field rotation at an average airmass of 1.12. Between each observation the half wave plate (HWP) modulator was rotated in 22.5° steps. The HWP introduces modulation in the signal and thereby allows for reconstruction of the Stokes vector later in the reduction steps. During these observations, the average Gemini Differential Image Motion Monitor (DIMM) seeing at Cerro Pachón was $0.''70$. We reduced the data with the GPI Data Reduction Pipeline (GPI DRP; [Maire et al., 2014](#); [Perrin et al., 2014](#)) following the procedure described in [Perrin et al. \(2015\)](#) and [Millar-Blanchaer et al. \(2015\)](#). This starts with dark subtraction, correction for instrument flexure, microphonics noise, and bad pixels. Each frame is then assembled into a polarization datacube where the third dimension represents the measured two orthogonal polarization states yielded by the Wollaston prism analyzer. The position of the obscured star is determined by a Radon transform-based algorithm ([Pueyo et al., 2015](#)). Each cube is then divided by a Gemini Facility Calibration Unit (GCAL) flat field, for throughput correction across the field. The next step involves a double differencing between the two polarization

states to correct for non-common path errors as described by Perrin et al. (2015). We correct for instrumental polarization systematics as outlined in Millar-Blanchaer et al. (2015).

The individual difference cubes are shifted to place the occulted star at the center of the frame and rotated to a common orientation: north along the y -axis and east along the x -axis. All cubes are then combined using a singular value decomposition matrix inversion based on waveplate angle and sky rotation for each exposure (Perrin et al., 2015). The procedure returns a Stokes datacube $[I, Q, U, V]$ that holds the total intensity, linear and circular polarization information for the entire observation sequence. Because GPI's HWP is not exactly one half wave at all wavelengths, GPI is only weakly sensitive to circular polarization, Stokes V . Thus we disregard the Stokes V cube slice. Afterwards, following Schmid et al. (2006), the Stokes cube was transformed into the radial Stokes convention $[I, Q_r, U_r, V]$. In this formalism, positive values of Stokes Q_r represent linear polarization perpendicular to the radial direction from the star, while negative values represent polarization parallel to the radial direction. For Rayleigh-like scatterers in an optically thin debris disk, no flux is expected in the Stokes U_r image as only the perpendicular macroscopic polarization state (azimuthal polarization) prevails (Millar-Blanchaer et al., 2015). Thus, light from single scattering events by dust grains will lead to positive values in Stokes Q_r . However, we note that multiple scattering in optically thick disks could have a Stokes U_r signal of a few percent of the Stokes Q_r signal that is below the sensitivity of the observations (Canovas et al., 2015).

In the final reduction step, we flux-calibrated the data. Following the procedure outlined in Hung et al. (2016), we adopt 1.85 ± 0.07 Jy as the H -band flux of HD 141569A from 2MASS (Cutri et al., 2003) to obtain a conversion factor of $(1.05 \pm 0.06) \times 10^{-8}$ Jy ADU⁻¹ coadd⁻¹. Complementary to the Stokes Q_r image, we also reduced the total intensity image (Stokes I slice) for the entire sequence with pyKLIP (Wang et al., 2015) which implements the Karhunen-Loève Image Projection algorithm (KLIP, Soummer et al., 2012) for optimal PSF subtraction.

Immediately after the polarimetry sequence was completed we also acquired integral field

spectroscopic (IFS; non-polarimetric) observations of HD 141569A with GPI in the H band. The IFS data contain an independent measurement of the total intensity flux from the disk. The sequence comprised 32 frames of 60 seconds each. The sequence started at an airmass of 1.13, with an average Gemini DIMM seeing of $1''.01$ and 27° of cumulative field rotation. We reduced the data and assembled the spectral datacubes with the standard recipes provided in the GPI DRP. The entire reduced dataset was then processed with pyKLIP.

3.3 Results

We present the imaging results in polarized and total intensity in Section 3.3.1 and 3.3.2, respectively. We revisit these further in Sections 3.5.1-3.5.2 in the context of previous observations and a scattered-light model of the disk (Section 4.4).

3.3.1 Polarized Intensity H-band Image

The H -band Stokes Q_r image in Figure 3.1 shows the first polarized light detection of the HD 141569A inner disk. We clearly resolve the eastern portion of the disk: likely the result of predominantly forward scattering by micron-size dust grains. This is dictated by the combined effects of phase function and polarization dependence with scattering angle. Most known dust compositions preferentially scatter light in the forward direction for dust particles a few times larger than the wavelength of the scattered light (van de Hulst, 1957). For such particles, optically-thin Mie models also suggest that polarized intensity curves peak at scattering angles $\leq 90^\circ$ (Perrin et al., 2015).

The emission peaks at a semi-major axis of $0''.40$ (44 AU) and extends out to $\sim 0''.9$ (100 AU), where it blends into the background. At $1''$ to the east the Stokes Q_r surface brightness increases again revealing the previously detected middle dusty ring at 220 AU. The clearing between the inner disk and the middle ring indicates a region deficient in scattering material, assuming that the disk is optically thin. In Section 3.5.2 we further discuss a residual arc-

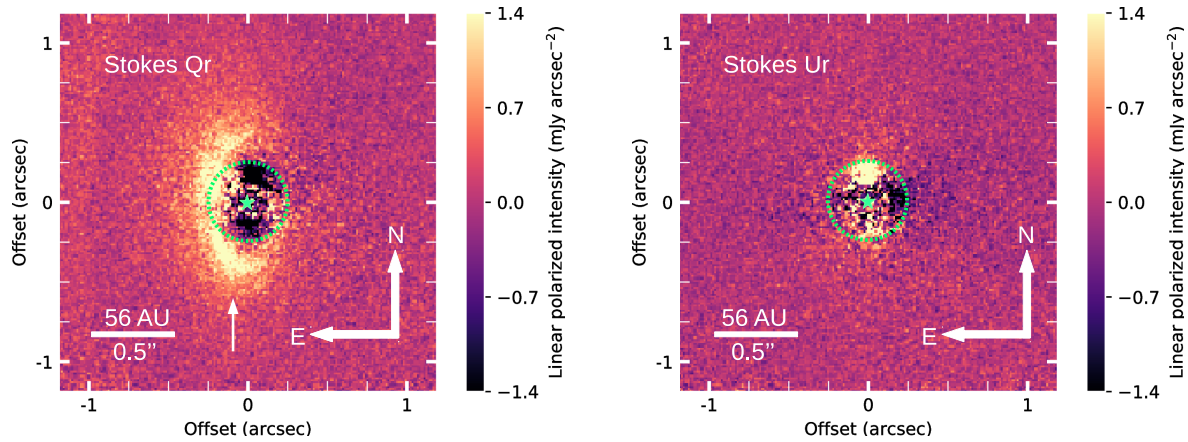


Figure 3.1 Observations of the HD 141569A dusty disk in H -band linear polarization with GPI in a total of 50 minutes of integration. *Left*: Linear polarization intensity Q_r image. *Right*: Stokes U_r image shown on the same color scale. An arrow points to the location of the surface brightness enhancement – an arc feature (see Figure 3.8) – to the south. A star symbol marks the position of the star, and a circular aperture of radius $0\prime.25$ centered on the star indicates the region affected by uncorrected instrumental polarization. Beyond this region, the U_r image scatters uniformly around zero flux, which indicates that the dust seen in the Stokes Q_r is optically thin. The previously known middle ring is visible at low surface brightness at $\sim 1''$ to the east in the Stokes Q_r image.

like structure to the south, which is also detectable as a brightness enhancement in the Stokes Q_r image (Figure 3.1, left panel). Uncorrected instrumental polarization and other reduction artifacts affect the signal within $0\prime.25$. We delimit this central circular region in subsequent figures, and exclude it from our analysis.

No coherent structures are observed in the Stokes U_r image to indicate significant optical depth. Hence, the Stokes U_r image can be used as a noise map for our measurements and it reassures the astrophysical nature of the Stokes Q_r emission: specifically the polarized morphology exterior to $0\prime.25$ and the middle ring near the edge to the east. Figure 3.2 shows an SNR map created by dividing the Q_r image at every position by local noise estimated as the standard deviation of pixels within a 3 pixel-wide annulus in the Stokes U_r image at the same angular separation from the star.

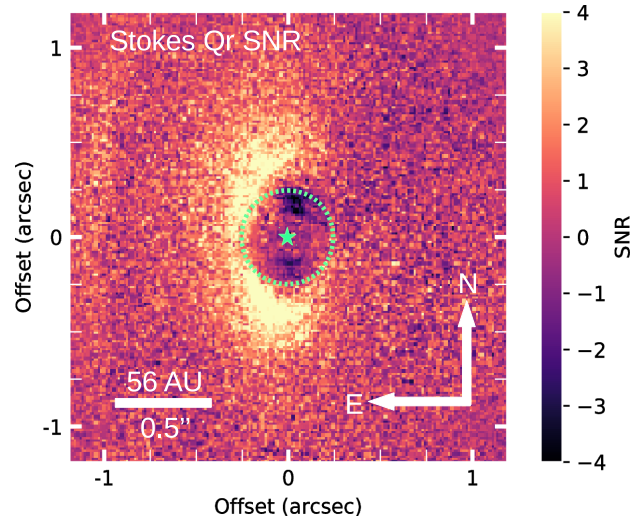


Figure 3.2 H -band Stokes Q_r SNR map of HD 141569A. Each point on the map is constructed by dividing the Q_r image by the standard deviation of all pixels within a 3 pixel-wide annulus in the U_r image at the same angular separation from the star.

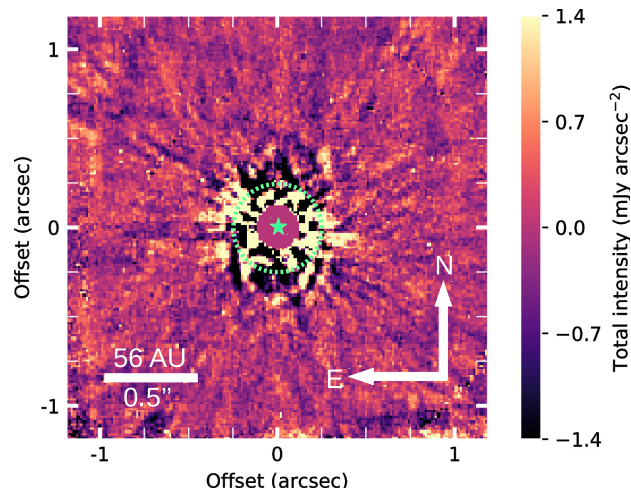


Figure 3.3 H -band total intensity (Stokes I) pyKLIP+ADI reduction of HD 141569A (Section 3.3.2). Self-subtraction degrades the residuals, and there is no significant evidence of the presence of the inner ring. The image hints at the presence of the middle 220 AU ring 1'' to the east.

3.3.2 Total Intensity H-band Image

We attempted to detect the total intensity emission from the inner ring in two different ways: from the combined polarization states in our PDI observations, and from the unpolarized IFS observations. Figure 3.3 shows the result of the PSF subtraction of the Stokes I image after applying pyKLIP Wang et al. (2015) and Angular Differential Imaging (ADI, Marois et al.,

2006). Our shorter IFS sequence with GPI did not reveal neither the inner disk detected in Stokes Q_r nor the previously known middle ring.

Our inability to detect the inner ring in total intensity is not entirely surprising. In extracting the Stokes I signal from high-contrast observations we lose the differential imaging advantage of PDI. Moreover, the PSF subtraction process in total intensity also removes the smooth structure of the disk. Hence, we expect greater sensitivity to scattered light in our polarized light Stokes Q_r image. In view of the low-SNR detection in total intensity we use only the polarimetric detection in Stokes Q_r in the remainder of this study.

3.4 Disk Modeling

We model the resolved polarized Stokes Q_r image of the inner disk with a radiative transfer model to determine the disk geometry (Section 3.4.1) and dust properties (Section 4.4.2). The same modeling tool can predict the SED for the disk models, but since the SED is dominated by emission from dust outside the GPI field of view, we only compute model SED as a test to check against gross inconsistency (Section 3.4.3).

3.4.1 Parameterization of the Dust Model

We use the Monte-Carlo continuum radiative transfer and ray-tracing code MCFOST (Pinte et al., 2006, 2009) to compute synthetic observations of the SED and the Stokes Q_r images of the disk around HD 141569A. MCFOST computes the scattering, absorption and re-emission events by dust grains by propagating photon packets throughout a cylindrical spatial grid in accordance with Mie theory. Dust grains are assumed to be in radiative equilibrium embedded in the radiation field from the host star. The sampling of our synthetic images is defined to cover the entire field of view of observations using GPI's pixel scale of GPI of 14.166 ± 0.007 mas lenslet⁻¹ (De Rosa et al., 2015). The star is located at the center of the computational grid and the disk is centered on the star. To obtain the stellar luminosity, we fit the optical to near-IR

Fixed stellar parameters		
Distance	$d(pc)$	111
Stellar Radius	$R_*(R_\odot)$	1.66 R_\odot
Effective Temperature	$T_{\text{eff}}(K)$	10000
Extinction	E_{B-V}	0.144
	R_V	3.1
Disk model fixed parameters		
Inner Radius	$R_{in}(AU)$	20
Outer Radius	$R_{out}(AU)$	110
Inner exponent	α_{in}	14
Reference Radius	$R_0(AU)$	45
Solid material dust density	$\rho_{\text{dust}} (\text{g cm}^{-3})$	3.5
Flaring exponent	β	1
Vertical exponent	γ	1

Disk model free parameters		Sampling	Range	Number of values	Best Fit Value
Inclination	$i(^{\circ})$	lin. in cosine	[40, 80]	10	$60^{\circ} \pm 10^{\circ}$
Position Angle	$PA(^{\circ})$	lin.	[-25, 15]	9	$5^{\circ} \pm 10^{\circ}$
Reference Scale Height	$H_0 (AU)$	lin.	[2.2, 36]	9	14_{-5}^{+9}
Dust mass	$M_d (M_\odot)$	lin.	$[0.2, 2.0] \times 10^{-6}$	10	$1.0 \pm 0.4 \times 10^{-6}$
Outer exponent	α_{out}	lin.	[-3.5, 0.0]	8	$-1.0_{-1.0}^{+0.5}$
R_c	$R_c (AU)$	lin.	[24, 64]	11	44_{-12}^{+8}
Minimum grain size	$a_{min} (\mu\text{m})$	log.	[0.5, 16]	6	4_{-2}^{+4}
Porosity	$p (\%)$		[0, 20, 40, 60, 80]	5	0
Minimum reduced χ^2					0.93

Table 3.1: Parameters probed in our exploration grid of models with MCFOST and best-fit values for the Stokes Q_r image.

SED of HD 141569A (Høg et al., 2000; Mendigutía et al., 2012; Cutri et al., 2003), keeping the stellar radius and foreground extinction as variables. We assumed a fixed distance of 111 pc (Arenou et al., 2017) with an effective temperature of 10000 K for the star (Merín et al., 2004) and used NextGen photospheric models from Hauschildt et al. (1999).

The disk geometry in cylindrical coordinates is described by the radial extent of the disk, with inner and outer radii R_{in} and R_{out} , inclination i , position angle PA and dust density distribution $\rho(r, z) = \Sigma(r)Z(r, z)$. Following Augereau et al. (1999b), the dust distribution in the vertical direction is parameterized within the MCFOST framework as an exponential with a shape parameter γ :

$$Z(r, z) = \exp\left(-\frac{|z|}{H(r)}\right)^\gamma, \quad (3.1)$$

where the scale height is defined as $H(r) = H_0 \left(\frac{r}{R_0}\right)^\beta$ at a fixed reference radius $R_0=45$ AU, and β is a disk flaring parameter. Radially, the dust distribution follows a smooth combination of two power laws:

$$\Sigma(r) \propto \left\{ \left(\frac{r}{R_c}\right)^{-2\alpha_{in}} + \left(\frac{r}{R_c}\right)^{-2\alpha_{out}} \right\}^{-1/2}, \quad (3.2)$$

where $\alpha_{in} > 0$, $\alpha_{out} < 0$, and R_c is the radial distance of the peak density of the grain distribution. The surface density of dust grains is represented as:

$$\sigma(r) = \int_{-\infty}^{+\infty} \rho(r, z) dz = \sigma_0 \times \Sigma(r) \left(\frac{r}{R_0}\right)^\beta, \quad (3.3)$$

where $\sigma_0 = 2H_0\rho(R_0, 0)$ for $\gamma = 1$. The maximum of the surface density is not at R_c , but at

$$r_{\max(\sigma)} = \left(\frac{\Gamma_{in}}{-\Gamma_{out}}\right)^{(2\Gamma_{in}-2\Gamma_{out})^{-1}} R_c, \quad (3.4)$$

where $\Gamma_1 = \alpha_{in} + \beta$ and $\Gamma_2 = \alpha_{out} + \beta$, which in our case is nearly identical to R_c .

We assume a disk with a constant opening angle, thus no flaring ($\beta = 1$), and adopt $\gamma=1$. Without better initial constrains on these parameters our assumption is reasonable for an optically-thin debris disk.

To characterize the dust content in the disk, we adopt a power-law grain size distribution $dN(a) \propto a^{-n} da$ with $n = 3.5$ as is commonly assumed for debris disks in a steady-state collisional cascade (Dohnanyi, 1969). The value of n is steeper than recent estimates from archival ALMA observations of HD 141569A by White et al. (2018). Authors estimate $n = 2.95 \pm 0.1$ for a 16–45 AU inner disk and $n = 3.21^{+0.30}_{-0.16}$ for a 90–300 AU disk. We discuss the exponent of the grain size distribution further in Sec 3.5.4. The size distribution has limits a_{\min} and a_{\max} and grain porosity p . We fix $a_{\max} = 1$ mm and leave a_{\min} as a free parameter in the model. Modeling is limited to a stellocentric disk populated by a single dust grain composition of amorphous magnesium-rich olivine with a dust grain density $\rho_{\text{dust}} = 3.5 \text{ g cm}^{-3}$. We adopted this dust grain composition to match the composition used by Thi et al. (2014) and Mawet et al. (2017).

Our disk model parametrization thus comprises: R_{in} , R_{out} , i , PA , H_0 , M_d , α_{in} , α_{out} , R_c , a_{\min} and p . To reduce the burden of an 11 dimensional parameter exploration, we fixed R_{in} and R_{out} at 20 AU and 110 AU respectively. These disk boundaries are motivated by our inability to detect the inner disk within $\sim 0''.25$ and beyond $1''$ from the star (Figure 3.2). We also set $\alpha_{in} = 14$ as motivated by preliminary modeling that pointed to high α_{in} values. Such a steep profile implies a sharp drop in density inside of r_{\max} . The probability density distribution for α_{in} in those models plateaued at $\alpha_{in} \geq 14$.

By exploring each of the variable parameters at 5 to 11 discrete values, we construct a model grid with over 3×10^7 grid points for the remaining eight free parameters. Table 3.1 details the full set of parameters involved in the modeling, including additional fixed parameters for the star and disk.

3.4.2 Polarized Scattered Light Modeling and Best Fit Estimates

In preparation for the fitting procedure, we first binned the images in 3×3 pixels to reduce the effects of correlated errors. GPI’s resolution element is about 3 pixels in the H band, and therefore, the binning should not lead to loss of spatial information. Following Millar-Blanchaer et al. (2015), we used the 3×3 binned Stokes U_r to derive the uncertainties used to

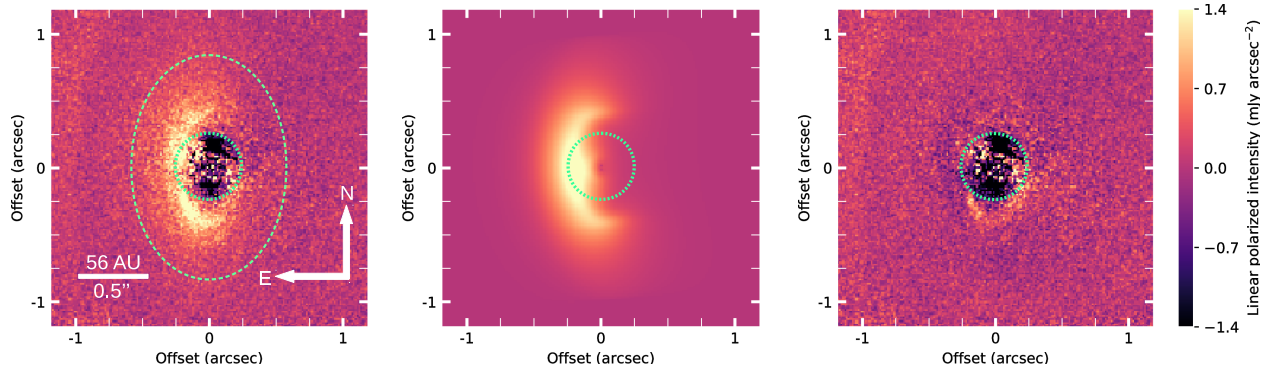


Figure 3.4 Modeling of the inner HD 141569A dust ring with MCFOST. The central $0''.25$ circular region is the same as in Figures 3.1–3.3, and is ignored in the modeling. *Left*: Observed Stokes Q_r image with the fitting region delimited between the circular and elliptical dashed lines. *Center*: Stokes Q_r image from best-fit model. *Right*: Residuals of the Stokes Q_r image minus the best-fit model. A residual arc-like polarized emission is seen to the south. We have used the same intensity scale and color stretch as for the Stokes U_r image in Figure 3.1.

fit the binned Stokes Q_r image. For each position in the binned Stokes Q_r image, the uncertainty is calculated as the standard deviation of a 3 pixel-wide annulus on the binned U_r image. These steps return the uncertainty map σ to use in the χ^2 minimization procedure:

$$\chi^2 = \sum_i^{N_{pix}} \left(\frac{Obs_i - Mod_i}{\sigma_i} \right)^2. \quad (3.5)$$

The fitting occurs within an $0''.85 \times 0''.61$ (radius) elliptical region centered on the star and excludes the central $0''.25$ -radius circular region to avoid PSF subtraction residuals (Figure 3.4, left). The fitting region in the binned image has 767 resolution elements. We opt for an elliptical fitting region rather than a circular one because Poisson noise from the disk rather than the stellar halo is the main limiting factor for our sensitivity. Unlike Mawet et al. (2017), we do not use a free parameter to scale the flux of the models to the flux of the Stokes Q_r image. Instead we aim to reproduce the properly calibrated fluxes as observed.

The outcome of our modeling strategy is presented in Figure 3.4 which shows the Stokes Q_r image (left), the best-fit model (center), and the residuals (right): all displayed on the same color and intensity scale as the Stokes U_r image in Figure 3.1. Our best-fit model returns a reduced $\chi_r^2 = 0.93$ and so provides a good match to the Stokes Q_r image. Our best-fit model

Stokes U_r image contains virtually no flux, on the order of 0.1% of the model Stokes Q_r . This indicates that the disk is optically thin with an inferred mid-plane optical depth of $\tau_{1.65\mu\text{m}} = 10^{-2}$ from MCFOST.

As a consistency check on our best-fit solution, we plot radial profiles of the polarized emission along the semi-major axis of the disk, and compare them to the prediction from the model (Figure 3.5). We see that the model follows the radial profile well, and stays within the $1\text{-}\sigma$ uncertainty band at most separations, except inwards of 31 AU to the north, where it overestimates the observed emission. There is also residual emission to the south around $PA = 150^\circ$ that has no counterpart to the north (Figure 3.4, right), which we discuss in Section 3.5.1 and 3.5.2.

The overall consistency of the model and image radial profiles give us confidence that we have an adequate understanding of the dust disk parameters. Assuming that our observational errors are approximately Gaussian, and adopting a flat prior for each parameter, the Bayesian probability of our model given the data is:

$$P \propto \exp\left(-\frac{\chi^2}{2}\right). \quad (3.6)$$

To estimate the probability density distribution for any parameter, we marginalize P over the remaining parameters as shown in Figure 3.6.

We obtain good constraints for α_{out} , M and a_{min} , whose probability density distributions are approximately Gaussian. Unfortunately, our modeling returns poor constraints on the viewing geometry of the disk and on some of the parameters that describe the spatial distribution of the dust. The posterior distributions for i and PA in Figure 3.6 are broader than we anticipated. Hence, we cannot establish a proper uncertainty. This suggests that polarized intensity is not the right approach for setting the geometry, since only the Eastern half of the disk is detected. In addition, for H_0 and R_c our modeling returns non-symmetric skewed distributions. We use the 68% confidence intervals as estimates for the uncertainties on the best-fit parameter values

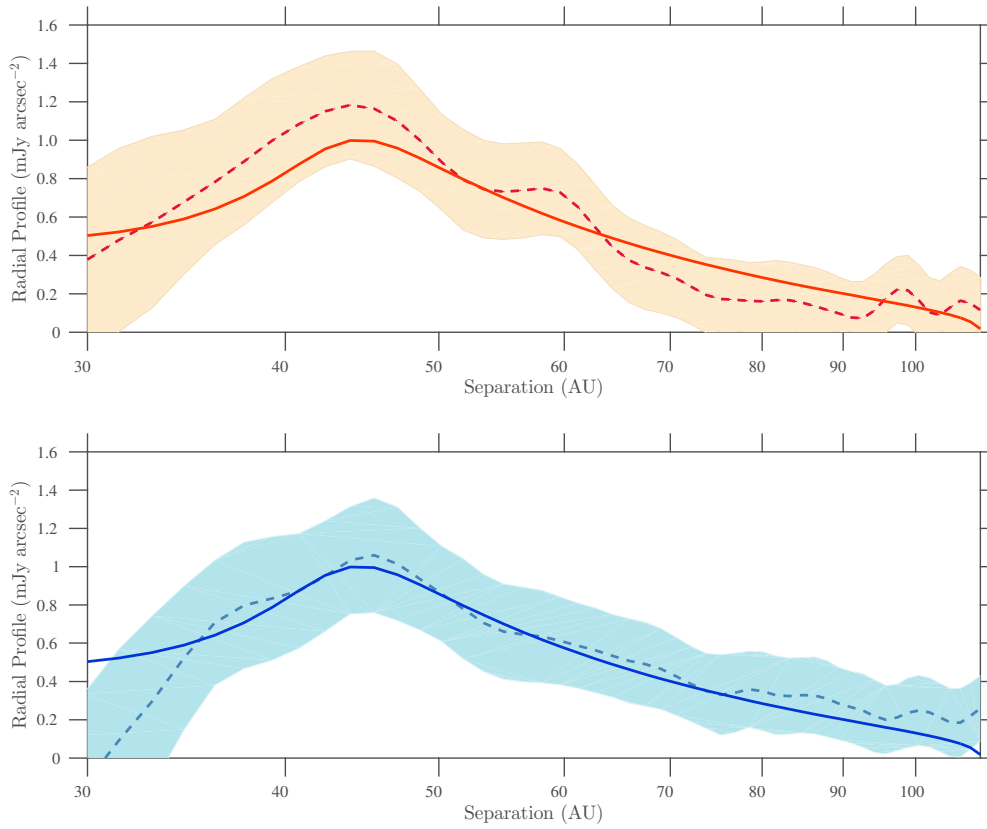


Figure 3.5 Radial profiles along the semi-major axis ($PA = 5^\circ$) of the Stokes Q_r image (dashed line) and of the best-fit models with MCFOST (solid line) inwards to 30 AU ($0'27$): *north* (top) and *south* (bottom). Shaded areas indicate the dispersion calculated using the uncertainty map derived from the Stokes U_r image (Figure 3.1, right panel). The best-fit model falls within uncertainties and in general agrees with the observed profiles.

for i , PA , H_0 , α_{out} , R_c and M_d . For a_{min} and p , we use the 90% confidence interval instead, as motivated by our coarser sampling in these parameters.

Our best-fit disk model has $i \sim 60^\circ$, position angle $PA \sim 5^\circ$, scale radius $R_c = 44^{+8}_{-12}$ AU, a rather large reference scale height $H_0 = 14^{+9}_{-5}$ AU (which at a reference radius of $R_0 = 45$ AU gives an opening angle of 17°), and a shallow outer exponent $\alpha_{\text{out}} = -1.0^{+0.5}_{-1.0}$. The total dust mass of $1.0 \pm 0.4 \times 10^{-6} M_\odot$ is within the range $0.03\text{--}1 \times 10^{-5} M_\odot$ estimated from SED modeling (Zuckerman et al., 1995; Sylvester et al., 1996; Merín et al., 2004; Thi et al., 2014). The best-fit minimum grain size is $a_{\text{min}} = 4^{+4}_{-2} \mu\text{m}$ (90% confidence interval). The minimum grain size

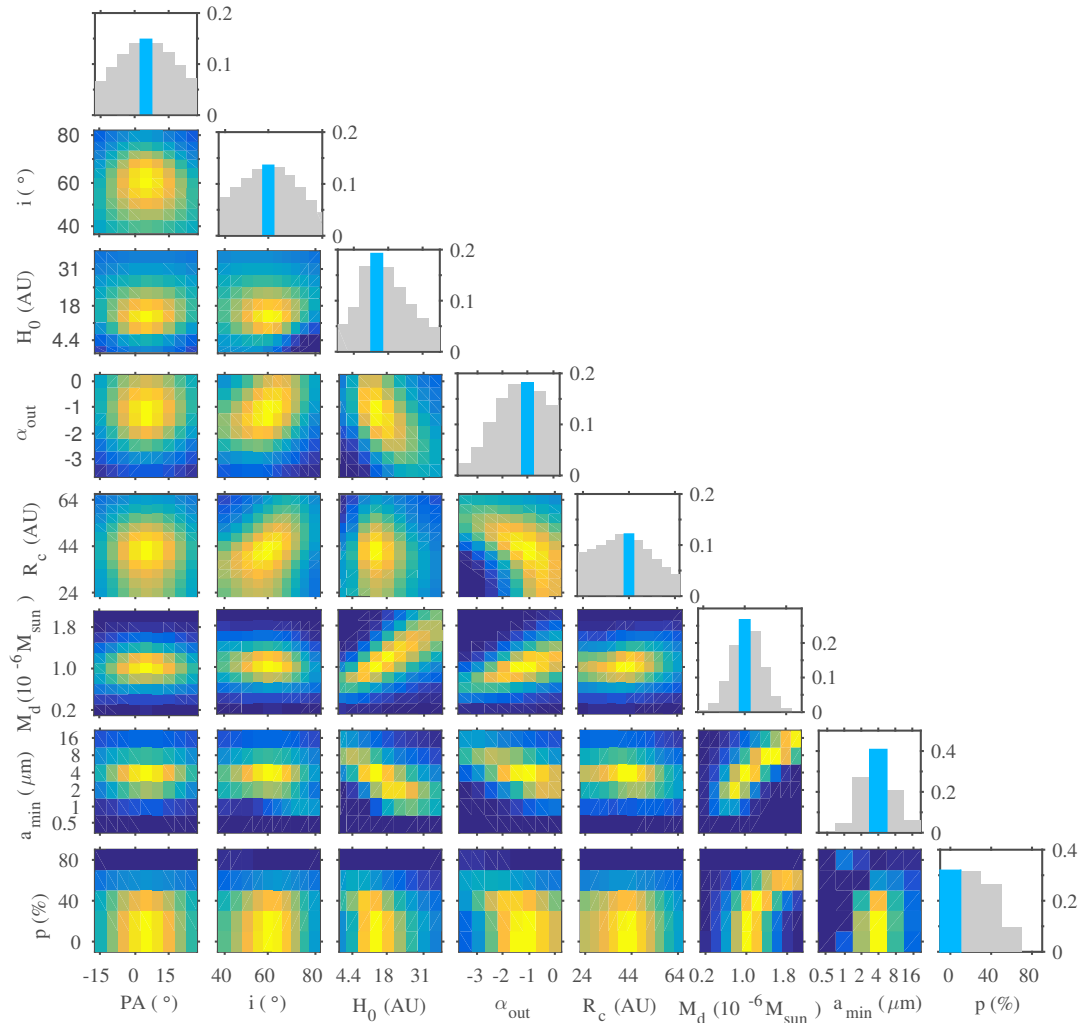


Figure 3.6 Normalized probability density distributions for each parameter in the grid of models explored to fit the Stokes Q_r image with MCFOST. Brighter yellow regions in the color maps correspond to higher probability densities. A blue bar in each of the histogram panels along the diagonal shows the best-fit value for each parameter.

agrees with the blow-out grain radius (Burns et al., 1979) for this system, with $r_{\text{blow-out}} = 4.2 \mu\text{m}$ for spherical silicate grains of density $\rho = 3.5 \text{ g cm}^{-3}$, assuming a radiation pressure efficiency

factor of $Q_p = 1$. The best-fit model favors a population of solid dust grains, porosity $p = 0\%$, although it is consistent with porosity up to $p = 40\%$ within the 90% confidence limit.

As seen in Figure 3.6, the total dust mass M_d is strongly degenerate with several disk parameters, notably the minimum grain size a_{\min} , the outer exponent α_{out} and, surprisingly, the disk scale height H_0 . There is no evident mechanism by which the scale height would be degenerate with the disk mass for an optically thin disk. A third parameter could set this correlation but the relationship remains unclear. All of these degeneracies preclude us from placing fully independent constraints on M_d , a_{\min} , H_0 , or α_{out} . In Section 3.5.4 we discuss an independent and more stringent constraint on the minimum grain size a_{\min} , arising from the lack of measurable signal in the Stokes U_r image.

3.4.3 Comparison of the Scattered Light Model to the SED

We compare the predicted thermal emission from our best-fit model to the Stokes Q_r image against the SED of HD 141569A in Figure 3.7. Fitting the SED is not a part of our search for the model that best matches the scattered light emission. It is merely a consistency check on our scattered light modeling assuming that the same dust population is responsible for both disk tracers.

We use the compendium of photometric data from Thi et al. (2014) with updated photometry in the optical (Høg et al., 2000; Mendigutía et al., 2012). We expand this dataset by including recent sub-millimeter and millimeter photometry with ALMA (White et al., 2018) and with the Submillimeter Array (SMA; Flaherty et al., 2016). We note that the photometric measurements in Thi et al. (2014), Flaherty et al. (2016) and White et al. (2018) come from instruments with different resolutions and beam sizes. These include FWHM $\approx 1''$ seeing-limited optical/near-IR measurements, and range from $0''.69 \times 0''.52$ for the 2.9 mm ALMA photometry to $5''.1 \times 4''.2$ for the 2.8 mm SMA photometry, and up to $12''$ for $22\mu\text{m}$ photometry from the Wide-field Infrared Survey Explorer (WISE).

We also include a PAH component, motivated by resolved (FWHM = $0''.26$) observations

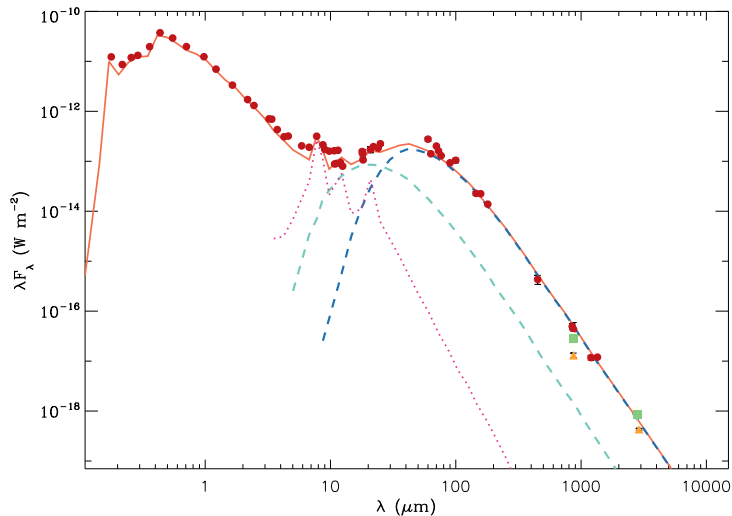


Figure 3.7 Measured data points and predicted MCFOST SEDs. Observations comprise the photometric compendium by Thi et al. (2014) and references therein (filled circles), SMA photometry by Flaherty et al. (2016, filled squares), and ALMA photometry by White et al. (2018, filled triangles). The model SEDs represent: the best-fit model to the Stokes Q_r image of the HD 141569A inner disk (dark blue dashed line), a fourth innermost disk (light blue dashed line), and PAH emission (magenta dotted line). The total emission from these components and the star is shown with a solid line.

with the VLT Imager and Spectrometer for the mid-IR (VISIR, Lagage et al. (2004)) in the PAH1 filter ($\lambda_c = 8.6\mu\text{m}$, $\Delta\lambda = 0.42$). These reveal a disk out to $1''$ along the semi-major axis (Thi et al., 2014). PAHs in the circumstellar environment of HD 141569A are responsible for the emission features in the mid-IR at 7.7 , 8.7 , 11.3 and $12.7\mu\text{m}$ (Sylvester et al., 1996). We include the PAH component (magenta dotted line) with the sole goal of approximating the emission features in the mid-IR modeled in previous studies (Li & Lunine, 2003; Thi et al., 2014). PAHs were added with the adopted single molecule size of 6.84 \AA and fixed mass of $1.6 \times 10^{-10} M_\odot$ from Thi et al. (2014).

Finally, we note that even while it reproduces the observed $\geq 50\mu\text{m}$ fluxes adequately, the combined SED of our scattered light and PAH emission model is underluminous between 8 – $30\mu\text{m}$. A fourth component, interior to the one seen by GPI, is likely present around the star. To correct for this flux deficit in the mid-IR, we model an innermost 5 – 15 AU dust disk (light

blue dashed line in Figure 3.7) in MCFOST. We discuss this innermost disk further in Section 3.5.5.

The combined thermal emission from our model of the polarized scattered light, the PAH grains, and the unseen fourth innermost ring reproduces the observed thermal excess seemingly well (Figure 3.7). It is broadly consistent with the mid-IR to mm data, especially given the large scatter among the millimeter fluxes.

However, the above combination of circumstellar dust components does not include the previously known middle or the outer HD 141569A rings. Therefore, our predicted mid- to far-IR flux is only a lower limit on the total thermal emission from all circumstellar components. In particular, the 220 AU middle ring would be expected to have a temperature of ~ 45 K, and so contributing significantly to the far-IR emission.

The discrepancy with our model likely reflects the different dust populations detected with GPI vs. mm observations. Even if our assumed dust size distribution extends to 1 mm, our Stokes Q_r image is sensitive to micron-sized dust, while SMA, ALMA, and JCMT observations trace mm-sized grains. The complex multi-ringed disk environment around HD 141569A requires a comprehensive modeling of scattered-light images and thermal emission maps that is beyond the scope of this paper.

3.5 Discussion

3.5.1 Morphology of the HD 141569A Inner Disk in Polarized Scattered Light: Comparison to Previous Observations

PDI with GPI has revealed the clearest view of the inner disk around HD 141569A inwards to an inner working angle (IWA) of $0''.25$ (28 AU). The IWA achieved with GPI shows the 44 AU ring morphology that supersedes any lower-SNR detections from images with larger IWAs.

The highest SNR obtained on the 44 AU ring previously in scattered light is through L_p -band AO and vortex coronagraphy with Keck/NIRC2 (FWHM $\approx 0''.08$, effective IWA $\approx 0''.16$)

by [Mawet et al. \(2017\)](#), and also reported with Keck/NIRC2 in L_p -band by [Currie et al. \(2016\)](#) down to 0."25. [Perrot et al. \(2016\)](#) report even higher angular resolution H -band AO observations with VLT/SPHERE (FWHM $\approx 0.''040$, IWA=0."093), as do [Konishi et al. \(2016\)](#) with HST/STIS (FWHM=0.'04, IWA=0.'40). Compared to our PDI with GPI, all of these previous non-polarimetric observations have lower SNR because of the inability to employ simultaneous differential imaging through polarimetry, but relying solely on ADI instead. Diffuse structures with significant axial symmetry, such as debris disks seen at low to moderate inclinations, are challenging to extract with ADI/KLIP. PDI with GPI has produced a high-SNR detection of the disk with much lower reduction-dependent systematics.

Our GPI polarized light image confirms the clearing within the 44 AU ring first reported by [Perrot et al. \(2016\)](#). [Thi et al. \(2014\)](#), [Konishi et al. \(2016\)](#) and [Mawet et al. \(2017\)](#) report PAH emission or scattered light emission from dust at similar separations, but describe its radial dependence with a single-exponent power law that decreases with separation. As seen in [Figure 3.5](#), we clearly resolve the peak at 44 AU that is well modeled with exponential drop-offs on either side. The width of the ring in polarized light (FWHM ~ 30 AU) is greater than reported (FWHM ~ 10 AU) from the unpolarized VLT/SPHERE observation of [Perrot et al. \(2016\)](#), which we attribute to self-subtraction in the various KLIP reductions of the SPHERE images.

Consistent with [Perrot et al. \(2016\)](#) and [Mawet et al. \(2017\)](#), we find a north-south asymmetry in the brightness of the 44 AU ring, which we now reveal as a high-SNR arc-like structure to the south. We do not see evidence of the other clumps reported in these studies, and suspect they may be related to image artifacts.

The viewing geometry of our best-fit model, $i \sim 60^\circ$ and $PA \sim 5^\circ$, is similar to previous findings from scattered light total intensity observations at lower SNR. [Perrot et al. \(2016\)](#) report that the inner ring has an inclination of $i = 57.9^\circ \pm 1.3^\circ$ and a PA of $353.7^\circ \pm 1.1^\circ$ from observations with VLT/SPHERE, while [Mawet et al. \(2017\)](#) report $i = 53 \pm 6^\circ$ and $PA = 349 \pm 8^\circ$ from L_p observations with Keck/NIRC2.

However, unlike all previous direct imaging (non-polarimetric) observations, which point to a relatively well-constrained slightly W of due N orientation of the semi-major axis of the inner ring, our polarimetric observation produces a less well constrained, slightly E of due N PA. Our values for i and PA follow broad distributions in Figure 3.6 that suggest uncertainties of about 10° . Our own H -band total intensity image (Figure 3.3) suggests a slightly clockwise ($PA \sim 350^\circ$) orientation of the scattered light emission: in agreement with Perrot et al. (2016) and Mawet et al. (2017), and contrary to our polarized image. Effectively, the orientation of the inner disk from previous total intensity observations is in perfect alignment with the outer disk.

It is at first surprising that our high-SNR polarimetric image does not produce better constraints. We note that the SNR of all of our and previously published total intensity observations is much lower, and that they suffer from the typical PSF-subtraction systematics for extended emission around bright stars: the result of ADI mode observations and image reduction with the KLIP algorithm. Thus, it is possible that the uncertainties in Perrot et al. (2016) have been underestimated, and our values are closer to agreement with theirs because of larger errors (as in Mawet et al., 2017). Nonetheless, the discrepancy between the polarized and the total intensity geometry is still unusual, as is the inability to get better geometric constraints from our polarized intensity images. We suspect that the failure of our modeling to produce better viewing geometry constraints may be a consequence of detecting only half of a radially extended disk in polarized intensity. The detection of this non-axisymmetric half disk, combined with the broader arc-like feature to the south (§ 4.4.2, Figure 3.4, right), may favor models with PAs flipped around the north-south axis.

3.5.2 The Arc-like Structure: Spiral Arm?

The arc-like asymmetry spans between $122^\circ - 170^\circ$ in PA. This feature is not an outcome of the data reduction process because the PDI image requires no PSF subtraction process, but is rather a true brightness enhancement in the ring. A disk with a stellocentric offset could be

another possible explanation for the enhanced emission from the arc-like structure to the south. The portion of the disk closer to the star would appear brighter than the other side, leading to pericenter glow (Wyatt et al., 1999). Our modeling procedure did not include stellocentric offsets, and so we cannot check for pericenter glow. Perrot et al. (2016) find that the inner ring has a stellocentric offset of 15.4 ± 3.4 mas (1.7 ± 0.4 AU) to the west, but only a negligible one, 1.2 ± 9.4 mas (0.1 ± 1.1 AU), to the north. Therefore a north-south stellocentric offset is not the likely cause of the brightness enhancement to the south.

For a clearer view of the morphology of the asymmetry, we mirror and subtract the northern portion of the disk from the southern half. Given the ambiguity of the disk’s orientation, we perform two different subtractions. In the first case we mirror around the semi-minor axis of the best-fit model of the polarized emission seen with GPI; i.e., the *PA* of the semi-major axis is 5° (Figure 3.8, middle panel). In the second case we use the geometry inferred from the total intensity image from SPHERE, with semi-major axis *PA* of 353.7° (Figure 3.8, right panel). Both subtractions show the excess emission to the south as a remnant arc. The residuals in the $PA = 5^\circ$ case are closer to zero, which is why our modeling of the polarized light emission prefers that geometry. However, the residuals in the $PA = 353.7^\circ$ case are more uniform, even if also more positive. Without a higher-SNR total intensity image of the disk, we can not decide in favor of one disk *PA* vs. the other. However, both point to the existence of an arc on the inner ring of the HD 141569A disk. Such arc-like structures are known on the outer two rings of HD 141569A (Mouillet et al., 2001; Clampin et al., 2003; Perrot et al., 2016; Mawet et al., 2017). We believe this to be the first convincing detection of such an arc on the inner ring. Still, we note that the location and extent of the feature match the observed brightness enhancement in the SE section of the inner ring in Perrot et al. (2016) and the enhancement in the CO zeroth moment map in White et al. (2016). Our best-fit model indicates an average temperature of ~ 90 K at the location of the arc, well above the sublimation point of CO. The CO production mechanism may thus be linked to the dust over-density: pointing to ongoing destruction of CO ice-rich planetesimals. The destruction cascade itself may be triggered by an unseen body that

is also responsible for producing the arc: as a spiral arm.

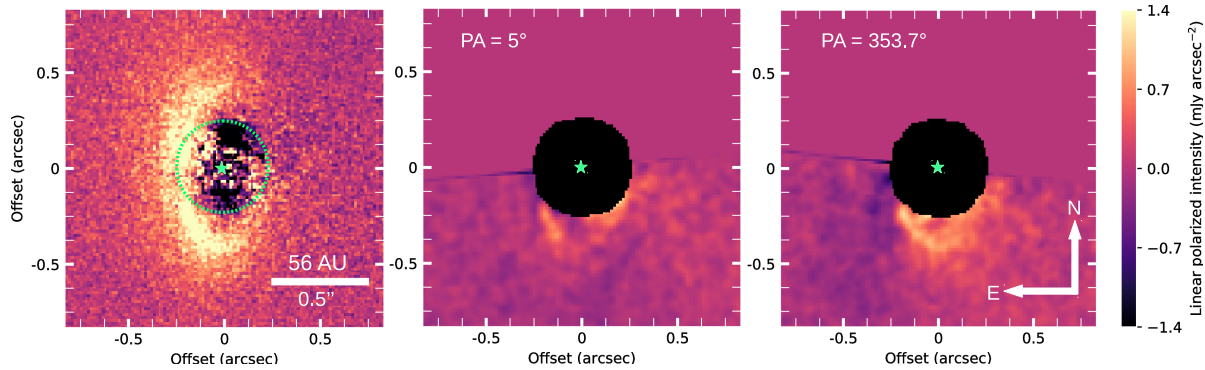


Figure 3.8 Revealing the southern arc on the 44 AU dust ring around HD 141569A by mirroring the northern part of the disk and subtracting it from the southern part. *Left*: The polarized intensity image from GPI. *Middle*: Mirroring and subtraction, assuming the best-fit geometry of the model of the GPI polarized light H -band emission. *Right*: Mirroring and subtraction, assuming the inferred geometry of the SPHERE total intensity H -band emission.

Spiral arm structures have been discovered in near-IR scattered light imaging observations of a few circumstellar disks (e.g., AB Aur, [Hashimoto et al. 2011](#); HD 142527, [Avenhaus et al. 2014](#); SAO 206462, [Muto et al. 2012](#); MWC 758, [Grady et al. 2013](#); HD 100453, [Wagner et al. 2015](#)). Two mechanisms are capable of driving such arms in gas-rich protoplanetary (and transition) disks: gravitational instability (e.g., [Dong et al., 2015a](#)), and interaction between the disk and a planetary or stellar companion. (e.g., [Dong et al., 2015b, 2016b](#)). In optically thin debris disks with much lower gas-to-dust ratios, photoelectric instability ([Klahr & Lin, 2005](#); [Besla & Wu, 2007](#)) may also lead to clumping of dust into structures. Spiral density waves are one of the hypotheses invoked for explaining the radially moving dust enhancements in the edge-on AU Mic debris disk ([Boccaletti et al., 2015](#)). However, typically multiple rings and arcs (i.e., broken rings), instead of one or two spiral arms, are seen in simulations ([Lyra & Kuchner, 2013](#); [Richert et al., 2017](#)). While the HD 141569A disk is almost certainly too low in mass to be gravitationally unstable, the possibility that the detected spiral-arm-like feature is driven by an unseen planet is exciting. [Dong et al. \(2016a\)](#) showed that spiral arms driven by giant planets in disks at modest to high inclinations may appear very close to, or be part of, the disk ring sculpted by the planet. In particular, the 50° and 60° inclination panels in Fig. 8

in [Dong et al. \(2016a\)](#) show intriguing similarities with the HD 141569A inner-disk spiral arm in Fig. 7. The weak contrast of the arm in HD 141569 A indicates that if it is planet-driven, the planet is most likely Jovian or smaller ([Dong & Fung, 2017](#)).

3.5.3 Disk Opening Angle

While it is much less powerful a constraint than it is in (optically thick) protoplanetary disks, our modeling allows us to place approximate constraints on the opening angle or scale height of the resolved inner disk. The best-fit model indicates a rather large reference scale height of $H_0 = 14$ AU at the $R_0 = 45$ AU reference radius, so an opening angle of 17° . This is above expectations even for a transitional disk, although values as small as 10% are within the 84% confidence limit. With such a large disk opening angle, the best-fit model incorporates significant scattering at angles smaller than the $\sim 30^\circ$ expected from a perfectly flat disk (given inclination of $i \sim 60^\circ$). However, if our Mie theory-derived scattering phase function is wrong, this constraint is not to be trusted.

Previous determinations of the opening angle range from 5%–10% ([Thi et al., 2014](#)) to 23% ([Merín et al., 2004](#)). The latter is from SED fitting alone, and while consistent with our finding, it is not very well constrained. The [Thi et al.](#) determination pertains to the gas disk geometry and is constrained from *Herschel* measurements of the $[C_{II}]/CO J = 3 - 2$ line flux ratio, which traces the efficiency of CO photodissociation as a function of gas scale height. However, without having spatially resolved the inner disk, [Thi et al.](#) adopt a model with a gas surface density peak at ≈ 28 AU (Fig. 6 in that paper), whereas we resolve the brightness peak of the inner dust disk at 44 AU (Fig. 3.5). If the gas and the dust are well-mixed, as assumed by [Thi et al.](#), then a cooler gas disk would require a greater scale height to produce the same $[C_{II}]/CO J = 3 - 2$ line flux ratio. It is therefore likely that under the joint constraints from the *Herschel* gas abundances and the GPI resolved dust disk morphology, the gas disk has a $>10\%$ opening angle consistent with the wide dust disk opening angle found here.

3.5.4 Independent Constraint on the Minimum Grain Size from Polarimetry

Our model of the polarized scattered light (Section 4.4.2) produced a minimum grain size of $a_{\min} = 4_{-2}^{+4}\mu\text{m}$, consistent with the $4.2\mu\text{m}$ blow-out grain radius around HD 141569A.

Our best-fit value is marginally consistent with previous findings from scattered light observations (Marsh et al., 2002; Mawet et al., 2017) but differ from values from SED modeling (Thi et al., 2014; Mawet et al., 2017). From resolved mid-IR observations with Keck II Marsh et al. (2002) infer a best-fit ($\chi_v^2 = 1.23$) minimum grain size of $1\text{--}3\mu\text{m}$ —in agreement with our findings—although fits with using ISM-sized $0.1\mu\text{m}$ ($\chi_v^2 = 1.40$) or large blackbody grains ($\chi_v^2 = 1.50$) are also satisfactory. More recently, Mawet et al. (2017) find that a population of dust particles of pure olivines with $a_{\min} = 10\mu\text{m}$ provides the best fit to the resolved L_p -band scattered light emission between 20–90 AU. However, Mawet et al. also find that a minimum grain size of $0.5\mu\text{m}$ is required to fit the SED best. This echoes the finding from SED modeling by Thi et al. (2014). Furthermore, the combined best fit to the L_p image and SED in Mawet et al. (2017) returns $a_{\min} = 0.1\mu\text{m}$.

The preference for very small ($0.1\text{--}0.5\mu\text{m}$) grains in SED modeling points to the presence of a warm dust component that may not be well represented by an extrapolation of an index $n = 3.5$ (collisionally-dominated) grain size distribution below $1\mu\text{m}$. The collisional cascade may not be equally efficient at all grain sizes, or at all radial separations in the disk. For example, a recent estimate from multi-band 0.99 mm ALMA and VLA data shows that at least for mm-sized grains the size distribution index is $n = 2.95 \pm 0.1$ (White et al., 2018).

Our polarization observations are uniquely diagnostic of the presence of sub-micron grains because of their polarization properties. Specifically, scattered light models with a significant population of $a_{\min} < 0.8\mu\text{m}$ are rejected because they produce negative polarization in Stokes Q_r that is not observed by GPI. We similarly rule out highly porous ($p > 60\%$) materials. Thus, with the added power of near-IR polarimetry, we conclude that the population of $\leq 1.0\mu\text{m}$ grains in the 44 AU dust ring is not significant enough to be detectable in polarized light.

A trace population may nonetheless exist, and could be responsible for the observed PAH emission. We use this result to argue for a fourth, innermost and unseen component of the HD 141569A debris disk in Section 3.5.5.

3.5.5 An Unseen Innermost (Fourth) Ring

Our best-fit model to the light-polarizing dust offers a good match to the $\lambda \gtrsim 50\mu\text{m}$ SED (Figure 3.7). However, there is remnant excess emission between 8–30 μm that is not reproduced by our dust model. The presence of warm circumstellar material well within 100 AU has been inferred not only from the above-mentioned SED fitting by Thi et al. (2014) and Mawet et al. (2017), but also from CO observations (Merín et al., 2004; Goto et al., 2006; Fisher et al., 2000; Thi et al., 2014; Flaherty et al., 2016; White et al., 2016). Our detection of an inner clearing within the 44 AU ring, and the lack of polarization signal from sub-micron-sized grains (Section 3.5.4), imposes new constraints on the spatial extent of the warm dust responsible for the excess thermal emission at shorter wavelengths.

To account for this missing flux, we employ a simple model in MCFOST assuming the same grain size distribution, $a_{\text{min}} = 4\mu\text{m}$, $a_{\text{max}} = 1\text{mm}$, porosity of 0% and magnesium-rich olivines from our best-fit model. Motivated by Thi et al. (2014), the dust is characterized by a radial density distribution $R \propto r^p$ with $p = 1$, no flaring ($\beta = 1$) and an inner disk radius of $R'_{\text{in}} = 5$ AU. We keep the outer radius R'_{out} , and dust mass M'_{dust} of the innermost disk as free parameters.

The best-fit thermal model for the innermost disk (light blue dashed line in Figure 3.7) indicates 300 K dust with a mass of $10^{-8}M_{\odot}$ ranging from $R'_{\text{in}} = 5.0$ AU up to $R'_{\text{out}} = 15$ AU. This is well within the coronagraph IWA of GPI, and so presently undetectable in scattered light.

3.6 Conclusion

We have presented the first polarimetric detection of the inner 44 AU disk component of the pre-main sequence star HD 141569A. *H*-band polarimetric differential imaging with GPI has revealed a non-uniform ring-shaped optically-thin dusty disk inwards to $0''.25$, at the highest signal-to-noise ratio attained to date. We find that the disk can be described radially with a combination of two power laws that peaks at 44 AU and extends out to 100 AU. Radiative transfer modeling suggests that the dust grains probed by our polarimetric observations are close to the blow-out size for this system: as might be expected from continuous collisional replenishment in a gas-poor disk. The disk also features an arc-like overdensity along the southern part that is reminiscent of the spiral arm structures previously known at larger scales in this system. The existence of this inner spiral arm structure and its co-location with CO emission detected by ALMA indicates that this may be a site of on-going icy grain destruction, perhaps driven by an unseen planetary perturber. The best-fit model to our polarimetry data indicates an optically-thin disk with a maximum surface density of $r_{max} \simeq R_c = 44_{-12}^{+8}$ AU, a steep inner gradient ($\alpha_{in} = 14$), and a shallower outer exponent ($\alpha_{out} = -1.0_{-1.0}^{+0.5}$). The polarimetric observations are best described by a dust population model with a minimum size of $4_{-2}^{+4} \mu\text{m}$ and a mass of $1.0 \pm 0.4 \times 10^{-6} M_{\odot}$ for non-porous grains up to 1 mm in size. A significant population of sub-micron grains is independently excluded by the lack of negative signal in the *H*-band Stokes Q_r image. We use the thermal emission from our best-fit model to estimate the amount of unseen dust inwards of 28 AU. We find that a fourth innermost dust population, potentially a 5–15 AU belt, is required to fully reproduce the 8–30 μm SED.

With our new high-SNR polarimetric detection of the 44 AU ring, the richness of the circumstellar environment around HD 141569A can be appreciated under a new light. Considering resolved imaging data from other high-contrast facilities, the HD 141569A debris disk shapes up to be made of at least three, and potentially four nested rings, with spiral structures on the three spatially resolved rings. As such, it is an excellent laboratory for studying dynamically perturbed disks.

3.6.1 Acknowledgments:

The Gemini Observatory is operated by the Association of Universities for Research in Astronomy, Inc., under a cooperative agreement with the NSF on behalf of the Gemini partnership: the National Science Foundation (United States), the National Research Council (Canada), CONICYT (Chile), the Australian Research Council (Australia), Ministerio da Ciencia, Tecnologia e Inovacao (Brazil), and Ministerio de Ciencia, Tecnologa e Innovacion Productiva (Argentina). This research was supported in part by a Discovery Grant by the Canadian Natural Sciences and Engineering Council (NSERC) to S.M., and by NSF grant AST-1413718 (GD). P.K. and J.R.G. thank support from NSF AST-1518332, NASA NNX15AC89G and NNX15AD95G/NEXSS. This work benefited from NASAs Nexus for Exoplanet System Science (NExSS) research coordination network sponsored by NASA's Science Mission Directorate. Portions of this work were performed under the auspices of the U.S. Department of Energy by Lawrence Livermore National Laboratory under Contract DE-AC52-07NA27344.

Bibliography

Arenou, F., Luri, X., Babusiaux, C., et al. 2017, *A&A*, 599, A50

Augereau, J. C., Lagrange, A. M., Mouillet, D., & Ménard, F. 1999a, *A&A*, 350, L51

Augereau, J. C., Lagrange, A. M., Mouillet, D., Papaloizou, J. C. B., & Grorod, P. A. 1999b, *A&A*, 348, 557

Avenhaus, H., Quanz, S. P., Schmid, H. M., et al. 2014, *ApJ*, 781, 87

Besla, G., & Wu, Y. 2007, *ApJ*, 655, 528

Boccaletti, A., Thalmann, C., Lagrange, A.-M., et al. 2015, *Nature*, 526, 230

Burns, J. A., Lamy, P. L., & Soter, S. 1979, *Icarus*, 40, 1

- Canovas, H., Ménard, F., de Boer, J., et al. 2015, *A&A*, 582, L7
- Clampin, M., Krist, J. E., Ardila, D. R., et al. 2003, *AJ*, 126, 385
- Currie, T., Grady, C. A., Cloutier, R., et al. 2016, *ApJ*, 819, L26
- Cutri, R. M., Skrutskie, M. F., van Dyk, S., et al. 2003, *VizieR Online Data Catalog*, 2246
- De Rosa, R. J., Nielsen, E. L., Blunt, S. C., et al. 2015, *ApJ*, 814, L3
- Dohnanyi, J. S. 1969, *J. Geophys. Res.*, 74, 2531
- Dong, R., & Fung, J. 2017, *ApJ*, 835, 38
- Dong, R., Fung, J., & Chiang, E. 2016a, *ApJ*, 826, 75
- Dong, R., Hall, C., Rice, K., & Chiang, E. 2015a, *ApJ*, 812, L32
- Dong, R., Zhu, Z., Fung, J., et al. 2016b, *ApJ*, 816, L12
- Dong, R., Zhu, Z., Rafikov, R. R., & Stone, J. M. 2015b, *ApJ*, 809, L5
- Fisher, R. S., Telesco, C. M., Piña, R. K., Knacke, R. F., & Wyatt, M. C. 2000, *ApJ*, 532, L141
- Flaherty, K. M., Hughes, A. M., Andrews, S. M., et al. 2016, *ApJ*, 818, 97
- Goto, M., Usuda, T., Dullemond, C. P., et al. 2006, *ApJ*, 652, 758
- Grady, C. A., Muto, T., Hashimoto, J., et al. 2013, *ApJ*, 762, 48
- Hashimoto, J., Tamura, M., Muto, T., et al. 2011, *ApJ*, 729, L17
- Hauschildt, P. H., Allard, F., & Baron, E. 1999, *ApJ*, 512, 377
- Høg, E., Fabricius, C., Makarov, V. V., et al. 2000, *A&A*, 355, L27
- Hughes, A. M., Wilner, D. J., Kamp, I., & Hogerheijde, M. R. 2008, *ApJ*, 681, 626

- Hung, L.-W., Bruzzone, S., Millar-Blanchaer, M. A., et al. 2016, Gemini planet imager observational calibration XII: photometric calibration in the polarimetry mode, doi:10.1117/12.2233665
- Jaschek, C., & Jaschek, M. 1992, A&AS, 95, 535
- Jaschek, M., Jaschek, C., & Egret, D. 1986, A&A, 158, 325
- Kalas, P., & Jewitt, D. 1995, AJ, 110, 794
- Klahr, H., & Lin, D. N. C. 2005, ApJ, 632, 1113
- Konishi, M., Grady, C. A., Schneider, G., et al. 2016, ApJ, 818, L23
- Kóspál, Á., Moór, A., Juhász, A., et al. 2013, ApJ, 776, 77
- Lagage, P. O., & Pantin, E. 1994, Nature, 369, 628
- Lagage, P. O., Pel, J. W., Authier, M., et al. 2004, The Messenger, 117, 12
- Lagrange, A.-M., Bonnefoy, M., Chauvin, G., et al. 2010, Science, 329, 57
- Li, A., & Lunine, J. I. 2003, ApJ, 594, 987
- Lyra, W., & Kuchner, M. 2013, Nature, 499, 184
- Macintosh, B., Graham, J. R., Ingraham, P., et al. 2014, Proceedings of the National Academy of Science, 111, 12661
- Maire, J., Ingraham, P. J., De Rosa, R. J., et al. 2014, in Society of Photo-Optical Instrumentation Engineers (SPIE) Conference Series, Vol. 9147, Society of Photo-Optical Instrumentation Engineers (SPIE) Conference Series, 85
- Marois, C., Lafrenière, D., Doyon, R., Macintosh, B., & Nadeau, D. 2006, ApJ, 641, 556
- Marsh, K. A., Silverstone, M. D., Becklin, E. E., et al. 2002, ApJ, 573, 425

- Mawet, D., Choquet, É., Absil, O., et al. 2017, *AJ*, 153, 44
- Mazoyer, J., Boccaletti, A., Choquet, É., et al. 2016, *ApJ*, 818, 150
- Mendigutía, I., Mora, A., Montesinos, B., et al. 2012, *A&A*, 543, A59
- Merín, B., Montesinos, B., Eiroa, C., et al. 2004, *A&A*, 419, 301
- Millar-Blanchaer, M. A., Graham, J. R., Pueyo, L., et al. 2015, *ApJ*, 811, 18
- Mouillet, D., Lagrange, A. M., Augereau, J. C., & Ménard, F. 2001, *A&A*, 372, L61
- Muto, T., Grady, C. A., Hashimoto, J., et al. 2012, *ApJ*, 748, L22
- Perrin, M. D., Maire, J., Ingraham, P., et al. 2014, in *Proc. SPIE*, Vol. 9147, *Ground-based and Airborne Instrumentation for Astronomy V*, 91473J
- Perrin, M. D., Duchene, G., Millar-Blanchaer, M., et al. 2015, *ApJ*, 799, 182
- Perrot, C., Boccaletti, A., Pantin, E., et al. 2016, *A&A*, 590, L7
- Pinte, C., Harries, T. J., Min, M., et al. 2009, *A&A*, 498, 967
- Pinte, C., Ménard, F., Duchêne, G., & Bastien, P. 2006, *A&A*, 459, 797
- Pueyo, L., Soummer, R., Hoffmann, J., et al. 2015, *ApJ*, 803, 31
- Richert, A. J. W., Lyra, W., & Kuchner, M. 2017, *ArXiv e-prints*, arXiv:1709.07982
- Schmid, H. M., Joos, F., & Tschan, D. 2006, *A&A*, 452, 657
- Soummer, R., Pueyo, L., & Larkin, J. 2012, *ApJ*, 755, L28
- Sylvester, R. J., Skinner, C. J., Barlow, M. J., & Mannings, V. 1996, *MNRAS*, 279, 915
- Thi, W.-F., Pinte, C., Pantin, E., et al. 2014, *A&A*, 561, A50
- van de Hulst, H. C. 1957, *Light Scattering by Small Particles*

- Wagner, K., Apai, D., Kasper, M., & Robberto, M. 2015, *ApJ*, 813, L2
- Walker, H. J., & Wolstencroft, R. D. 1988, *PASP*, 100, 1509
- Wang, J. J., Ruffio, J.-B., De Rosa, R. J., et al. 2015, *pyKLIP: PSF Subtraction for Exoplanets and Disks*, *Astrophysics Source Code Library*
- Weinberger, A. J., Becklin, E. E., Schneider, G., et al. 1999, *ApJ*, 525, L53
- Weinberger, A. J., Rich, R. M., Becklin, E. E., Zuckerman, B., & Matthews, K. 2000, *ApJ*, 544, 937
- White, J. A., Boley, A. C., Hughes, A. M., et al. 2016, *ApJ*, 829, 6
- White, J. A., Boley, A. C., MacGregor, M. A., Hughes, A. M., & Wilner, D. J. 2018, *MNRAS*, 474, 4500
- Wyatt, M. C., Dermott, S. F., Telesco, C. M., et al. 1999, *ApJ*, 527, 918
- Zuckerman, B., Forveille, T., & Kastner, J. H. 1995, *Nature*, 373, 494

Chapter 4

An active collisional cascade in the old HD 157587 debris disk deduced from multi-band Gemini Planet Imager polarimetry

A version of this chapter is to be submitted.

Authors: Juan Bruzzone, Stanimir Metchev, Gaspard Duchene, Esposito, Thomas, Schuyler, Wolff, Jason Wang, James R. Graham, Johan Mazoyer, S. Ammons, Adam Schneider, Alexandra Greenbaum, Brenda Matthews, Pauline Arriaga, Vanessa Bailey, Travis Barman, Joanna Bulger, Jeffrey Chilcote, Tara Cotten, Robert De Rosa, Rene Doyon, Michael Fitzgerald, Katherine Follette, Benjamin Gerard, Stephen Goodsell, Pascale Hibon, Justin Hom, Li-Wei Hung, Patrick Ingraham, Paul Kalas, Quinn M. Konopacky, James Larkin, Bruce Macintosh, Jerome Maire, Franck Marchis, Christian Marois, Maxwell Millar-Blanchaer, Katie Morzinski, Eric Nielsen, Rebecca Oppenheimer, David Palmer, Rahul Patel, Jennifer Patience, Marshall Perrin, Lisa Poyneer, Laurent Pueyo, Abhijith Rajan, Julien Rameau, Fredrik Rantakyro, Dmitry Savransky, Anand Sivaramakrishnan, Inseok Song, Remi Soummer, Sandrine Thomas,

J. Wallace, Kimberly Ward-Duong, Alycia Weinberger and Sloane Wiktorowicz.

We present follow-up near-infrared polarimetric observations of the debris disk around the F5V star HD 157587 obtained with the Gemini Planet Imager (GPI). Our detections at J and $K1$ confirm the previous detection with GPI H -band polarimetry of the east half of an 83 AU ring-shaped optically-thin debris disk. Our detections at J and $K1$ also confirm a secondary asymmetry reported at H indicating the the SE portion of the ring is mildly brighter and agrees with an offset of the disk along its semimajor axis. We included the archival H -band detection and derived the disk colors in polarized intensity indicating that the disk is consistently red. Our best-fit radiative transfer model favors a disk with a population of sub-micron ($0.43\mu\text{m}$) porous and micron-sized ($> 30\mu\text{m}$) compact grains. The grain size distribution exponent from the best-fit model is $q = 3.73^{+0.85}_{-0.08}$, consistent with an active collisional cascade in the system. We apply recent GAIA DR2 measurements of HD 157587 to the BANYAN Σ web tool to derive an stellar age consistent with a field star. This indicates that HD 157587 belongs into a small subset of old debris disks.

4.1 Introduction

The detection of nearby young planetary systems in near-IR scattered light has increased significantly in recent years. High-contrast high-angular resolution instruments such as GPI (Macintosh et al., 2014) and SPHERE (Beuzit et al., 2008) currently resolve young planetary systems down to a few tens of AU (Millar-Blanchaer et al., 2015; Hung et al., 2015; Draper et al., 2016; Esposito et al., 2016; Garufi et al., 2017). Of the dozen or so directly imaged planets to date many share a distinctive characteristic: they reside in stellar systems known to also possess circumstellar dust: β Pictoris (Lagrange et al., 2010; Millar-Blanchaer et al., 2015), 51 Eridani b (Macintosh et al., 2015), Fomalhaut (Kalas et al., 2008). Roughly 25% of main sequence stars are known to possess dusty "debris" disks, as manifested by the thermal emis-

sion of warm dust grains (Hughes et al., 2018) and references therein. The detection of such dust, whose presence and dynamics is affected by disruptive processes involving minor bodies, planetary embryos and planets, offers an important pathway for probing the planetary systems themselves.

HD 157587 is an F5V star known to host IR-emitting circumstellar dust with $L_{\text{IR}}/L_{\text{star}} = 7.9 \times 10^{-4}$ (McDonald et al., 2012) at a distance $d = 98.1$ pc (Arenou et al., 2017). Follow-up Hubble Space Telescope (HST)/STIS observations of HD 157587’s $22\mu\text{m}$ WISE excess confirmed dust-scattered light from a projected separation of 90 AU out to 700 AU (Padgett & Stapelfeldt, 2016). This was followed by Millar-Blanchaer et al. (2016) revealing an inner 80 AU (at $d = 107.4$ pc) ring-shaped disk extending out to 216 ± 16 AU with H -band GPI Polarimetric Differential Imaging (PDI). Millar-Blanchaer et al. determined disk inclination and position angles (PA) of $72.2^\circ \pm 0.4^\circ$ and $127.0^\circ \pm 0.3^\circ$ respectively while detecting only half of the disk in the SE-NW direction. The strong polarization detection of one side of the disk is explained as polarized emission by strongly forward-scattered light by dust grains. Millar-Blanchaer et al. (2016) reports a disk offset and three point source candidates and suggest that they are likely unrelated to HD 157587.

Here we present GPI PDI follow-up J - and $K1$ -band observations of the HD 157587 debris disk in scattered light as part of the Long and Large Program GS-2016A-LP-6 on Gemini South (PI Chen). We also include GPI spectroscopy-mode observations in the $K1$ band, and the archival H -band GPI PDI observations from Millar-Blanchaer et al. (2016). We introduce our observations in Section 4.2 and present our results in Sections 4.3.1 through 4.3.3. The modeling procedure is presented in Section 4.4.1 and modeling results in Section 4.4.2. In Section 4.5 we elaborate the discussion and our conclusions are presented in Section 4.6.

4.2 Observations

4.2.1 Observations in Polarimetry Mode

We observed HD 157587 with GPI's polarimetry mode on 2016 March 26 and March 27 UT in the J and $K1$ bands respectively. On 2016 March 26, the sequence consisted of twenty-eight 90 second individual exposures at J ($[1.12 - 1.35]\mu\text{m}$, $\lambda_c = 1.24\mu\text{m}$) for a total of $48^\circ.6$ of cumulative field rotation and an average airmass of 1.02. Due to a technical error, both the Gemini Differential Image Motion Monitor (DIMM) and Multi-Aperture Scintillation Sensor (MASS) seeing recorded at Cerro Pachón remained at $1''.58$ through the entire sequence. However, the AO system telemetry reported a wavefront rms error (AOWFE) of 146 ± 8 nm. On the next night on March 27, the sequence comprised twenty-four two-minute exposures in $K1$ band ($[1.90 - 2.16]\mu\text{m}$, $\lambda_c = 2.05\mu\text{m}$) covering $\sim 32^\circ$ of cumulative parallactic field rotation at an average airmass of 1.04. DIMM and MASS seeing measurements through the sequence averaged $1''.33$ and $0''.55$ respectively with an rms AOWFE of 128 ± 16 nm. In polarimetry mode observations, the half wave plate (HWP) modulator was rotated between exposures at $0^\circ.0$, $22^\circ.5$, $45^\circ.0$ and $67^\circ.5$ degrees. The HWP introduces modulation in the signal at $22^\circ.5$ steps and thus allows for reconstruction of the Stokes vector. We reduced the data with the GPI Data Reduction Pipeline (GPI DRP; [Maire et al., 2014](#); [Perrin et al., 2014](#)) following the procedure described in [Perrin et al. \(2015\)](#). The observing procedure and reduction steps in polarimetry mode with GPI are common to all filters, with the exception of thermal background subtraction in the $K1$ band and flux calibration. The process starts with dark subtraction, thermal background subtraction in the $K1$ band, correction for instrument flexure, microphonics noise, bad pixels and correction for distortion. The individual frames are then assembled into a polarization datacube where the third dimension comprises two slices holding the two orthogonal polarization states as generated by the Wollaston prism. Each cube is 281 pixels on a side times 2 slices. Cubes are then divided by a Gemini Facility Calibration Unit (GCAL) flat field, for throughput correction across the field. The next step includes establishing the position of the

obscured star with a Radon transform-based algorithm (Pueyo et al., 2015). With the position of the star established, the fiducial satellite spots fluxes are measured and stored to perform the flux calibration following Hung et al. (2016). A double differencing follows to remove non-common path errors between the two polarization states in individual frames as described by Perrin et al. (2015). What follows is the correction of instrumental polarization systematics as outlined in Millar-Blanchaer et al. (2015).

The individual difference cubes are shifted to place the occulted star at a common center and then rotated so that north is along the y axis and east is along the x axis. All cubes are then combined following the procedure described in Perrin et al. (2015) to create a Stokes cube based on the waveplate the angle and sky rotation information of each individual exposure. The procedure returns a Stokes datacube $[I, Q, U, V]$ that holds the total intensity, linear and circular polarization information for the entire observation sequence respectively. Because GPI's HWP is not exactly one half wave at all wavelengths, it is not sensitive to circular polarization. This limits the utility of Stokes V , so we opt to disregard the Stokes V slice. We then transform the Stokes cubes using the radial Stokes formalism into Stokes Q_r and Stokes U_r (Schmid et al., 2006). Stokes Q_r maps linear polarization perpendicular to the radial direction from the star: light from single scattering events by dust grains will lead to positive values in Stokes Q_r . Negative values translate into polarization parallel to the radial direction. In optically thin debris disks, all of the flux is expected in the Stokes Q_r image leaving the Stokes U_r as a noise image. However, we note that multiple scattering in optically thick disks could have a Stokes U_r signal of a few percent of the Stokes Q_r signal that is below the sensitivity of the observations (Canovas et al., 2015). We smoothed the observations with a Gaussian kernel ($\sigma = 2\text{pixel}$). The final reduction step includes the flux calibration of the data. Following Hung et al. (2016), we use 0.809 ± 0.04 Jy as the $K1$ band flux of HD 157587 from 2MASS (Cutri et al., 2003) to obtain a conversion factor of $(1.41 \pm 0.07) \times 10^{-8}$ Jy ADU $^{-1}$ coadd $^{-1}$. In a similar fashion, we use the HD 157587 2MASS flux of 1.49 ± 0.04 Jy in J band and obtain a flux calibration factor of $(1.31 \pm 0.06) \times 10^{-8}$ Jy ADU $^{-1}$ coadd $^{-1}$. In addition to our

Stokes Q_r and U_r images, we also obtain the total intensity images (Stokes I) in each band with pyKLIP (Wang et al., 2015), which implements the Karhunen-Loève Image Projection algorithm (KLIP; Soummer et al., 2012) for optimal PSF subtraction.

Lastly, we include ancillary H -band GPI PDI observations from Millar-Blanchaer et al. (2016) following the same reduction steps and flux calibration procedure in that study. Our flux-calibrated H -band reductions are an order of magnitude fainter than the derived in (Millar-Blanchaer et al., 2016) and this is related to a problem with the flux calibration in that study. An Erratum will be submitted soon addressing the flux calibration in Millar-Blanchaer et al. (2016), (Millar-Blanchaer, personal communication).

4.2.2 Observations in Spectroscopy Mode

We observed HD 157587 in $K1$ -band spectroscopy mode with GPI on 2016 March 24 UT. The sequence comprised 53 90-second individual exposures with 47° of cumulative field rotation. The average DIMM and MASS seeing for this sequence was $1''.57$ and $0''.47$ respectively, at an average airmass of 1.04. The telemetry data recorded a rms AOWFE of 143 ± 10 nm. We use the GPI DRP to reduce the spectroscopic sequence following the standard steps outlined in Perrin et al. (2014). In GPI's spectroscopy mode, a single observation includes thousands of individual micro-spectra that are extracted and assembled into a datacube. Datacubes are 281×281 pixel arrays plus a third dimension comprising 37 spectral channels covering the filter band pass. The basic reduction process is similar to polarization observations: dark and thermal background subtraction, correction for instrument flexure, microphonics, distortion and bad pixels. The star location and photometric calibration in each channel is determined from measurements of four fiducial satellite spots. The satellite spots are diffracted realizations of the star generated by the grid imprinted in GPI's apodizer (Sivaramakrishnan & Oppenheimer, 2006) with a known star:spot flux ratio in $K1$ band of 2.695×10^{-4} (Wang et al., 2014; Pueyo et al., 2015; Maire et al., 2014). We then flux-calibrated the observations with the 2MASS stellar K flux of 0.809 ± 0.04 Jy. In this paper we only consider the broadband-collapsed results

from the spectral data cubes; leaving the consideration and analysis of the disk's $K1$ spectrum in scattered light for future work.

4.3 Results

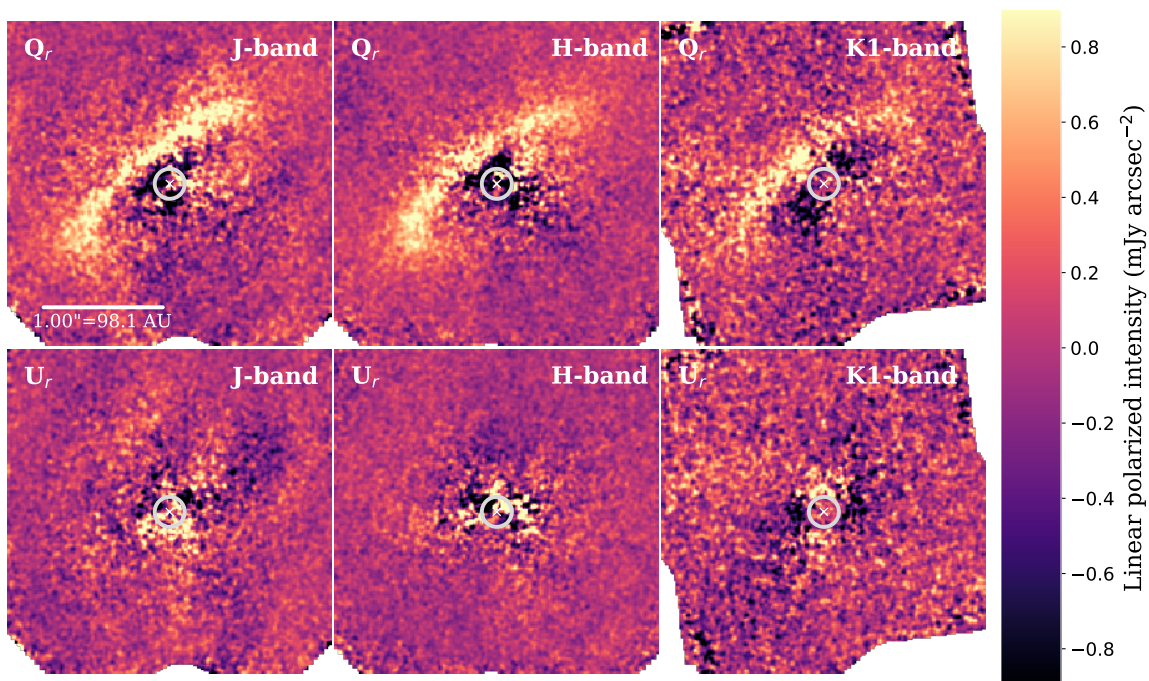


Figure 4.1 Surface brightness detections of the HD 157587 debris disk in J , H and $K1$ bands in linear polarized light with GPI PDI. *Top*: Stokes Q_r images. *Bottom*: Stokes U_r images shown on the same color scale. North is up along the y axis and east is to the right on the x axis. The location of the star is marked with a cross and a circle of radius $0''.12$ indicates the size of the FPM. All observations were acquired with the H -band apodizer FPM. The Stokes U_r frames show a small region in the vicinity of the FPM affected by uncorrected instrumental polarization. Beyond this region, the U_r images scatter largely uniformly around zero flux indicating single scattering events from circumstellar dust grains.

4.3.1 Polarized Intensity Images

We present the detections of the HD 157587 disk in linear polarized intensity with GPI PDI in Figure 4.1. Our polarized detections of the disk in the J and $K1$ bands confirm the previous

detection in the H band with GPI PDI (Millar-Blanchaer et al., 2016). Our Stokes Q_r observations recover the overall morphology and orientation of the ring-shaped disk revealing the eastern side peaking at $0''.85$ (83 AU at $d = 98$ pc) and extending out to about $\sim 1.3''$ along its semimajor axis. This one-sided asymmetry is a common feature in previous disk detections with GPI PDI, for example: HD 131835 (Hung et al., 2015) and HD 141569A (Bruzzone et al., 2019). It is interpreted as the result of preferential forward scattering by dust grains in a tilted disk, such that the brighter side is closer to the observer. The Stokes U_r images scatter around zero flux and contain no clear disk signal. The J -band Stokes U_r image seems affected by a residual quadrupole pattern outside of $0''.12$ with increased positive and negative flux at $\sim 0''.2$ and $1''$ respectively at $PA\ 315^\circ$. We consider this to be an artifact of the reduction process and not a disk feature. The overall uniform zero-median distribution in the Stokes U_r , supports the detection of an optically-thin dusty disk. The polarized light at all three wavelengths share the common morphology of a ring-shaped disk.

Besides the strong NE-SW brightness asymmetry, the surface brightness of the disk is not uniform in the azimuthal direction. The polarized disk detection in J band looks slightly brighter towards the NW ansa, in contrast with a mildly brighter surface brightness towards SE portion in the Q_r $K1$ detection. The latter agrees with the mild brightness asymmetry visible in the H band and reported by Millar-Blanchaer et al. (2016). However, it is possible that the discrepant surface brightness asymmetry at J may not be real. It could be related to low spatial frequency residuals arising from the reduction and acquisition process and related to the quadrupole pattern in the Stokes U_r that shows an undulation across $\sim 0''.4 - 0''.7$.

Figure 4.2 shows maps of the signal-to-ratio (SNR) of the polarized detections of the disk. Following Millar-Blanchaer et al. (2015), we derive an uncertainty map σ in each filter as the standard deviation of the Stokes U_r image in 3-pixel wide concentric annuli. We then compute the SNR in each filter by dividing the Stokes Q_r over the uncertainty map σ . The highest SNR values are located towards the ansae and away from the minor axis of the disk. The dichotomy is most pronounced in the J and H bands. This is not surprising as we expect

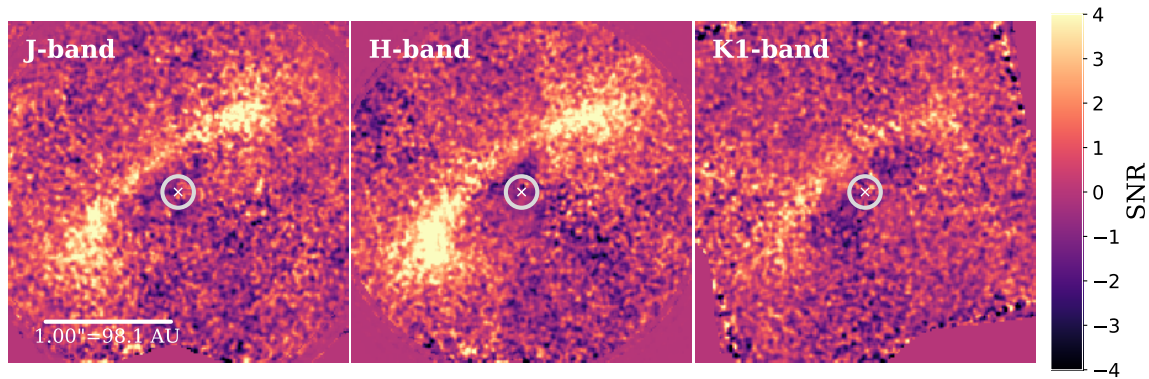


Figure 4.2 SNR maps of HD 157587 in J , H and $K1$ bands. The maps are constructed by dividing the Q_r image by the standard deviation of all pixels within a 3 pixel-wide annulus in the U_r image at the same angular separation from the star.

higher uncertainties closer to the coronagraph. In contrast, the $K1$ -band SNR map indicates a weaker detection with slightly stronger emission for the rim of the disk towards the SE, not revealing as much of the back side towards the ansae as in the J and H detections.

4.3.2 Total Intensity Images

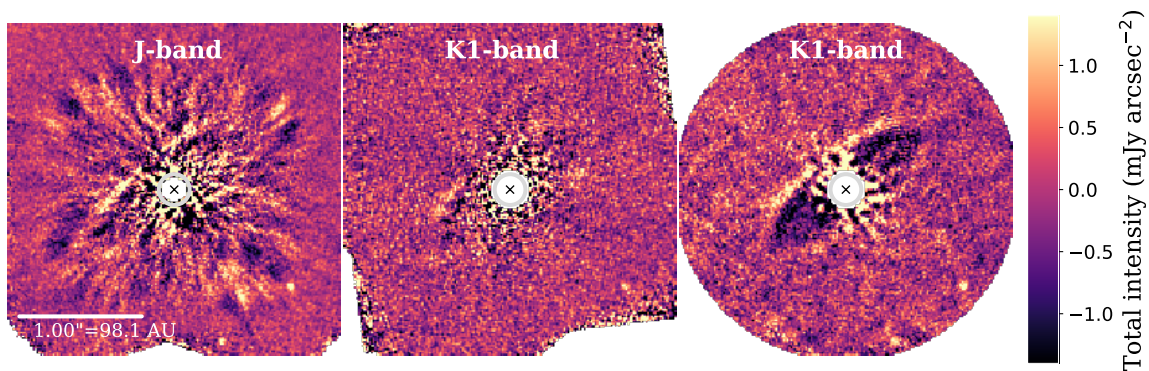


Figure 4.3 HD 157587's disk KLIP+ADI reductions in the J , and $K1$ bands in total intensity. *Left and Center:* total intensity images from polarimetric sequences on 2016 March 26 and March 27 UT. *Right:* broadband-collapsed spectral datacube in spectroscopy mode. North is up along the y axis and east is to the right on the x axis. Visible to the SW are two of the three candidate point sources identified in [Millar-Blanchaer et al. \(2016\)](#).

We present our observations of the HD 157587 disk in total intensity in Figure 4.3. Our PSF-subtracted reductions in total intensity returned mixed results with a more favorable de-

tection of the disk coming from the $K1$ spectroscopic sequence. The thin rim-like appearance of the disk in these reductions is a common outcome of applying KLIP+ADI on circumstellar disks. KLIP+ADI excels in removing the stellar speckle halo to reveal faint point sources at small inner angular separations. However, this process also washes out low spatial frequency features, usually leaving only a thin silhouette of the disk. Applying KLIP+ADI to our polarization sequences did not lead to the recovery of the disk, especially for the $K1$ sequence where only a hint of the bright side is retrieved. Only the spectrally-collapsed spectroscopic sequence returns a detection of the eastern side and hints at the presence of the back of the disk. However, there are substantial PSF subtraction artifacts in the vicinity of the coronagraph that hampers the recovery of the disk's signal close to its semi-minor axis. The area interior to the disk is not suitable for analysis as it suffers from substantial PSF over subtraction residuals. The strong attenuation of the disk signal towards the ansae and the PSF reduction artifacts near the front side of the disk makes it difficult to retrieve meaningful estimates of the flux. We proceed to model the Stokes Q_r detections at J , H and $K1$ in the remainder of this study and leave the study of the total intensity detection in spectroscopy mode for future work. The difficulty to detect the disk in total intensity highlight the power of PDI to retrieve the extended scattered-light images of debris disk that are virtually free of PSF subtraction systematics.

KLIP + ADI reveals two of the three candidate point sources identified in [Millar-Blanchaer et al. \(2016\)](#); cc1 and cc2 in that study. We do not detect the fainter candidate companion cc3 in neither J nor $K1$ strongly suggest that it was not a stellar object. Our deeper sequences in J and $K1$ should have allowed us to recover the object given the deeper coverage at a slightly shorter and a slightly longer wavelength. We therefore conclude that cc3 in [Millar-Blanchaer et al. \(2016\)](#) was an artifact. We focus on candidates cc1 and cc2 and use the KLIP+ADI reduction in [Millar-Blanchaer et al. \(2016\)](#) and our spectroscopically-collapsed reduction to assess the relative motion of these objects in two epochs roughly 7 months apart (0.578 yr). A quick inspection of the relative motion of the candidates cc1 and cc2 indicates an offset in declination with respect of their initial positions of $0.015 \pm 0.002''$ and $0.016 \pm 0.002''$ respectively. In right

ascension, the offset is $0.022 \pm 0.002''$ and $0.024 \pm 0.002''$ respectively. The GAIA DR2 proper motion in declination of HD 157587 is $-31.24 \pm 0.06 \text{ mas yr}^{-1}$ and $-3.89 \pm 0.11 \text{ mas yr}^{-1}$ in right ascension (Gaia Collaboration et al., 2016, 2018). Thus, the position of HD 157587 near the galactic plane and the relative offsets suggest that these point sources are likely not associated with HD 157587.

4.3.3 Disk Colors

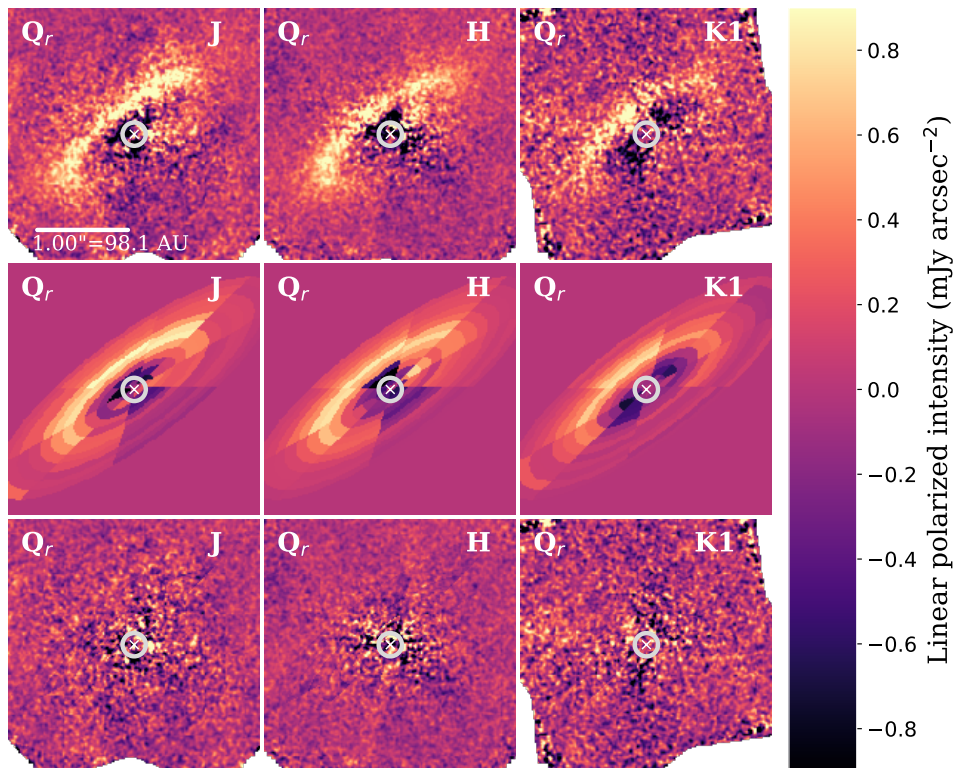


Figure 4.4 Disk photometry maps with the estimated mean surface brightness the HD 157587 disk and residuals. Each map is divided in eight sectors in the azimuthal direction, rotating counter-clockwise, with sector 1 being towards the NE, along the semi-minor axis. In this way, sectors one to three, and sectors seven and eight cover the eastern side of the disk. Radially, the grid is divided in 12 10-pixel wide annuli. For each sector and annuli interval, a mean surface brightness and standard deviation is calculated generating a map of the disk photometry.

In the absence of a clean detection of the disk in total intensity, we generate photometry maps of the disk to estimate the disk NIR colors from the Stokes Q_r detections. With the disk

	$P_{J-H}(\text{mag})$	$P_{H-K1}(\text{mag})$	$P_{J-K1}(\text{mag})$
sector 1	0.43 ± 0.07	0.36 ± 0.11	0.67 ± 0.10
sector 2	0.34 ± 0.05	0.21 ± 0.10	0.59 ± 0.10
sector 3	0.30 ± 0.06	0.73 ± 0.17	1.26 ± 0.18
sector 7	0.64 ± 0.08	0.40 ± 0.17	1.28 ± 0.24
sector 8	0.15 ± 0.05	0.14 ± 0.12	0.25 ± 0.12

Table 4.1: Stokes colors of the HD 157587 disk. Colors are estimated as from flux ratios of the Stokes Q_r photometry maps and divided by the stellar fluxes.

photometry, we compute the Stokes colors:

$$P_{\lambda_1-\lambda_2} = -2.5 \log_{10} \left(\frac{f_{*,\lambda_2} f_{\text{disk},\lambda_1}}{f_{*,\lambda_1} f_{\text{disk},\lambda_2}} \right) \quad (4.1)$$

where $f_{*,\lambda}$ and $f_{\text{disk},\lambda}$ is the stellar flux and disk flux at filters with central wavelength λ respectively. For each filter, the photometry map comprises an elliptical grid centered on the star and constructed with the same orientation and aspect ratio of the disk. This is used to estimate the projected stellocentric distances in the plane of the sky due to the disk orientation. Figure 4.4 shows the disk photometry maps over the Stokes Q_r observations and residuals. We compute P_{J-H} , P_{J-K1} and P_{H-K1} as estimators of the disk broad-band color in polarized intensity. We consider the 2MASS stellar fluxes $f_{*,J} = 1.49 \pm 0.04$ Jy, $f_{*,H} = 1.16 \pm 0.04$ Jy and $f_{*,K1} = 0.809 \pm 0.02$ Jy. We use this estimator as a proxy for the scattering efficiency of dust grains. We compute the weighted average in each region and propagated the uncertainties and added them in quadrature. Table 4.1 shows the estimated average broad-band colors of HD 157587's disk across different sectors of the photometry maps. After removing the stellar color, the disk appears consistently red as more light is scattered at longer wavelengths.

Param.	Prior Range	Max Lk	16%-tile	50%-tile	84%-tile
R_c (AU)	(50,110)	81.9	81.5	82.6	86.5
R_{out} (AU)	(140,350)	253	214	246	272
H_0 (AU)	(2.0,69)	8.8	7.4	8.8	9.7
α_{in}	(0,9.5)	7.3	6.7	7.1	7.6
α_{out}	(-5,0)	-2.9	-3.3	-3.0	-2.8
γ	(0.1,3.0)	1.0	0.80	0.95	1.1
M_d (M_{\oplus})	(0.00007,16.7)	0.17	0.10	0.18	1.3
a_{min} (μm)	(0.1, 80)	0.42	0.41	0.43	26.47
q	[2, 6)	3.70	3.65	3.73	4.59
p (%)	[0,100)	70	5.0	70	71

	J band	H band	$K1$ band
Minimum reduced χ^2	1.20	1.13	1.15
Combined minimum reduced χ^2	1.16		

Table 4.2: Parameters probed in our exploration grid of debris disk models with MCFOST and best-fit values for the Stokes Q_r images in J , H and $K1$ filters.

4.4 Disk Modeling

4.4.1 Parametrization of the Dust Model

We model the HD 157587 disk Stokes Q_r images computing synthetic observations with the radiative transfer code MCFOST (Pinte et al., 2006, 2009). We use a modified version of the modeling procedure presented in Bruzzone et al. (2019) to simultaneously fit the disk Stokes Q_r polarimetric detections at J , H and $K1$. To fit models to the data we use the affine invariant Markov Chain Monte Carlo (MCMC) ensemble sampling package emcee (Foreman-Mackey et al., 2013). Our modeling adopts Mie scattering theory for the treatment of photon scattering by idealized spherical dust grains. The spatial sampling of our synthetic observations matches GPI’s pixel scale of GPI of 14.166 ± 0.007 mas lenslet⁻¹ (De Rosa et al., 2015) and covers GPI’s field of view. The disk is centered on the star, the latter located at the center of the spatial grid. We derive the stellar luminosity by fitting HD 157587’s optical to near-IR SED using the VO SED Analyzer Tool (VOSA; Bayo et al., 2008). The fitting used NextGen (Hauschildt et al.,

1999) and Kurucz (Kurucz, 1993) photospheric models. We assumed a fixed distance of 98.1 pc (Arenou et al., 2017), reddening $R_V = 3.1$ while keeping the stellar effective temperature (T_{eff}) and radius (R) as variables. The best-fit model returned a luminosity of $3.08 \pm 0.3 L_{\odot}$, $T_{\text{eff}} = 6400 \pm 100$ K and $R = 1.43 \pm 0.06 R_{\odot}$ using the NextGen photospheric model. The best-fit radius and effective temperature agrees within uncertainties with previous estimates by Masana et al. (2006) and McDonald et al. (2012).

The disk is parametrized within MCFOST as an azimuthally symmetric ring in cylindrical coordinates: r is the distance on the equatorial plane and z the height above the disk mid-plane. We set the disk orientation by adopting the best-fit inclination of $72.2^{\circ} \pm 0.4^{\circ}$ and PA of $127.0^{\circ} \pm 0.3^{\circ}$ from Millar-Blanchaer et al. (2016). The dust density distribution is parametrized as follows:

$$\rho(r, z) \propto \frac{\exp\left(-\frac{|z|}{H(r)}\right)^{\gamma}}{\left\{\left(\frac{r}{R_c}\right)^{-2\alpha_{\text{in}}} + \left(\frac{r}{R_c}\right)^{-2\alpha_{\text{out}}}\right\}^{-1/2}}. \quad (4.2)$$

The scale height is $H(r) = H_0 \left(\frac{r}{R_0}\right)^{\beta}$, with R_0 fixed at 86 AU while β controls the flaring of the disk. We assume a disk with a constant opening angle, $\beta = 1$, as appropriate for a gas-poor debris disk. We set $R_0 = 86$ AU because that distance approximates the radial distance to the midpoint of the ring along its semimajor axis. Radially, the extension of the disk has limits R_{in} and R_{out} . We hold R_{in} fixed at 20 AU as preferred in initial exploratory modeling and keep R_{out} as a free parameter. The critical radius R_c divides the disk into two regions: an inner region inwards of R_c controlled by the surface density power law index $\alpha_{\text{in}} > 0$, and an outer region described by a surface density power law index $\alpha_{\text{out}} < 0$ onwards.

The surface brightness and thermal flux of the disk is controlled by the total mass in grains in the disk M_d . Dust grains populate the disk following a power-law size distribution $dN(a) \propto a^{-q} da$. The size distribution has limits a_{min} and a_{max} and grain porosity p . We fix $a_{\text{max}} = 1$ mm and leave a_{min} as a free parameter in the model. Within the MCFOST framework, the refractive index of porous grains is approximated by mixing the grain's material with void particles following Bruggeman mixing rule. Our modeling accounts for a single dust grain

composition of "astronomical" silicates (Draine & Lee, 1984) with a dust grain density $\rho_{\text{dust}} = 3.5 \text{ g cm}^{-3}$.

The list of free parameters explored in our modeling thus comprises: R_{out} , H_0 , M_d , α_{in} , α_{out} , R_c , a_{min} , q , γ , and p .

4.4.2 Modeling Procedure and Best-Fit Estimates

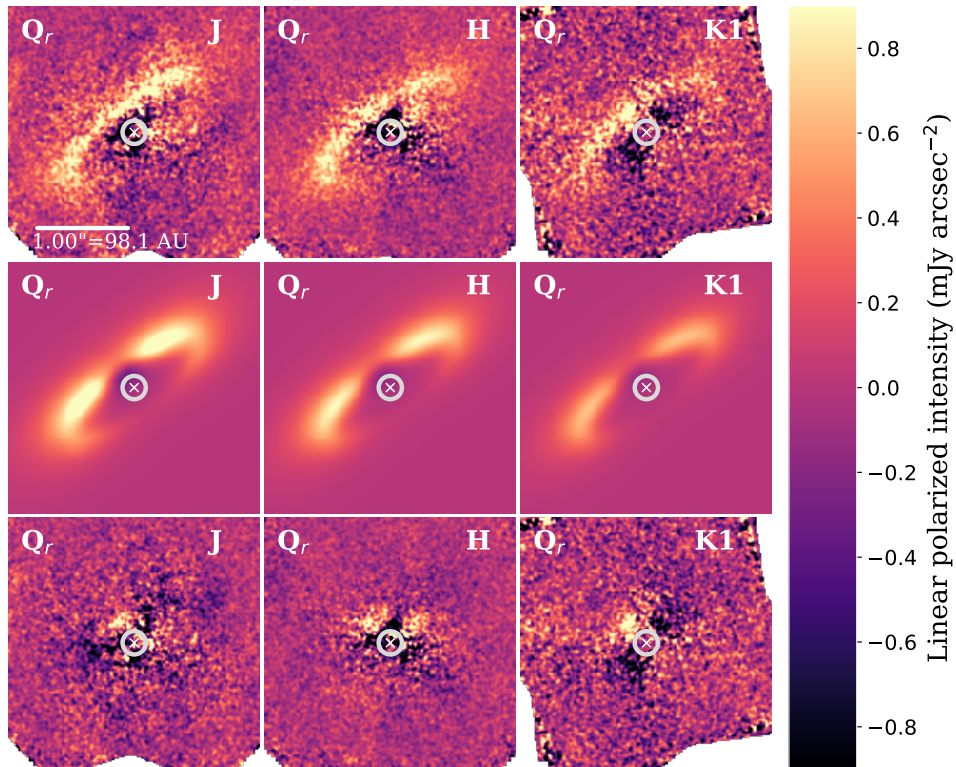


Figure 4.5 *Top*: Observations of HD 157587's disk in *J*, *H* and *K1* bands, *Middle*: Best-fit models, *Bottom*: Residuals of the best-fit models. Images are displayed on the same colorscale and orientation as Figure 4.1.

Prior to our fitting procedure, we applied a binning factor of 3 to our observations to mitigate the effects of correlated errors. We use these binned observations in our modeling procedure. Although GPI's PSF is about [2.7–4.4] pixels in our 1.24 – 2.05 μm observations, we favor the use of binning images to reduce the computation time of our individual models at the expense of losing spatial information. Following (Millar-Blanchaer et al., 2015), we use

the 3×3 binned Stokes U_r images in each filter to produce uncertainty maps σ respectively as described in Section 4.3.

We employ a parallel-tempered MCMC with three temperatures, each with 160 walkers for every parameter we explore. The walkers were initialized with random values drawn from a uniform distribution. The procedure starts with walker chains evolving in each iteration within the boundaries set by a flat prior listed in Table 4.2. The walker chains reached 3800 iterations (1.824×10^6 model realizations) before converging. Figure 4.6 shows the marginalized posterior distributions from the modeling procedure and Figure 4.5 shows the best-fit model.

Table 4.2 lists the maximum likelihood values returned by our modeling procedure along with values at the 16th, 50th (i.e., median), and 84th percentiles. The maximum likelihood values are very similar to those at the 50th percentile. The 50th percentile and maximum likelihood models are virtually indistinguishable from their reduced χ^2 . Thus we adopt the median values as the best-fit parameters hereafter. Our modeling favors a disk with $R_c = 82.6_{-1.2}^{+2.7}$ AU for a dust density distribution extending out to $R_{out} = 246_{-33}^{+26}$ AU and controlled by steep inner slope parameter $\alpha_{in} = 7.2_{-0.5}^{+0.4}$ and shallower $\alpha_{out} = -3.0_{-0.3}^{+0.2}$. The scale height of the disk is $H_0 = 8.8_{-1.5}^{+0.8}$ AU (at $R_0=86$ AU) with a vertical density profile exponent $\gamma = 0.95_{-0.17}^{+0.16}$. The dust size distribution is controlled by an index $q = 3.73_{-0.08}^{+0.81}$ and it is in good agreement with the value of $q = 3.5$ inferred from steady-collisional models (Dohnanyi, 1969; MacGregor et al., 2016). This value for q is above the estimated values associated with zodiacal dust ($q \sim 2 - 2.5$; Leinert et al., 1976; Grun et al., 1985) and suggest a steady supply of small grains in the system. The dust mass in the disk is $M_d = 0.18_{-0.08}^{+1.09} M_\oplus$ for a population of $a_{min} = 0.43 \mu\text{m}$ grains with porosity $p = 70$. The porous grains favored in our modeling agree with previous deductions for debris disks (AU Mic disk; Graham et al., 2007) and was linked to grain growth through agglomeration. As a first order, the effect of porosity is to reduce the effective size of the dust particle with similar scattering properties of smaller solid grains (Graham et al., 2007; Shen et al., 2009).

Our synthetic MCFOST model captures the geometry of the disk well with a combined

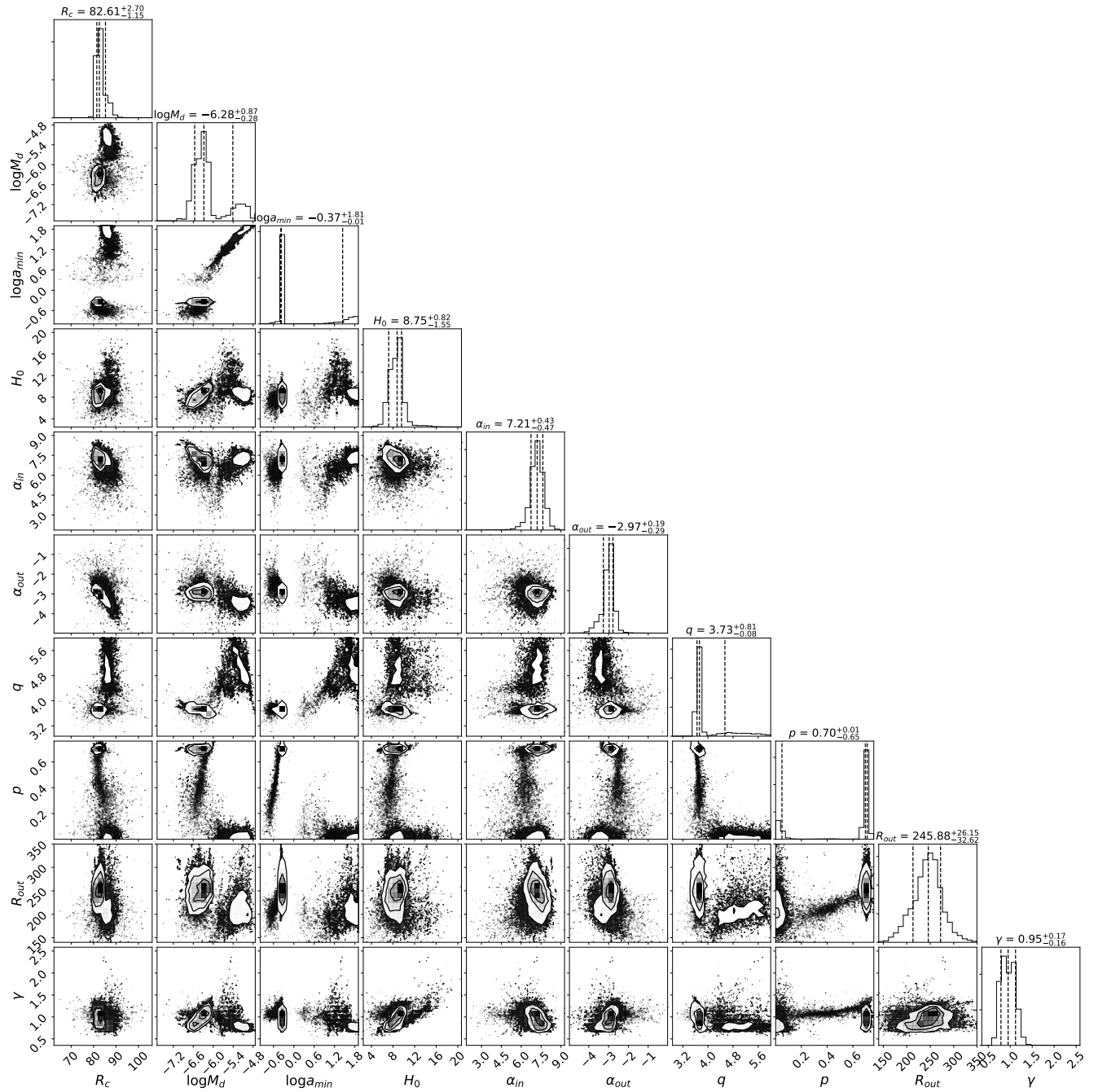


Figure 4.6 Marginalized posterior probability distributions for our MCMC modeling procedure with MCFOST.

$\chi^2_{\text{red}} = 1.16$ and individual $\chi^2_{J\text{red}} = 1.20$, $\chi^2_{H\text{red}} = 1.13$ and $\chi^2_{K1\text{red}} = 1.15$ from the J , H and $K1$ fits respectively. However the morphology of our best-fit model differs from the Stokes Q_r detections with linear polarization values approaching zero towards smaller scattering angles. This effect is clearly represented in the J -band model, achieving negative polarization values

at a scattering angle $\theta_{\text{sca}} \sim 18^\circ$. Negative polarization implies an inversion of the polarization angle at the backscattering region, with polarization vectors pointing in the radial direction. We think that this decrement in linear polarization in our models does not correspond to a real feature of the disk. Instead, our modeling seemingly favors this solution as a consequence of the fitting procedure in a region with large uncertainties next to the FPM. The SNR maps suggest that our modeling is not very sensitive in a small region surrounding the FPM, approximately within $0'.15$ and $PA = 0 - 90$ and thus, more weight is assigned in the fit of other high-SNR regions, particularly towards the ansae of the disk.

4.4.3 A Second Family of Solutions

Unlike the rest of marginalized posteriors in Figure 4.6, the posteriors for M_d , a_{min} , p and q seemingly suggest a bimodality in these distributions. The dust mass M_d and minimum grain size a_{min} are degenerate in optically-thin debris disk as smaller particles, compared to the wavelength of the scattered light, scatter more efficiently. Our modeling thus indicates that a second family of solutions may exist for larger ($\gtrsim 30\mu\text{m}$) and compact (non-porous) grains in a more massive disk. These parameters are degenerate in our modeling, as suggested by their marginalized posteriors in Figure 4.6. We thus select a subset of M_d , a_{min} , p and q drawn around the secondary peaks in the posteriors identified in Section 4.4.2 and test models against data.

Figure 4.7 shows the secondary best-fit in J , H and $K1$ filters in polarized light. This secondary solution captures the front of the disk better at small scattering angles $\theta_{\text{sca}} = 18^\circ \sim 23^\circ$ than smaller grain model. Parameter values for M_d , a_{min} are poorly constrained: $M_d = 3_{-2}^{+3} M_\oplus$, $a_{\text{min}} = 30\mu\text{m} - 70\mu\text{m}$ while there is no strong preference for q in the range $[4 - 6]$. On the other hand, a porosity consistent with zero is strongly preferred. The combined χ_{red}^2 for this solution is 1.19 and it is not statistically different than the $\chi_{\text{red}}^2 = 1.16$ in our best-fit with submicron grains. Although this new model renders the front side of ring better at closer distance to the FPM, the best-fit model with small porous grains still captures the back side of

the disk better, particularly close to the disk ansae.

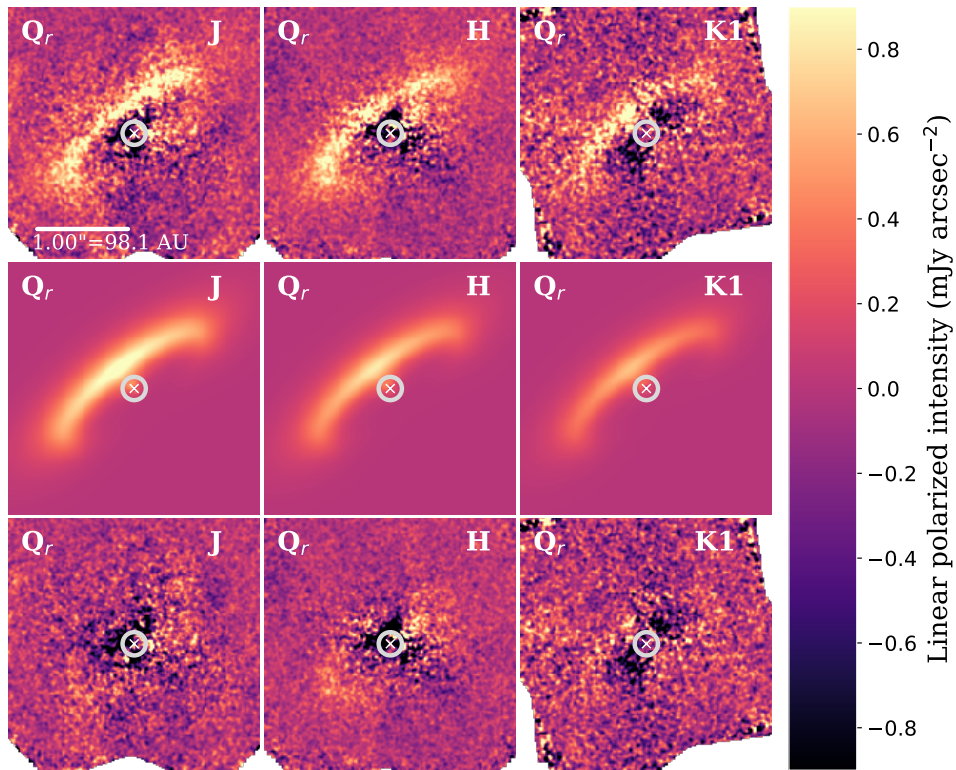


Figure 4.7 *Top*: Observations of HD 157587's disk in *J*, *H* and *K1* bands, *Middle*: images of the secondary best-fit models with ($\sim 30\mu\text{m}$ – $70\mu\text{m}$) grains, : *Bottom* best-fit residuals. Images are displayed on the same colorscale and orientation as Figure 4.1

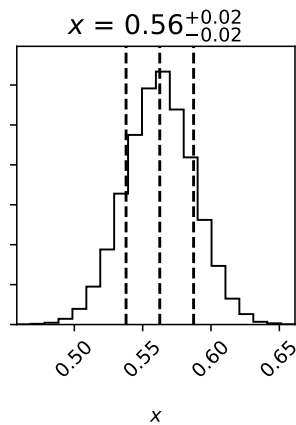


Figure 4.8 Best-fit linear combination parameter x .

We conduct a second test combining the two best-fit solutions and compare it to our data. We define a new model as the linear combination of the two solutions (i.e. the 'small grain' and

'large grain' models) and find the best linear coefficients x (and $1-x$) that fit our observations. We run another instance of the Markov Chain Monte Carlo (MCMC) ensemble sampling package `emcee` with x as a free parameter with 100 single temperature walkers for 1000 iterations. Figure 4.8 shows the posterior probability distribution for x and Figure 4.9 shows the best linear combination model. The best-fit linear coefficient $x = 0.56 \pm 0.02$ and indicates that the 'small grain' model is slightly preferred over larger grains but still consistent with 50%. The combined model offers improvement over the individual models with a $\chi_{\text{red}}^2 = 1.12$.

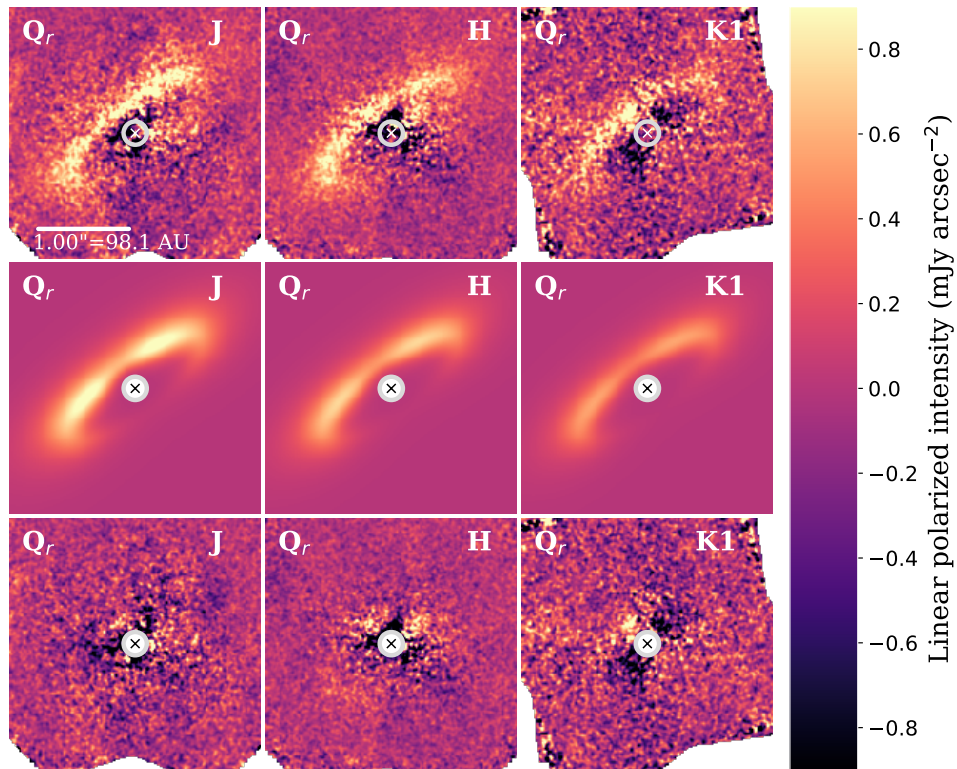


Figure 4.9 Our best linear combination of models. The best model is a linear combination of the best-fit (i.e., 'small grains') model and the second (i.e., 'large grains') model solution. Middle row with models and bottom row shows residuals.

We discuss the morphology of our best-fit model and other possible model solutions further in Section 4.5.2.

4.5 Discussion

4.5.1 Disk Brightness Asymmetries

Our Stokes Q_r detections in J and $K1$ of the NE side of the HD157587 disk confirm the overall ring-shaped morphology reported by [Millar-Blanchaer et al. \(2016\)](#). This strong brightness asymmetry is often interpreted as dust grains scattering light preferentially in the forward direction. The detections at J , H and $K1$ indicate a ring with a steep profile leading to a peak at 83 AU. [Millar-Blanchaer et al. \(2016\)](#) reports a milder secondary brightness asymmetry with the SE half portion of the ring being 15% brighter than the NW half. Such brightness asymmetry can be explained by an stellocentric offset of the disk having a side closer to the star as a result of the presence of a planet in an eccentric orbit ([Wyatt et al., 1999](#)). Our modeling procedure in Section 4.4.1 did not include an stellocentric offset. Therefore our axisymmetric model cannot be used for this test. We instead use the disk photometry maps of the Stokes Q_r detections to quantify this brightness asymmetry between the SE and NW portions of the ring. We combine sectors 2 and 3 in our photometry maps to estimate the flux of the SE portion of the disk. Similarly, sectors 7 and 8 are combined for the NW. This quantifies the flux in two sections towards the disk ansae from which we can compute their ratio. For each filter, we sum the mean fluxes in sectors two and three to compute the total flux of the disk towards the SE. We repeat this procedure on sectors 7 and 8 to compute the total flux for the NW portion of the disk and compute the ratio between SE to the NW sections for each filter. The uncertainties in the selected regions and annuli were propagated and added in quadrature. Our procedure yields SE:NW polarized flux ratios of 1.16 ± 0.04 in H , 1.04 ± 0.04 in J and 1.37 ± 0.13 in $K1$ filters. These estimates further support a disk offset along the projected semimajor axis.

4.5.2 Small and Large Grains

The best model from the simultaneous fit to the Stokes Q_r observations returns an overall good description of the ring. However our models predict negative polarization at small scattering

angles that do not correspond to the observed linear polarization in our observations. Although negative polarization at small scattering angles are feasible for small grains of certain compositions (Shen et al., 2009) it is unclear whether our data shows evidence of this. This discrepancy in our best-fit model taints with uncertainty part of the discussion of certain parameters, namely disk mass M_d , minimum grain size a_{min} , porosity p and the dust grain size distribution index q . The linear combination of the best two models however, reconciles the overall fit to the Stokes Q_r detections with a reduced χ^2 .

The strong asymmetry revealing the eastern side of the disk suggests the detection of a population of small grains. Forward scattering is heavily preferred for grains with size parameter $2\pi a/\lambda \sim$ a few. This corresponds well to the wavelength coverage of our observations in the case of sub-micron grains.

The blow-out radius (Burns et al., 1979) for compact spherical grains in this system is $r_{blow} \sim 0.8\mu\text{m}$ assuming $Q_p = 1$. However, we consider this a lower limit, since porosity increases the effective cross-section of a grain, leading to larger values of r_{blow} . All this indicates that such small grains are short lived becoming analogous to β meteoroids. A halo of dust grains in hyperbolic orbits could populate the outer reaches of the disk seen with HST extending out to ~ 460 AU (Padgett & Stapelfeldt, 2016).

The good agreement of the combined model opens the possibility of two different grain populations coexisting in the disk. Typical dust grain sizes in other disks range from $\sim 0.3\mu\text{m}$ to $\sim 20\mu\text{m}$ from the analysis of images in the optical and NIR and from spectral analysis of silicate features (Graham et al., 2007; Perrin et al., 2015; Mittal et al., 2015; Esposito et al., 2018). The larger grains we derive are above this inferred range but still marginally consistent with the larger 20-30 μm (albeit porous) grains in HR 4796A (Milli et al., 2017). For such large grains, $2\pi a/\lambda \gg 1$ suggesting that scattering operates in the Fresnel regime leading to a strong forward scattering sharply limited to small scattering angles rapidly leveling off at larger θ_{sca} (Perrin et al., 2015). We derive a size distribution index q in the range 4-6 that exceeds the expected value for debris disks from steady collisional models. However values of $q \gtrsim 5$ are

still possible (MacGregor et al., 2016). Measuring polarization fraction curves in each filter would provide better constraints on the minimum grain size and porosity.

4.5.3 A Bright Old Debris Disk

The dust populating debris disk is thought to have originated in belts of minor bodies and planetesimals where a collisional mechanism reduces km-size bodies down to micron-sized grains. The dynamical mechanism behind this involves planets or Mars-sized objects massive enough to stir these km-size objects into more eccentric orbits leading to a higher velocity dispersion and fatal collisions (Wyatt et al., 1999; Kenyon & Bromley, 2008). Radiation pressure and Poynting-Robertson drag should effectively remove this smaller grains over short timescales (Robertson, 1937; Wyatt & Whipple, 1950; Klačka & Kocifaj, 2008). It is thus expected that the mass in small grains should decrease with stellar age leading to fainter disks.

The age estimates for HD 157587 range from 2.2 ± 0.5 Gyrs to $3.0^{+1.7}_{-1.5}$ Gyrs from fits to metallicity, effective temperature and absolute magnitude to evolutionary models (Feltzing et al., 2001; Casagrande et al., 2011). Recently, GAIA DR2 (Gaia Collaboration et al., 2016, 2018) measurements of HD 157587 indicate proper motions of -3.89 ± 0.11 mas yr⁻¹ in right ascension and -31.25 ± 0.076 mas yr⁻¹ in declination with $v_{\text{rad}} = -7.72 \pm 0.65$ km s⁻¹. Applying these recent measurements of stellar coordinates, proper motion, radial velocity and parallax to the BANYAN Σ web tool (Gagné et al., 2018) returns 94% probability that the star is a > 1Gyr old field star and 6% that it is associated with the UCL member group. The higher probability indicates that HD 157587 is likely among a handful of old debris disks resolved in scattered light such as HD 10647. As pointed out in Millar-Blanchaer et al. (2016), HD 10647 is F8V star with a debris ring at ~ 85 AU hosting a Jupiter-mass planet at 2 AU. The debris ring shows a brightness asymmetry in scattered light observations with HST/ACS (Stapelfeldt et al., 2007) and may be linked to a second planet in the system further out (Liseau et al., 2008).

4.6 Conclusion

We have presented follow-up observations of the HD 157587 debris disk with GPI in J and $K1$ polarimetry and GPI spectroscopic observations in $K1$ that complement the first detection at H with GPI PDI by [Millar-Blanchaer et al. \(2016\)](#). Our polarimetric detections confirm the ring-like morphology of the eastern side of an 83 AU optically thin debris disks. The Stokes Q_r detections in the J and $K1$ bands also confirm a milder secondary asymmetry reported by [Millar-Blanchaer et al. \(2016\)](#) that suggests an offset of the disk along its semimajor axis and points to the existence of at least a planetary perturber inside of 83 AU. PDI with GPI outperformed our KLIP+ADI reductions in total intensity revealing in greater detail the morphology of the disk along with its extended features. Our radiative transfer modeling indicates good agreement with a description of a gas-poor dust-rich debris disk. Modeling favors a disk populated by small ($a_{min} = 0.43\mu\text{m}$) porous ($p = 70\%$) grains slightly below the blow out radius for the system. However our modeling also returns a second solution with a disk populated by larger ($\approx 30\mu\text{m}-70\mu\text{m}$) non-porous grains. We find that a linear combination of the best-fit model with this second solution with larger and compact grains improves the overall fit to the data and solves a conspicuous negative polarization at small scattering angles. Recent astrometry from GAIA DR2 narrows down the age estimate of HD 157587, and indicates that it is likely a old field star: among a handful of bright old debris disks.

4.6.1 Acknowledgments

The Gemini Observatory is operated by the Association of Universities for Research in Astronomy, Inc., under a cooperative agreement with the NSF on behalf of the Gemini partnership: the National Science Foundation (United States), the National Research Council (Canada), CONICYT (Chile), the Australian Research Council (Australia), Ministerio da Ciencia, Tecnologia e Inovacao (Brazil), and Ministerio de Ciencia, Tecnologia e Innovacion Productiva (Argentina). This research was supported in part by a Discovery Grant by the Canadian Nat-

ural Sciences and Engineering Council (NSERC) to S.M., and by NSF grant AST-1413718 (GD). P.K. and J.R.G. thank support from NSF AST-1518332, NASA NNX15AC89G and NNX15AD95G/NEXSS. This work benefited from NASAs Nexus for Exoplanet System Science (NExSS) research coordination network sponsored by NASA's Science Mission Directorate. Portions of this work were performed under the auspices of the U.S. Department of Energy by Lawrence Livermore National Laboratory under Contract DE-AC52-07NA27344. This work has made use of data from the European Space Agency (ESA) mission *Gaia* (<https://www.cosmos.esa.int/gaia>), processed by the *Gaia* Data Processing and Analysis Consortium (DPAC, <https://www.cosmos.esa.int/web/gaia/dpac/consortium>). Funding for the DPAC has been provided by national institutions, in particular the institutions participating in the *Gaia* Multilateral Agreement.

Bibliography

Arenou, F., Luri, X., Babusiaux, C., et al. 2017, *A&A*, 599, A50

Bayo, A., Rodrigo, C., Barrado Y Navascués, D., et al. 2008, *A&A*, 492, 277

Beuzit, J.-L., Feldt, M., Dohlen, K., et al. 2008, in *Society of Photo-Optical Instrumentation Engineers (SPIE) Conference Series*, Vol. 7014, *Society of Photo-Optical Instrumentation Engineers (SPIE) Conference Series*, 18

Bruzzone, S., Metchev, S., & Duchene, G. 2019, submitted

Burns, J. A., Lamy, P. L., & Soter, S. 1979, *Icarus*, 40, 1

Canovas, H., Ménard, F., de Boer, J., et al. 2015, *A&A*, 582, L7

Casagrande, L., Schönrich, R., Asplund, M., et al. 2011, *A&A*, 530, A138

Cutri, R. M., Skrutskie, M. F., van Dyk, S., et al. 2003, *VizieR Online Data Catalog*, 2246

- De Rosa, R. J., Nielsen, E. L., Blunt, S. C., et al. 2015, *ApJ*, 814, L3
- Dohnanyi, J. S. 1969, *J. Geophys. Res.*, 74, 2531
- Draine, B. T., & Lee, H. M. 1984, *ApJ*, 285, 89
- Draper, Z. H., Duchêne, G., Millar-Blanchaer, M. A., et al. 2016, *ApJ*, 826, 147
- Esposito, T. M., Fitzgerald, M. P., Graham, J. R., et al. 2016, *AJ*, 152, 85
- Esposito, T. M., Duchêne, G., Kalas, P., et al. 2018, *AJ*, 156, 47
- Feltzing, S., Holmberg, J., & Hurley, J. R. 2001, *A&A*, 377, 911
- Foreman-Mackey, D., Hogg, D. W., Lang, D., & Goodman, J. 2013, *PASP*, 125, 306
- Gagné, J., Mamajek, E. E., Malo, L., et al. 2018, *ApJ*, 856, 23
- Gaia Collaboration, Brown, A. G. A., Vallenari, A., et al. 2018, *ArXiv e-prints*, arXiv:1804.09365
- Gaia Collaboration, Prusti, T., de Bruijne, J. H. J., et al. 2016, *A&A*, 595, A1
- Garufi, A., Benisty, M., Stolker, T., et al. 2017, *The Messenger*, 169, 32
- Graham, J. R., Kalas, P. G., & Matthews, B. C. 2007, *ApJ*, 654, 595
- Grun, E., Zook, H. A., Fechtig, H., & Giese, R. H. 1985, *Icarus*, 62, 244
- Hauschildt, P. H., Allard, F., & Baron, E. 1999, *ApJ*, 512, 377
- Hughes, A. M., Duchene, G., & Matthews, B. 2018, *ArXiv e-prints*, arXiv:1802.04313
- Hung, L.-W., Duchêne, G., Arriaga, P., et al. 2015, *ApJ*, 815, L14
- Hung, L.-W., Bruzzone, S., Millar-Blanchaer, M. A., et al. 2016, *Gemini planet imager observational calibration XII: photometric calibration in the polarimetry mode*, doi:10.1117/12.2233665

- Kalas, P., Graham, J. R., Chiang, E., et al. 2008, *Science*, 322, 1345
- Kenyon, S. J., & Bromley, B. C. 2008, *ApJS*, 179, 451
- Klačka, J., & Kocifaj, M. 2008, *MNRAS*, 390, 1491
- Kurucz, R. 1993, *ATLAS9 Stellar Atmosphere Programs and 2 km/s grid*. Kurucz CD-ROM No. 13. Cambridge, Mass.: Smithsonian Astrophysical Observatory, 1993., 13
- Lagrange, A.-M., Bonnefoy, M., Chauvin, G., et al. 2010, *Science*, 329, 57
- Lebreton, J., Augereau, J.-C., Thi, W.-F., et al. 2012, *A&A*, 539, A17
- Leinert, C., Link, H., Pitz, E., & Giese, R. H. 1976, *A&A*, 47, 221
- Liseau, R., Risacher, C., Brandeker, A., et al. 2008, *A&A*, 480, L47
- MacGregor, M. A., Wilner, D. J., Chandler, C., et al. 2016, *The Astrophysical Journal*, 823, 79
- Macintosh, B., Graham, J. R., Ingraham, P., et al. 2014, *Proceedings of the National Academy of Science*, 111, 12661
- Macintosh, B., Graham, J. R., Barman, T., et al. 2015, *Science*, 350, 64
- Maire, J., Ingraham, P. J., De Rosa, R. J., et al. 2014, in *Society of Photo-Optical Instrumentation Engineers (SPIE) Conference Series*, Vol. 9147, *Society of Photo-Optical Instrumentation Engineers (SPIE) Conference Series*, 85
- Masana, E., Jordi, C., & Ribas, I. 2006, *A&A*, 450, 735
- McDonald, I., Zijlstra, A. A., & Boyer, M. L. 2012, *MNRAS*, 427, 343
- Millar-Blanchaer, M. A., Graham, J. R., Pueyo, L., et al. 2015, *ApJ*, 811, 18
- Millar-Blanchaer, M. A., Wang, J. J., Kalas, P., et al. 2016, *AJ*, 152, 128
- Milli, J., Vigan, A., Mouillet, D., et al. 2017, *A&A*, 599, A108

- Mittal, T., Chen, C. H., Jang-Condell, H., et al. 2015, *ApJ*, 798, 87
- Mukai, T., Ishimoto, H., Kozasa, T., Blum, J., & Greenberg, J. M. 1992, *A&A*, 262, 315
- Padgett, D., & Stapelfeldt, K. 2016, in *IAU Symposium*, Vol. 314, *Young Stars & Planets Near the Sun*, ed. J. H. Kastner, B. Stelzer, & S. A. Metchev, 175–178
- Perrin, M. D., Maire, J., Ingraham, P., et al. 2014, in *Proc. SPIE*, Vol. 9147, *Ground-based and Airborne Instrumentation for Astronomy V*, 91473J
- Perrin, M. D., Duchene, G., Millar-Blanchaer, M., et al. 2015, *ApJ*, 799, 182
- Pinte, C., Harries, T. J., Min, M., et al. 2009, *A&A*, 498, 967
- Pinte, C., Ménard, F., Duchêne, G., & Bastien, P. 2006, *A&A*, 459, 797
- Pueyo, L., Soummer, R., Hoffmann, J., et al. 2015, *ApJ*, 803, 31
- Robertson, H. P. 1937, *MNRAS*, 97, 423
- Schmid, H. M., Joos, F., & Tschan, D. 2006, *A&A*, 452, 657
- Shen, Y., Draine, B. T., & Johnson, E. T. 2009, *ApJ*, 696, 2126
- Sivaramakrishnan, A., & Oppenheimer, B. R. 2006, *ApJ*, 647, 620
- Soummer, R., Pueyo, L., & Larkin, J. 2012, *ApJ*, 755, L28
- Stapelfeldt, K., Krist, J., Bryden, G., & Chen, C. 2007, in *In the Spirit of Bernard Lyot: The Direct Detection of Planets and Circumstellar Disks in the 21st Century*
- Wang, J. J., Ruffio, J.-B., De Rosa, R. J., et al. 2015, *pyKLIP: PSF Subtraction for Exoplanets and Disks*, *Astrophysics Source Code Library*
- Wang, J. J., Rajan, A., Graham, J. R., et al. 2014, in *Proc. SPIE*, Vol. 9147, *Ground-based and Airborne Instrumentation for Astronomy V*, 914755

Wyatt, M. C., Dermott, S. F., Telesco, C. M., et al. 1999, *ApJ*, 527, 918

Wyatt, S. P., & Whipple, F. L. 1950, *ApJ*, 111, 134

Chapter 5

Conclusions.

Debris disks are gas-poor disks that show evidence of ongoing dust production. These dust-rich disks comprise second-generation dust which arises from destructive collisions of planetesimals and as the decay products of asteroids and comets. Up to a certain extent, currently observed debris disk can be regarded as massive analogs to the population of small icy bodies of the Solar System. The observed morphologies of these debris disks such as warps, spirals, gaps, offsets and asymmetries, suggest the presence of hidden planets and provide useful constraints to models of planet-disk interactions.

Direct imaging of faint debris disks represents a challenge as high-angular resolution and high-contrast instruments are needed. Current instrumental limitations dictate that very bright nearby stars (< 200 pc) are usually the best candidates for coronagraphic scattered-light observations in the near-IR. This arises as a prerequisite for AO performance and for probing closer to the star with a sufficiently small IWA. However, most debris disks are a few orders of magnitude fainter than their host stars and this is a major obstacle preventing their detection. The undesired residual light surrounding the central star in AO systems, often referred as speckles, creates a bright halo that buries any faint contribution from circumstellar material. Solutions for PSF subtraction such as KLIP+ADI or LOCI are usually effective in removing the bright stellar halo and revealing faint stellar companions. However, such techniques are

often ineffective in recovering extended sources like disks. PDI with the GPI offers an efficient way to suppress the residual starlight dramatically improving the contrast performance of the instrument. Starlight is usually not polarized as individual photons undergo multiple scattering events as they leave the stellar photosphere. However, once these randomly polarized photons are scattered by dust grains in an optically thin medium, they become linearly polarized. This is key for achieving high-contrast observations as polarimeters can effectively separate the polarized component of the scattered light. In addition, polarimetry allows us to infer dust grain properties such as grain size and porosity in debris disks. This helps to study grain growth as grains bigger than the grains found in the interstellar medium are expected to populate these dusty disks.

For decades, the birth of planetary systems has been a topic of extensive research in the astronomical community. With the advances gained in high-angular resolution capabilities, the community focused on characterizing newly resolved disks and studied them as snapshots of the planetary formation process. The characterization of debris disks in scattered light is important as they represent windows into the early stages of planetary systems, right after the gas is removed and at the time where young gas giants and planetary embryos form. One of the big questions of the field is how planets and dusty disks interact, specially at a time where the gas content diminished significantly. Fomalhaut and β Pictoris are the only examples where a planet has been detected interacting with a debris disk. By expanding the number of resolved debris disk we increase statistics on disk morphologies and as a result provide upper limits of planetary masses.

Debris disks are also the closest analogues to our Solar System with ring-shaped structures reminiscent of the Kuiper and Main Asteroid Belts. By combining the power of high-angular resolution scattered-light PDI observations and thermal emission maps of debris disks we can bring a clearer picture of the dust architecture in these systems. This allows us to trace two dust populations and separate them into a cold debris and warm zodiacal cloud component. By modeling debris disk images in scattered light and their thermal emission we reveal how

ubiquitous these two dust populations are and how they compare to the dust in the Solar System.

This thesis has presented a comprehensive approach to characterize the morphology of debris disk with GPI and it is thus a valuable contribution to the debris disks community. The work comprising chapter 2 has provided the GPI community with a way to flux-calibrate data taken in polarimetry mode with this instrument. It also characterized the instrument in polarimetry mode revealing unknown biases in the GPI DRP. Chapters 3 and 4 laid down the steps to fully characterize the morphology of two debris disks taking full advantage of PDI to reveal the faint emission of such dusty objects. In the study of HD 141569A, this thesis has revealed the first detection in polarized light with GPI PDI and highlights the power of polarization as an effective tool to achieve high-contrast detections of dusty disks. Chapter 3 also contributes with the first report of an spiral arm within 50 AU that may signal the presence of an unseen planet. In addition, this thesis presents the highest SNR detection of the multi-ringed structure of the HD 141569A to date. Chapters 3 and 4 also showed the powerful synergy between PDI and ray-tracing modeling with MCFOST to map and reproduce disk morphologies. The work included in Chapters 3 and 4 is applicable to other existing debris disks detections with GPI and it is an excellent example to expand the taxonomy of debris disk by mapping their structures at extreme-contrast.

The following sections provide a summary of the work presented in this thesis and includes a brief outline of future steps.

5.1 Thesis Summary

- The ability to secure calibrated fluxes in high-contrast high-angular resolution observations of debris disks is fundamental to debris disk characterization. In my first project, I presented a new method to perform the photometric calibration of coronagraphic observations with GPI in polarimetry mode. I developed a primitive in the GPI DRP to measure the stellar flux by performing aperture photometry of GPI's four fiducial spots.

The primitive relies on the satellite spot geometry and orientation inferred from GPI's apodizer in the H band. The calibration uses the known satellite:star flux ratio, the stellar flux and the average satellite flux. The method is used to photometrically calibrate the H -band polarimetric observations of HD 19467 B and β Pic b. The consistency between our calibrated fluxes and the literature values indicates the reliability of the procedure. Finally, an alternative photometric calibration method is performed by scaling the polarimetric observations to the calibrated observations in spectroscopy mode. With this procedure, I was able to show that polarimetric observations with GPI are on average 3% brighter than in spectroscopy mode.

- PDI with GPI has proven to be an effective tool to reveal fine details of debris disk when other techniques struggle to do so. In the study of the HD 141569A system, I presented the first polarimetric detection of the inner 44 AU disk component in polarimetry. H -band PDI with GPI has revealed the highest SNR detection of this inner ring-shaped disk inwards to $0''.25$ and supersedes other detections with contemporary high-contrast high-resolution instruments. This high SNR detection shows a disk described radially with a combination of two power laws that peaks at 44 AU and extends out to 100 AU. Polarimetry reveals the east side of the disk and independently indicates an optically thin circumstellar medium. The circumstellar environment indicates macroscopic polarization of photons that experience single scattering events. The east side of the middle 200 AU ring is also detected and puts into perspective the small IWA achieved with GPI. The high-contrast and high-angular resolution of PDI reveals an arc-like overdensity that is reminiscent of spiral arm structures previously known at larger spatial scales in this system. With flux-calibrated PDI observations, we apply radiative transfer modeling to explore disk parameters and predict the thermal emission of the disk. This enables to rule out the presence of a significant population of sub-micron grains by the lack of negative signal in the H -band Stokes Q_r image. We estimate the amount of unseen dust inwards of 28 AU by comparing the predicted SED against a catalog of existed photometry of

HD 141569A. We find that a 5–15 AU belt likely exists interior to the observed 44 AU ring to fully reproduce the 8–30 μm SED. The multi-ring structure of the disk with its arc-like structures provides new insights for models of planet-disk interactions. PDI with GPI has revealed the richness of the circumstellar environment in unprecedented detail.

- For the third project, I performed a follow-up study of the HD 157587 debris disk with GPI PDI including observations in the J and $K1$ bands. The study incorporates archival H -band data with GPI PDI covering the 1.24 μm –2.05 μm range of the NIR. I confirmed the ring-like morphology of the eastern side of a 83 AU optically-thin debris disk detected in H band. PDI with GPI outperformed our KLIP+ADI reductions in total intensity and revealed extended details of the disk. This highlights a current obstacle in debris disk characterization as it is often difficult to simultaneously retrieve a robust detection in total intensity. The dependence of polarization fraction with scattering angle requires detecting the disk in total intensity in a wide range of scattering angles and thus limits the power of using polarimetry to probe dust grain size and porosity. Our Stokes Q_r detections in the J and $K1$ bands also confirms a mild secondary asymmetry along the disk semimajor axis reported in the H band with GPI PDI. Measuring this asymmetry in three bands supports an offset of the disk along its semimajor axis and may indicate the existence of a planetary perturber inside of 83 AU. Our flux-calibrated detections enabled radiative transfer modeling to simultaneously fit the three detections and show good agreement with a description of a gas-poor dust-rich debris disk. Our modeling indicated that a two-model solution is likely needed to better describe the disk, with a disk populated by a first population of small ($a_{min} = 0.43\mu\text{m}$), porous ($p = 70\%$) grains and a second population of $\sim 30\mu\text{m} - 70\mu\text{m}$ compact grains. I included recent astrometry from GAIA DR2 which suggest an age for HD 157587 likely above 1Gyr based on its proper motion. This places HD 157587 among a handful of bright old debris disks with strong evidence of ongoing dust production in the system.

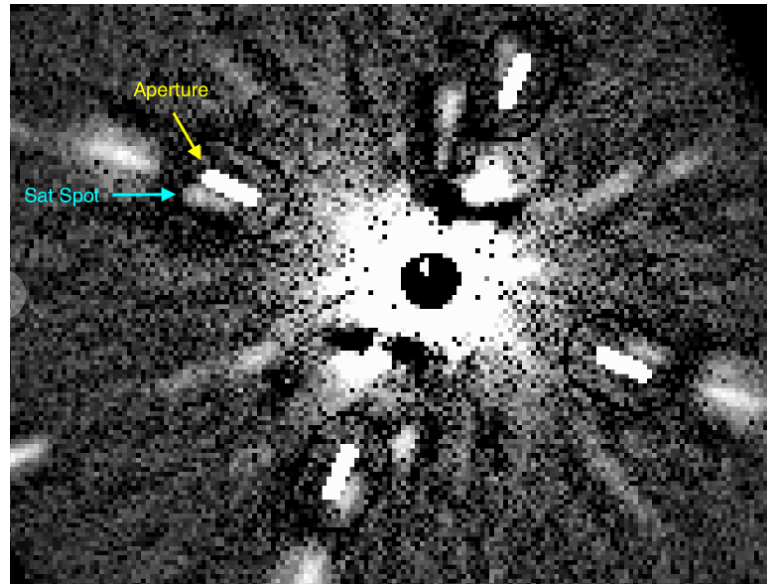


Figure 5.1 Comparison of satellite spot aperture positions for the H -band apodizer at J with the J -band apodizer. The apertures are displaced from the true satellite spot positions and will return erroneous flux measurements (Thomas Esposito, personal communication).

5.2 Future Work

5.2.1 Photometric Calibration of GPI in the J and $K1$ bands in Polarimetry Mode

The debris disk LLP extended the set of observed disks with GPI with observations at J and $K1$. The photometric calibration presented in the first project relies on the satellite spot geometry and orientation derived for the H -band apodizer (e.g. the satellite spot distance from the star is λ/d where d is the wire spacing in the apodizer). Attempting to measure satellite spot fluxes in polarimetry mode in the J and $K1$ bands will return erroneous measurements as the photometry apertures will appear displaced away from the true position of the satellite spots. Figure 5.1 shows this effect when running the primitive to measure satellite spot fluxes on non H -band apodizer observations in polarimetry mode. I am contributing to efforts to improve satellite spot flux measurements, led by GPIES collaborator Thomas Esposito with a new version of the primitive. This will enable further testing of satellite spot flux variability at all bands in

polarimetry mode and will allow to flux calibrate a larger set of disk observations.

5.2.2 Debris Disk Observations

In this thesis we have shown the difficulty to simultaneously detect debris disks in polarized light and in total intensity. It represents an obstacle for probing dust grain properties through their polarization dependence on scattering angle. Our study of HD 157587 has shown how the disk is recovered in polarized light at J , H and $K1$ and highlights the utility of securing multi-band polarimetric observations. Future work could include fitting simultaneously few different grain compositions (ices, silicates, magnesium-rich olivines) to multi-band observations in polarimetry mode as a tool to probe the behavior of different dust grain composition with wavelength. In 3-4 years GPI will be moved to the Gemini North telescope, and will so allow an extension of the present work to northern debris disks. Relocating the instrument to a new observatory would require time to understand the systematics of observations and could delay the first light of the instrument in the north. The GPI survey suffered from bad weather and systematic strong winds that limited contrast quality and observing time. Structural vibrations induced by winds are known to have aborted numerous observing sequences. With the lessons learned over the past four years of operations and new instrument upgrades, like an improved wavefront sensor detector, the disk survey will benefit from greater instrument sensitivity and a higher disk detection rate, and result in new exciting discoveries

Appendix A

Appendix.

In this study we characterize the photometric response and throughput of GPI in polarimetry mode in H-band to calibrate the photometric response in this observing mode. To do so, we compare total H-band satellite spot fluxes using laboratory data, on-sky observations and flat fields in spectral and polarimetry mode. Due to the current observing strategy, most of the targets suitable for this study are taken after a long sequence in spectral mode and include between 5 and 8 polarimetry-mode snapshots. Persistence is known to be relevant after long sequences and in some cases, steps were taken to mitigate its effects. Independently, flat frames in polarimetry and spectroscopy were acquired to study the throughput in these observing modes. In Section [A.1](#) we describe the methods. Section [A.2](#) includes the results with the analysis of the satellite spot fluxes in [A.2.1](#) and in [A.2.2](#) the study of the GCAL flats. The satellite spot flux variability is presented in [A.2.2](#), arriving to the conclusions in Section [A.3](#).

A.1 Methodology

All science observations were reduced with GPI Data Reduction Pipeline (hereafter DRP) v1.3 rev4105M. Spectroscopy data were reduced with the `Calibrated Datacube Extraction` recipe excluding the `Calibrate Photometric Flux` primitive since we are interested in comparing fluxes in $\text{ADU coadd}^{-1} \text{ s}^{-1}$. In this step, we manually retrieved all the calibra-

tion arcs taken prior to each sequence to generate wavelength solutions as input to the `Update Shift for Flexure` primitive. Polarimetry podc cubes were created with the `Simple Polarization Datacube Extraction` recipe with the `PSF` and `BOX` extraction algorithms. Here, `OLD` and `NEW` were the two methods for bad pixel interpolation in datacubes used. As before, all calibrations files were inspected and the shifts computed for flexure were inspected for errors while Darks with persistence were removed as well.

We used the default method of datacube extraction in spectroscopy mode which integrates the signal over a rectangular 1×3 pixel aperture centered on the spectrum, and repeated for each pixel along the dispersion axis. The dimensions of this rectangular aperture were chosen to integrate the maximum number of pixels of the micro-lens PSF and small enough to mitigate contamination from wings of neighboring spectra. Once all the spectra are individually extracted, they are interpolated onto a common wavelength axis to create the datacube. On the other hand, two methods of datacube extraction in polarimetry mode were used in this study. The first method to extract the datacubes (`BOX`) implements a 5×5 box centered at each polarimetry spot while the second method (`PSF`) uses empirically calibrated subpixel lenslet PSFs. In addition to these methods, GPI DRP offers two procedures for bad pixel interpolation in datacubes in polarimetry mode: `OLD` and `NEW`. We compare how the `BOX` and `PSF` method perform in [A.2.1](#). Then we compare the two methods for bad pixel interpolation in polarimetry cubes in [A.2.1](#) as implemented with `PSF`.

The reduced spdc and podc cubes were collapsed to retrieve the total flux in H-band in both observing modes. In this process, satellite spots become smeared with a streak-like appearance pointing radially out of the central occulted star. This represents a problem since the satellite spot positions and morphology need to be addressed to properly define the best shape to use in aperture photometry. Here we describe how to define the locations of the satellite spots in polarimetry mode. The spaces between the wires in the grid imprinted on GPI's apodizer can be used to find the radial position of the satellite spots. With the wire spacing d , we can locate the

fiducial satellite spots relative to the occulter at λ/d , with λ the wavelength. This allows us to define the characteristic length of the smeared spots in the desired range in wavelengths. Then the azimuthal position of the satellite spots was determined using a collection of the observed targets to provide the mean angular positions. With this and the position of the occulted star we were able to also define the position of the smeared satellite spots in polarimetry mode. To define the satellite spot positions in spectroscopy mode we proceeded as follows. The positions of the smeared satellite spots in spectral mode were computed retrieving the satellite spot positions at slice 18 using the `Measure Satellite Spot Location` primitive. Then using the same characteristic length as in pol mode, we can address the location of the streaks. As a quality check, the locations of the smeared spots were compared and both methods agree within less than 0.5 pixels on average.

To handle this and other operations a primitive was developed in the DRP to measure the smeared satellite spot fluxes in polarimetry and spectroscopy mode. To retrieve the satellite spot fluxes we performed aperture photometry with an elongated aperture as illustrated in Figure A.1. The aperture consists of a rectangle capped with semi-circles on either end along the longest axis of the rectangle. The length of the rectangle is defined by the satellite spot positions at the minimum and maximum wavelength in H band and corresponds to 12 pixels. Two sets of aperture values were selected in this study. In the first set, a radius 4 pixels was chosen to measure the satellite spot fluxes, a value slightly greater than the FWHM of the satellite spots in spectral mode. To measure sky values, we use a region around the aperture that resembles a *racetrack* with inner and outer radii for the racetrack region at 6 and 9 pixels respectively. The second set included [5,8,12] as the radii to measure satellite spot fluxes and sky levels respectively. The average FWHM of the satellite spots at slice 18 is 3.7 pixels for the observed targets, and 3.9 pixels in laboratory data.

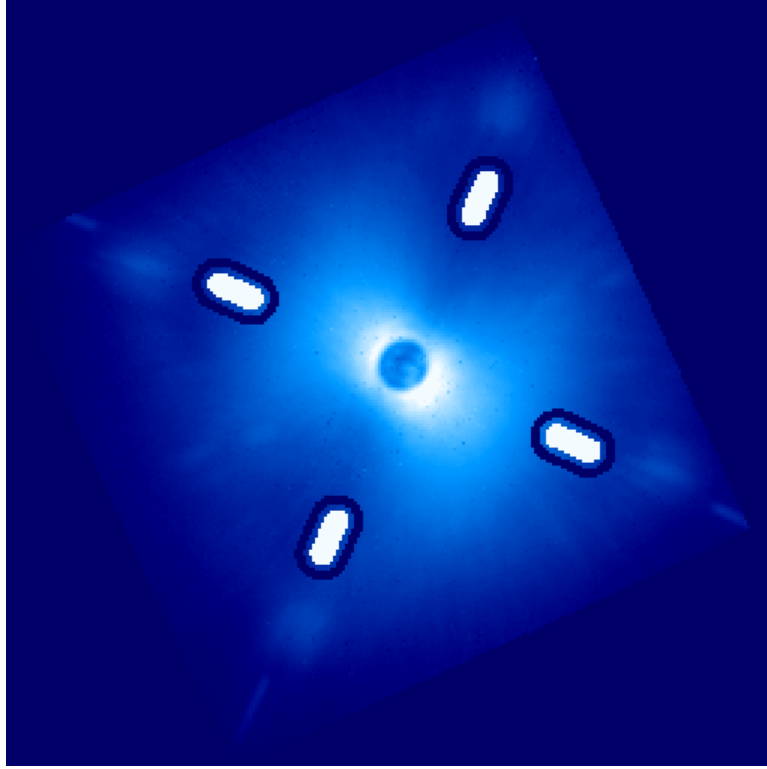


Figure A.1 49 Cet in polarimetry mode with apertures for source (white) and sky (dark blue) used to measure satellite fluxes. The elongated aperture used is a 8×12 rectangle capped by $r=4$ semi-circles on either end.

The satellite spot flux uncertainties calculated in this primitive were derived following Equation A.1

$$\sigma^2 = \frac{1}{g} \frac{\sum_{i=1}^{N_A} s_i - N_A \bar{B}}{N_i} + \left(N_A + \frac{N_A^2}{N_B} \right) \sigma_B^2 \quad (\text{A.1})$$

Where g is the system gain of $3.04 \text{ e}^{-1} \text{ ADU}^{-1}$, N_A the pixels used in the aperture for source estimation, \bar{B} the median sky value, N_B number of pixels used for sky estimation, σ_B^2 is the sky variance and N_i the number of coadds. A detailed explanation of this equation can be found at [Uncertainties in Aperture Photometry by F. Masci, 2008](#). However we note that the flux uncertainties in this study are derived from the standard deviation of the measurements and represent the scatter of the data.

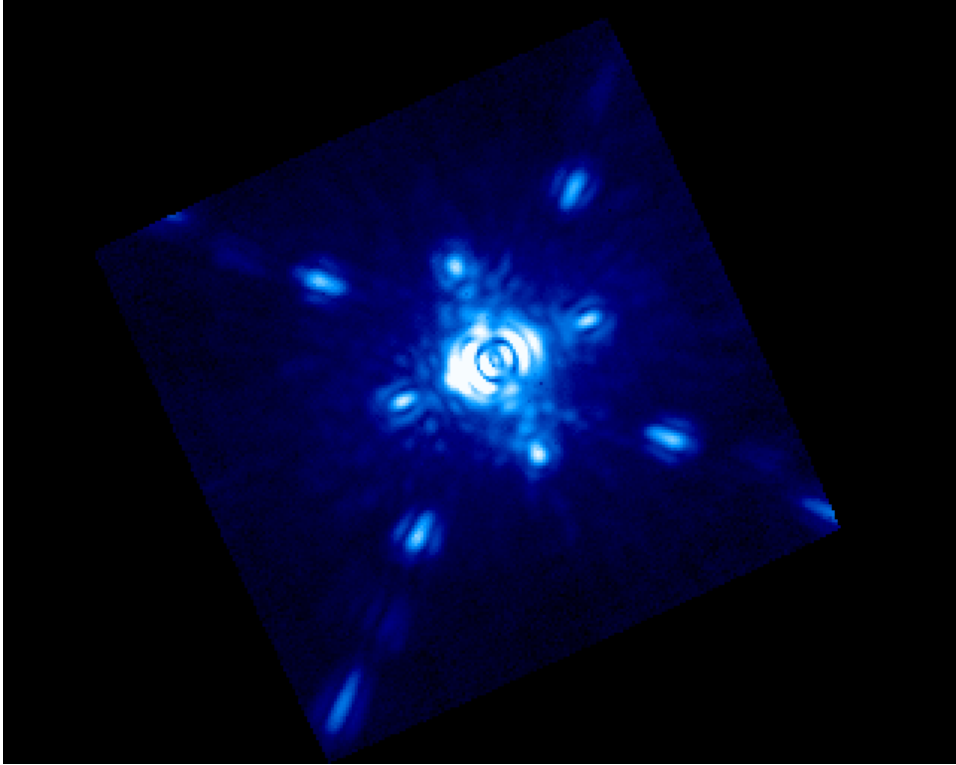


Figure A.2 Reduced podc cube from the laboratory. The injected spots were added closer to the occulted artificial source.

The primitive was used to measure satellite spot fluxes with their uncertainties along with the flux of the companions. For each target, the total satellite flux was measured in each image in spectroscopy and polarimetry mode and the mean of each observing sequence calculated. This procedure returns the mean total satellite spot flux in spectroscopy and the mean total satellite spot flux in polarimetry mode for each target, along with the standard deviation for each sequence. With the means, a pol:spec ratio is recorded and its uncertainty comes from error propagation. In the special case of HIP 70931 and HD 19467, we use APER to retrieve the companion fluxes and its uncertainty. We note however that the uncertainties used here were based on the standard deviation of the measurements.

A.2 Results

A.2.1 Satellite Spot and Companion pol:spec total flux ratios

BOX and PSF

As noted before, BOX and PSF are the two methods available to assemble the podc cubes in GPI DRP. We inspected the total satellite spot fluxes in polarimetry mode as measured on the reduced podc cubes following these two extraction algorithms. Here, we used OLD as the bad pixel interpolation method in polarimetry cubes. We investigate the effects of using the OLD and NEW method in A.2.1. Table A.1 shows the pol:spec ratio of the total satellite spot flux as derived with the BOX and PSF extraction algorithms, where we adopted [4, 6, 9] as the aperture photometry radius, inner and outer sky radii respectively.

A systematic increase in flux is observed when using the 5×5 box extraction algorithm instead of the PSF method with no significant effect on the scatter of the data. This is due perhaps to more flux being measured within the 5×5 box. Although this increment in flux varies from target to target, the weighted averages of the pol:spec ratio of the total satellite spot flux is 1.02 ± 0.02 and 1.14 ± 0.02 for the PSF and BOX algorithms respectively. This suggests an average increase of $\sim 12\%$ in polarimetry flux across all targets as summarized in Table A.1. Interestingly, the PSF algorithm for HIP 70931 yields a satellite spot: companion ratio of the pol:spec ratios of one, indicating the validity of the procedure. However, for HD 19467 the same ratio of ratios is 0.92, perhaps because the companion is faint. The same ratio from BOX for HD 19467 is closer to unity whereby for HIP 70931 the same comparison yields 0.97 as observed in January 2015. We note however, that comparing satellite spot fluxes with companion fluxes is not straightforward as a proper account of the systematics involved is needed. We are comparing fluxes using different aperture sizes and shapes. Moreover, HIP 70931B is much brighter compared to the satellite spots.

Laboratory measurements were performed on Sept 2014 and in this sequence, four extra spots were injected into the image by injecting sine waves into the deformable mirror. Figure [A.2](#) shows a laboratory podc cube. Looking at the laboratory data, the pol:spec ratio of the total satellite flux does not agree with the science targets with neither algorithm. It is worth noting that BOX returns a satellite spot: injected spot ratio of the pol:spec ratios of one while with PSF the same test fails miserably. We don't understand what is behind such discrepancies and will focus on the pol:spec ratio of the total satellite spot fluxes for the science targets from now on. We think nevertheless that different background extraction procedures should be tested to help expand the scope of this analysis.

The higher pol:spec ratios of the total satellite spot fluxes from BOX look suspicious as such a great difference in flux is not expected for GPI. The smaller pol:spec ratios from PSF seem reasonable, therefore we adopt the latter in this study.

Pol:Spec ratios

Table [A.2](#) summarizes the results of the pol:spec ratio of the total satellite flux for the two sets of aperture values used, [4,6,9] and [5,8,12]. Also included is the pol:spec ratio of the total flux of HIP 70931B and HD 19467B and the pol:spec ratio of the total flux of the injected satellite spots in the laboratory. CNTRD was used to locate the centroid of the companions and aperture photometry was performed with APER with an aperture of 10 and 4 pixels for HIP 70931B and HD 19467B respectively. For the faint HD 19467B, an aperture of 4 pixels was used. All centroids were manually inspected for offsets. Figure [A.3](#) shows the total flux of HIP 70931B in March 2014 and January 2015. We did not correct for airmass due to the short duration of the sequences.

The apertures chosen yield a slightly different pol:spec ratio of the total satellite spot flux. With an aperture of 4 pix we arrive at a weighted average of the pol:spec ratio of the total satellite flux of 1.02 ± 0.02 . Similarly, an aperture of 5 pixels yields a weighted average of 1.04

Name	H (mag)	Ratio (PSF)	σ	Ratio (BOX)	σ
49 Cet	5.5	1.11	0.09	1.25	0.10
ϵ Eri	1.75	1.09	0.09	1.17	0.09
V435 Car	6.3	0.99	0.05	1.08	0.05
HD31392	5.8	1.10	0.13	1.19	0.13
γ Dor	3.5	1.11	0.26	1.20	0.28
γ Ophi	3.6	1.09	0.07	1.17	0.07
HD74576	4.4	1.05	0.09	1.15	0.08
HR 826	5.6	0.97	0.11	1.05	0.12
HR 6948	5.3	1.05	0.10	1.13	0.10
HD 19467	5.44	0.98	0.05	1.12	0.05
HD 19467B	17.9	1.07	0.43	1.14	0.43
HIP70931 ³	5.3	1.07	0.08	1.12	0.14
HIP70931 ^{4*}	5.3	1.02	0.06	1.11	0.09
HIP70931B ³		1.06	0.02	1.13	0.02
HIP70931B ⁴		1.02	0.01	1.15	0.02
LAB	-	0.93	0.01	1.22	0.06
LAB Injected Spots	-	1.07	0.03	1.22	0.05

Table A.1: Science targets and laboratory observations with GPI in polarimetry and spectroscopy mode. Total pol:spec ratios of the total satellite spot fluxes with σ as the standard deviation of the measurements. We included values retrieved from the two extraction algorithm available in polarimetry mode, BOX and PSF

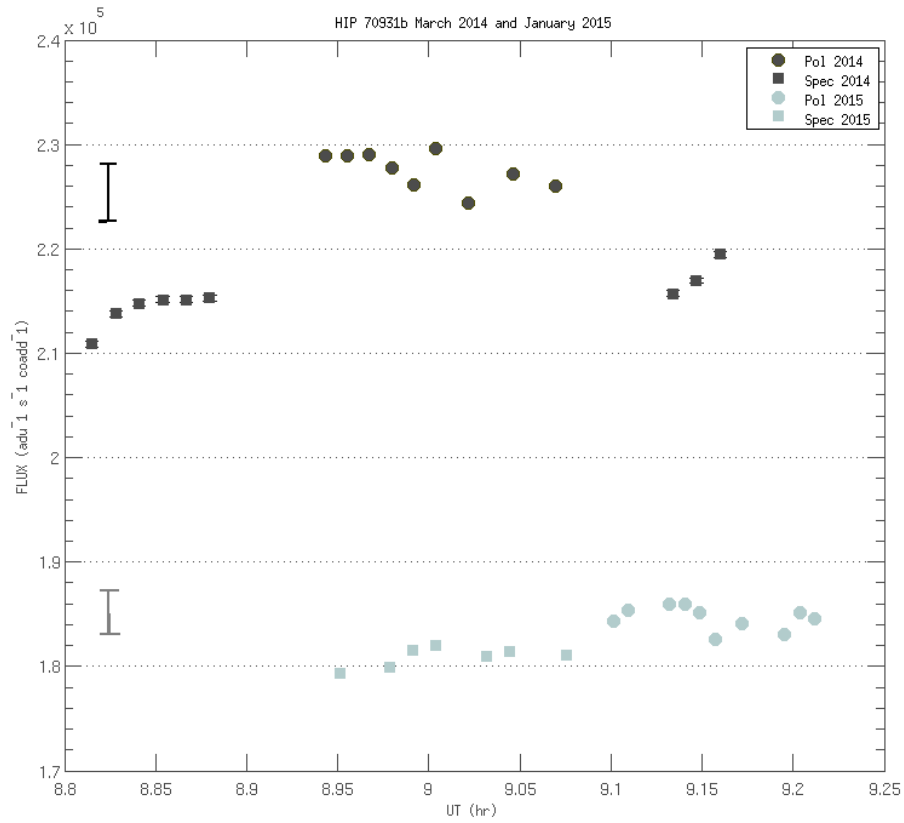


Figure A.3 Total flux variability of HIP 70931b in March 2014 and January 2015. The dark error bar indicates the standard deviation in polarimetry flux in March 2014 on the top left, and on the bottom left, the gray error bar shows the standard deviation in polarimetry in January 2015.

Name	H (mag)	Elevation ¹	Elevation ²	ITIME ¹	ITIME ²	Ratio (PSF) ^a	σ^a	Ratio (PSF) ^b	σ^b	#obs
49 Cet	5.5	74.8°	73.7°	59.6	59.6	1.11	0.09	1.06	0.14	17
ϵ Eri	1.75	66.4°	65.78°	14.5*4	1.5*13	1.09	0.09	1.05	0.14	7
V435 Car	6.3	69°	68.77°	59.64	29.1*2	0.99	0.05	1.03	0.08	8
HD31392	5.8	78.4°	77°	59.64	29.1*2	1.10	0.13	1.04	0.10	8
γ Dor	3.5	66°	65.4°	59.64	4.4*8	1.11	0.26	1.09	0.20	7
γ Ophi	3.6	51°	49.6°	59.64	4.4*8	1.09	0.07	1.08	0.05	12
HD74576	4.4	78°	76.3°	59.64	29.1*2	1.05	0.09	1.04	0.08	4
HR 826	5.6	79°	77.2°	59.64	59.64	0.97	0.11	0.92	0.13	6
HR 6948	5.3	80°	74°	59.64	29.10*2	1.05	0.10	1.06	0.12	10
HD 19467	5.44	57.2°	56.1°	119.29	59.64	0.98	0.05	0.97	0.06	10
HD 19467B	17.9	57.2°	56.1°	119.29	59.64	1.07	0.43	-	-	10
HIP70931 ³	5.3	62.7°	62°	29.09	4.4*4	1.07	0.08	1.18	0.17	5
HIP70931 ^{4*}	5.3	62.5°	63.7°	29.09	14.5*4	1.02	0.06	-	-	8
HIP70931B ³		62.7°	62°	29.09	4.4*4	1.06	0.02	-	-	5
HIP70931B ⁴		62.5°	63.7°	29.09	14.5*4	1.02	0.01	-	-	8
LAB	-	-	-	59.64	8.78	0.93	0.01	0.94	0.01	3
LAB Injected Spots	-	-	-	59.64	8.78	1.07	0.03	1.08	0.03	3

Table A.2: Science targets observed with GPI in polarimetry and spectroscopy mode. Total pol:spec satellite flux ratio with σ as the standard deviation of the measurements.

^a Fluxes with [4,6,9] as the aperture settings

^b Fluxes with [5,8,12] as the aperture settings

¹ Spectroscopic and ² polarimetric observations.

³ HIP70931 observed in March 2014 and

⁴ in HIP70931 Jan 2015. The podc cubes were assembled with the PSF extraction algorithm.

^{4*} Three satellite spots were used instead of four.

± 0.03 . Although both results are consistent, they differ from what is observed using laboratory measurements and the source of this discrepancy is unknown.

However, we can independently derive the pol:spec ratio of the total flux of the bright companion HIP 70931B. Using the flux of HIP 70931B in polarimetry and spectroscopy we compute a weighted average of the total flux ratios of 1.03 ± 0.01 . Being able to constrain the mean pol:spec ratio within 1%, covering the range of the weighted means for the satellite spots found before, gives us confidence of how well we can assess the uncertainties, random and systematic in our calibration. Therefore we compute the weighted average of the pol:spec ratio of the total satellite spot fluxes found before to arrive at a weighted average of the pol:spec ratio of the total satellite spot flux of 1.03 ± 0.01 . The uncertainty here represents the scatter of the data including systematic errors.

Figure A.4 shows the mean total satellite spot flux as a function of H magnitude in polarimetry and spectroscopy mode for the targets in this study. We fitted a simple relation $flux = 10^{-0.4(H+const)}$ to the data with weights in both observing modes. This yields $const = -15.13 \pm 0.10$ in polarimetry and $const = -15.13 \pm 0.07$ in spectroscopy mode within a 95% confidence interval.

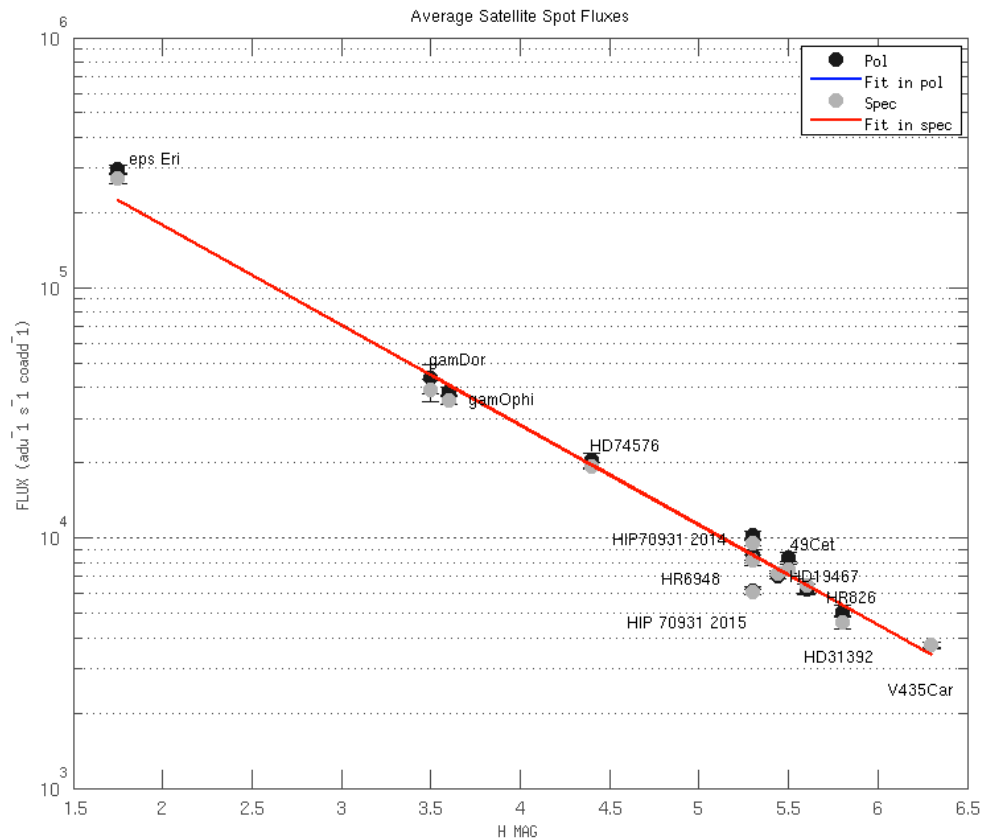


Figure A.4 Average total satellite spot flux as a function of H magnitude with an aperture of 4 pixels in spectroscopy (light gray) and polarimetry (black) dots. The weighted fit to the data follows the expected relation between fluxes and magnitudes. Both fits are virtually identical.

Name	H (mag)	Ratio (OLD Method)	σ	Ratio (NEW Method)	σ
49 Cet	5.5	1.11	0.09	1.12	0.10
ϵ Eri	1.75	1.09	0.09	1.10	0.09
V435 Car	6.3	0.99	0.05	1.00	0.05
HD31392	5.8	1.10	0.13	1.10	0.13
γ Dor	3.5	1.11	0.26	1.12	0.27
γ Ophi	3.6	1.09	0.07	1.09	0.08
HD74576	4.4	1.05	0.09	1.06	0.09
HR 826	5.6	0.97	0.11	0.97	0.11
HR 6948	5.3	1.05	0.10	1.05	0.10
HD 19467	5.44	0.98	0.05	0.98	0.05
HD 19467B	17.9	1.07	0.43	1.06	0.41
HIP70931 ³	5.3	1.07	0.08	1.08	0.10
HIP70931 ^{4*}	5.3	1.02	0.06	1.01	0.09
HIP70931B ³		1.06	0.02	0.96	0.03
HIP70931B ⁴		1.02	0.01	0.99	0.03
LAB	-	0.93	0.01	0.88	0.05
LAB Injected Spots	-	1.07	0.03	1.01	0.05

Table A.3: Science targets and laboratory observations with GPI in polarimetry and spectroscopy mode. Total pol:spec ratios of the total satellite spot fluxes with σ as the standard deviation of the measurements. We include values retrieved using the two methods available for bad pixel interpolation in polarimetry datacubes: OLD and NEW, available in polarimetry mode.

Interpolating Bad Pixels in Cube: OLD and NEW Methods

There are two methods for bad pixel interpolation in polarimetry datacubes available when reducing polarimetry data, OLD and NEW. Up to this point, we used the OLD method for bad pixel interpolation in datacubes in polarimetry. The current version of GPI DRP implements the NEW method as default thus it is interesting to investigate how this new method works. Here we briefly compare these two bad pixel interpolation methods fixing the aperture settings at [4,6,9] as used before and adopting all default values for their parameters. We show in Table A.3 the pol:spec ratio of the total satellite spot fluxes for these two methods.

With the NEW method we find a weighted average of the pol:spec ratio of the total satellite spot flux of 1.03 ± 0.02 with a very similar flux variability as shown with the OLD method. We observe an increase of 1% with respect to the weighted average of the pol:spec ratio of

1.02 ± 0.02 from the OLD method. We find the default values in the new method too aggressive introducing great variations in the flux of HIP70931B, thus we cannot use it to better constrain the pol:spec ratio of the satellite spot flux. Exploring the parameter space of these methods is out of the scope of this study but we warn about the usage of the new method in very bright companions. This also makes the comparison of the satellite spot: companion ratio of the pol:spec ratios problematic.

It is instructive nevertheless to repeat the study of total satellite spot flux as a function of H magnitude for the targets. Figure A.5 shows the results where we recover very similar results as found with the OLD method before fitting a simple relation of the form $flux = 10^{-0.4(H+const)}$. We have $const = -15.15 \pm 0.10$ in polarimetry and $const = -15.13 \pm 0.07$ in spectroscopy mode within a 95% confidence interval.

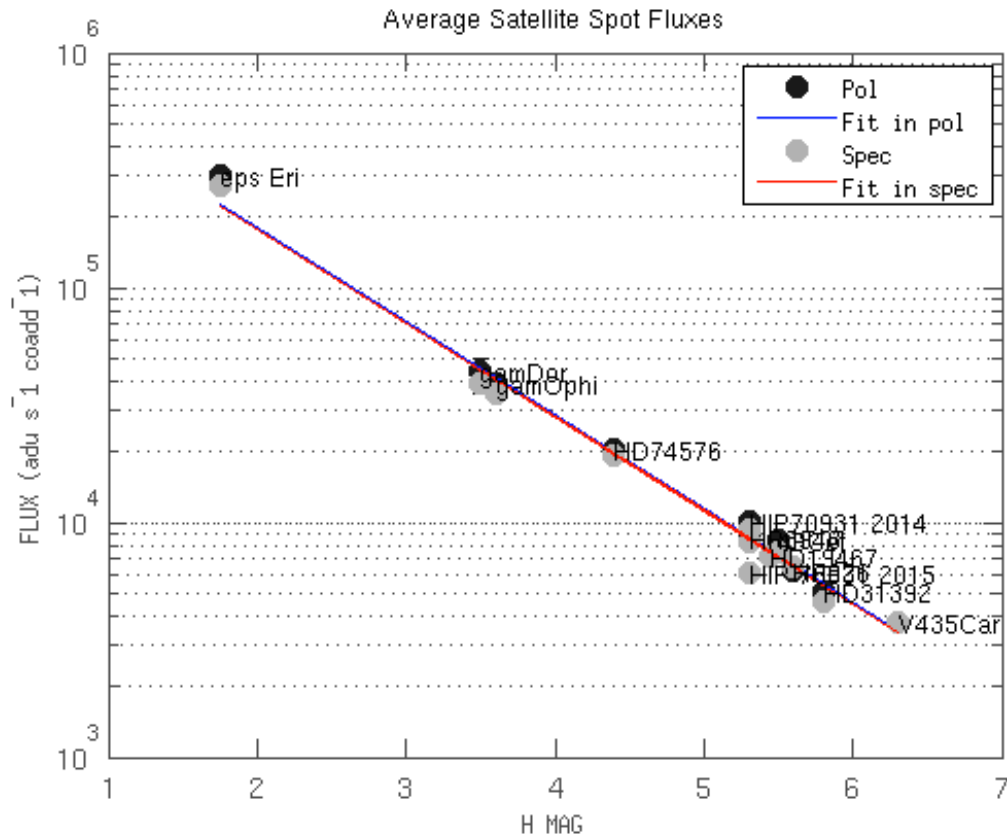


Figure A.5 Average total satellite spot flux as a function of H magnitude with an aperture of 4 pixels in spectroscopy (light gray) and polarimetry (black) dots using the NEW method for bad pixel interpolation in datacubes in polarimetry mode. The weighted fit to the data follows the expected relation between fluxes and magnitudes. Both fits are virtually identical.

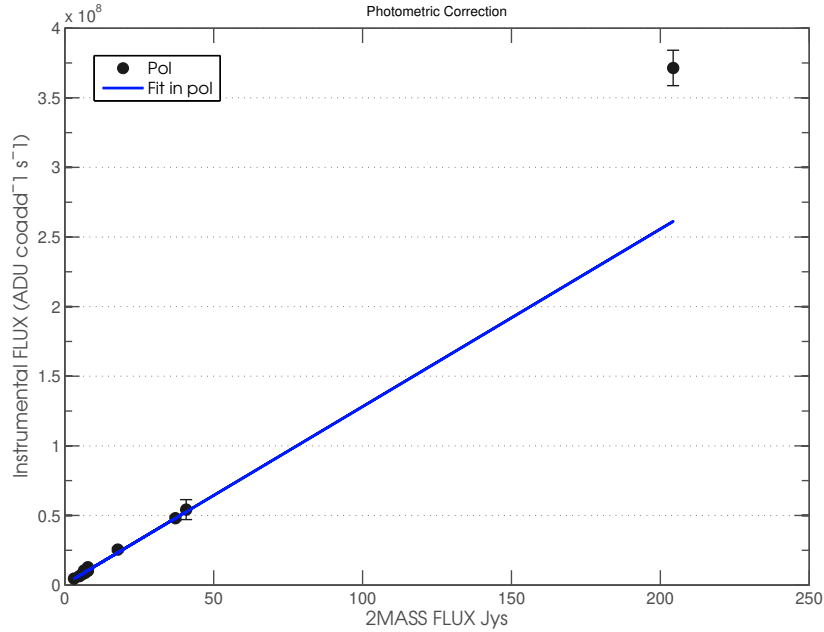


Figure A.6 Average total satellite spot flux as a function of 2MASS fluxes in Jy with an aperture of 4 pixels polarimetry (black) dots.

It is important to provide a way to convert the measured fluxes into calibrated units such as Janskys, or Jy. For each target, the grid ratio in H band 2.035×10^{-4} is used to calculate the measured star flux in H band from the mean satellite spot flux in each individual exposure. The mean value for the sequence is computed and adjusted by airmass and saved as *Flux* and the operation repeated for the remaining targets. Now, we fit the published 2MASS fluxes to the observations weighted on the uncertainties in the measured fluxes, computed as the standard deviation of the observations for each target. Figure A.6 shows the observed star flux as a function of 2MASS flux in Jy for the targets in this study whereby we obtain

$$Flux = a \times 2MASS F + b \quad (\text{A.2})$$

with $a = (1.28 \pm 0.17) \times 10^6 \text{ ADU coadd}^{-1} \text{ s}^{-1} \text{ Jy}^{-1}$ and $b = (6.0 \pm 1.0) \times 10^5 \text{ ADU coadd}^{-1} \text{ s}^{-1} \text{ Jy}^{-1}$. Now we can convert the measured fluxes into Jy by using the inverse relation with coefficients $a' = a^{-1} = (7.84 \pm 1.05) \times 10^{-7} \text{ Jy ADU}^{-1} \text{ coadd s}$ and $b' = -0.47 \text{ Jy ADU}^{-1} \text{ coadd}$

s.

A.2.2 Flat Fields

We investigated whether the throughput in each observing mode could be addressed by comparing raw and reduced GCAL flat fields taken on the same day. For this, sequences of GCAL flats in polarimetry and spectroscopy mode were secured, leaving 5 frames in between each sequence to mitigate persistence. Three sequences of three flats at 1.45 second each were taken in spectroscopy and polarimetry mode in July 29 2015 during the GPIES run. For each observing mode, datacubes were collapsed individually to 2D images storing the total flux. We followed the same reduction steps in GPI DRP as the ones outlined before to assemble the reduced cubes. Then for each 2-D collapsed flat a resistant mean was calculated on non-zero spaxels as to reduce the shift to lower values. The average in each sequence and the pol:spec ratio was calculated. A similar test was performed using raw Flats to check whether the reduction steps in GPI DRP could lead to the observed difference in flux measurements in polarimetry and spectroscopy mode. The mean of each raw image was calculated and the average across each sequence in polarimetry and spectroscopy mode saved. We present the results of raw flats in Figure A.7 and the reduced flats in Figure A.8

Raw flats appear dimmer at the beginning of every sequence in polarimetry and spectroscopy mode. This is also noticeable in the reduced flats in spectroscopy mode but not so in the reduced polarimetry flats. We excluded these first flats in our calculation and used the remaining two as we suspect this is related to the readout of the detector and not an intrinsic flux variation of the lamp.

We find 1.0145 ± 0.0002 as the average pol:spec flux ratio of raw GCAL flats. For the reduced GCAL flats, we find the average pol:spec flux ratio for the three sequences to be 1.044 ± 0.003 . We noticed the importance of setting up the right calibration files to be used. For instance, taking the first three polarimetry flats to calibrate the satellite spot locations will

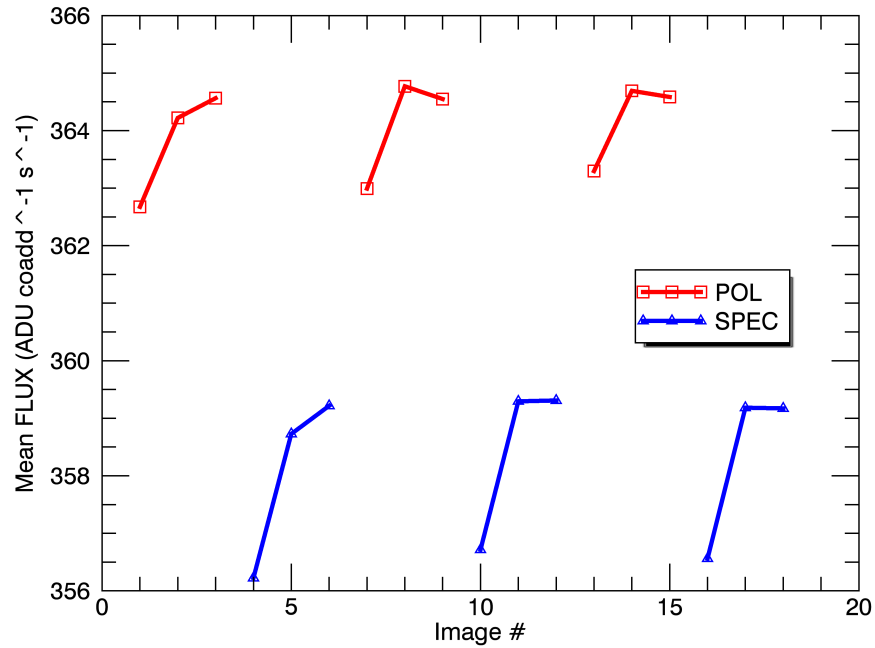


Figure A.7 Mean flux of raw GCAL Flats in spectroscopy (blue triangles) and polarimetry (red squares) mode in H band. The first frame of each sequence was excluded from our calculations.

create a systematic decrease in flux of 0.7% between the first and last flats. However the spectroscopy flats only showed a 0.2% variation in flux across the three sequences. We recover the same variation of 0.2% in the polarimetry flats by selecting all flats for the calibration of the satellite spot locations.

The adopted method for bad pixel interpolation (OLD | NEW) in `Interpolate bad pixels in cube` has a small, but noticeable effect in the reduction process of the flat frames. Moreover, by using NEW as the method for bad pixel interpolation yields on a average a reduction of 0.2% in the polarimetry flux measured thus giving an average ratio of 1.042. We used the same OLD method for bad pixel interpolation algorithm here to be consistent with the reduction steps used to measure the total satellite spot flux ratios. We also note that default settings in the new method are too aggressive and introduces large artificial fluctuations in HIP 70931B flux measurements.

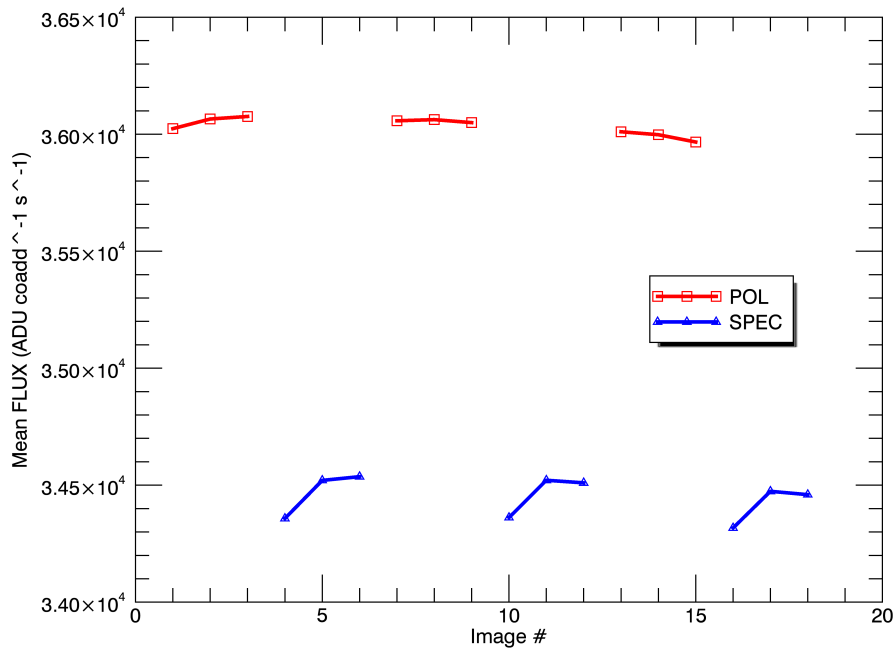


Figure A.8 Mean flux of reduced GCAL Flats in spectroscopy (blue triangles) and polarimetry (red squares) mode in H band. The first flat of each spectroscopy sequence was excluded.

Short term variability of total Satellite Spot Fluxes

We investigated the short term variability of the total satellite spot flux with the primitive developed for this study. Table A.4 shows the relative standard deviation (RSD) of the total satellite spot flux in spectroscopy and polarimetry mode at apertures of 4 and 5 pixels for each target. All in all, we observe an average variability of 4% in polarimetry and spectroscopy mode excluding γ Dor using the 4 pixel aperture and a value of 5% with the 5 pixel aperture.

Figures A.9, A.10 and A.11 are a good representation of the total satellite spot flux variability in polarimetry and spectroscopy mode. For these plots, we used an aperture of 4 pixels whereas the individual uncertainties were derived with Equation A.1.

Name	RSD _{pol} 4pix	RSD _{spec} 4pix	RSD _{pol} 5pix	RSD _{spec} 5pix
49Cet	0.05	0.04	0.09	0.04
ϵEri	0.03	0.05	0.06	0.07
V435 Car	0.03	0.02	0.06	0.02
HD 31392	0.06	0.06	0.05	0.05
γDor	0.1	0.1	0.09	0.08
γOphi	0.04	0.03	0.03	0.02
HD74576	0.06	0.03	0.04	0.04
HR 826	0.04	0.07	0.03	0.1
HR 6948	0.05	0.05	0.06	0.05
HD 19467	0.02	0.02	0.03	0.03
HIP 70931 ^a	0.04	0.03	0.08	0.06

Table A.4: Total satellite spot flux relative standard deviation (RSD) in spectroscopy and polarimetry mode with apertures of 4 and 5 pixels. ^a HIP 70931 observed in March 2014.

A.3 Conclusions

In this study we investigated the behaviour of raw and reduced flat frames to assess the throughput in polarimetry and spectroscopy mode of GPI. From the analysis of the raw flat frames we derived a mean pol:spec ratio of 1.0145 ± 0.0002 . This can be interpreted as a measurement of the physical throughput of GPI suggesting that the increment of 1.45% between the polarimetry and spectroscopy flats is a consequence of the different optical setups of GPI and sets a floor level for the observed ratios coming from the GPI DRP. Using the reduced flat frames, a mean pol:spec ratio of 1.044 ± 0.003 was found. In a different approach, we studied the total satellite spot flux to derive mean pol:spec ratios for each of the eleven targets in this study. The weighted average pol:spec ratio of the total satellite spot flux of all targets and the companion HIP 70931B is 1.03 ± 0.01 with the PSF method for datacube extraction in polarimetry mode. The short term variability of the total satellite spot fluxes for the sample of targets was found to be on average between 4% and 5% in polarimetry and spectroscopy mode. The current NEW method of bad pixel interpolation is in agreement with these findings. However without exploring other parameters in this method, we cannot use the bright companion HIP70931B to better constrain this result. We emphasize that this calibration is sensitive to the algorithm used

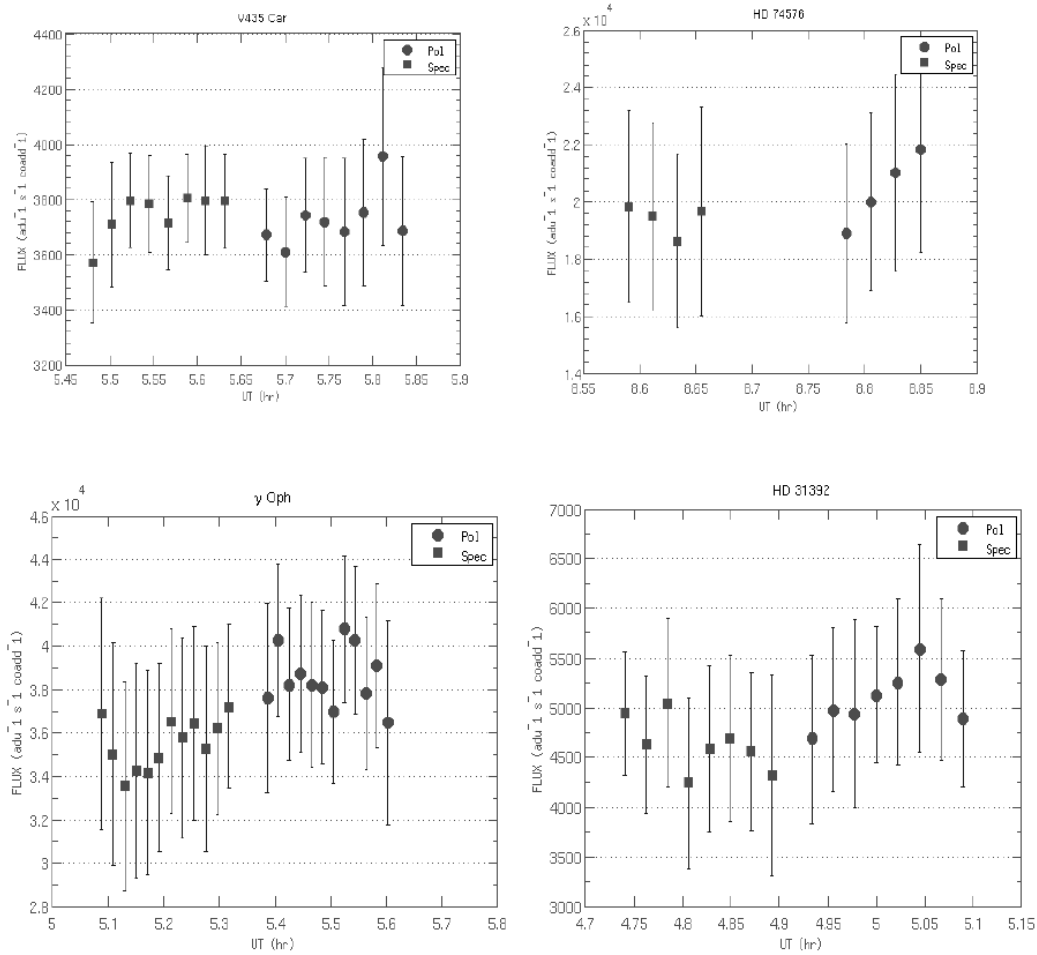


Figure A.9 GPI photometry in spectroscopy and polarimetry mode.

to extract the podc cubes and warn the user that variations of $\sim 12\%$ in polarimetry flux could be a consequence of using the 5×5 box method instead of the one used here. Both methods for bad pixel interpolation in polarimetry cubes yield similar results. Variations of 0.2% in flux are expected as a result of the preferred bad pixel interpolation algorithm and could drive the throughput in polarimetry mode 4.2% brighter as suggested by the reduced flat frames. We cannot rule out flux variations of $\sim 1\%$ in polarimetry mode due to flexure in the targets as also suggested from the reduced flat frames.

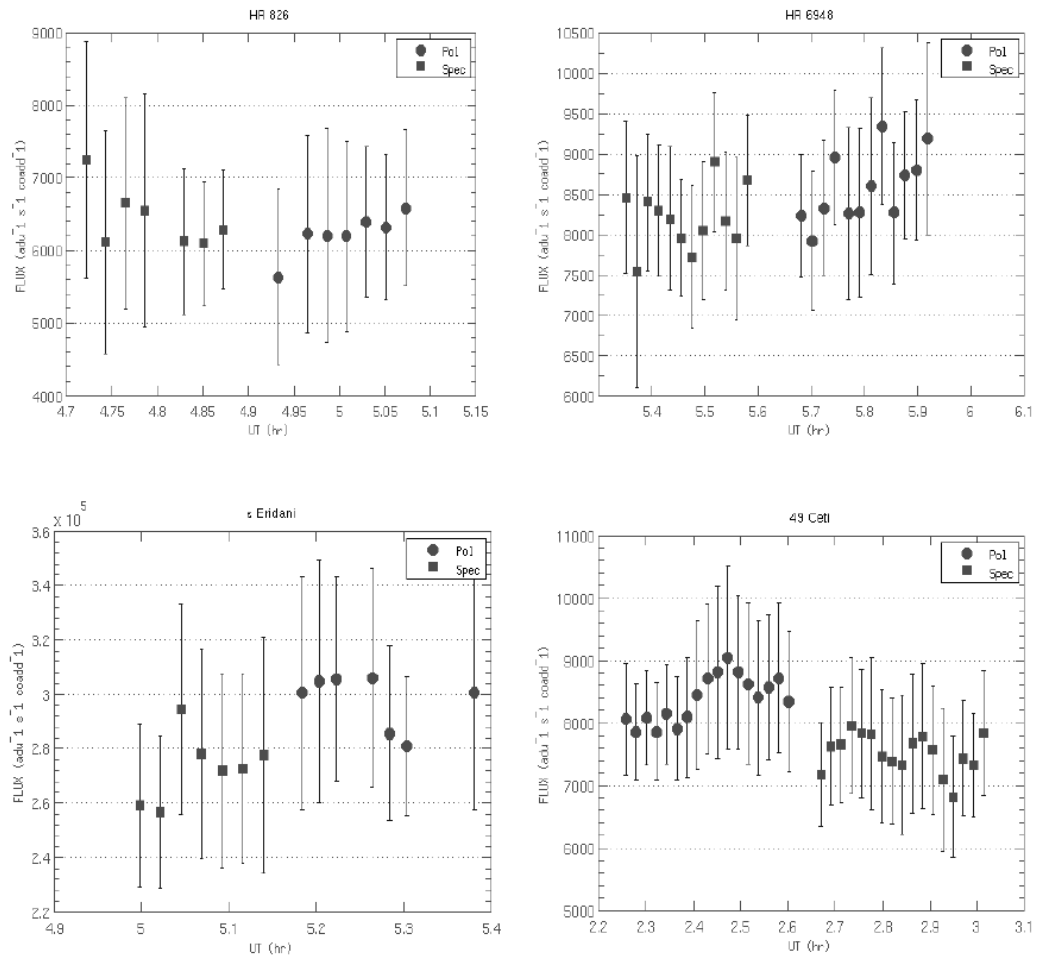


Figure A.10 GPI photometry in spectroscopy and polarimetry mode.

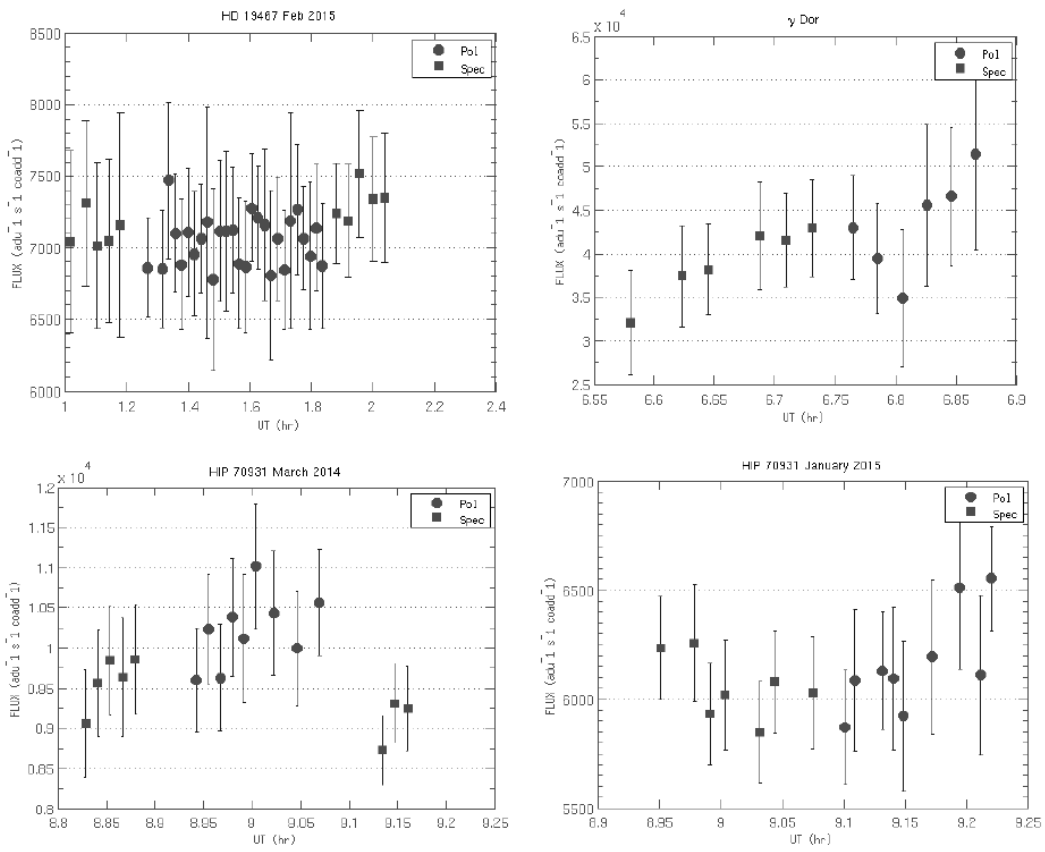


Figure A.11 GPI photometry in spectroscopy and polarimetry mode.

Curriculum Vitae

Name: Juan Sebastián Bruzzone

Post-Secondary Education and Degrees: Ph.D in Astronomy, 2014-2018
The University of Western Ontario
London, Ontario, Canada

M.Sc. in Planetary Science, 2012-2014
The University of Western Ontario
London, Ontario, Canada

B.Sc. in Physics option in Astronomy, 2000-2011
Faculty of Sciences, Universidad de la República
Montevideo, Uruguay

Related Work Experience: Graduate Research and Teaching Assistant
The University of Western Ontario, 2012-2018

Observer at Los Molinos Astronomical Observatory
Montevideo, Uruguay, 2006-2012.

Peer-Reviewed Publications:

- Revealing the Kuiper belt-analogue 46 AU debris ring around HD 141569A with GPI Polarimetry, **Bruzzone, J.S.**, Metchev, S., Duchene, G., Millar-Blanchaer, M., Wang, J. and the GPI team. *Submitted to the Astrophysical Journal.*
- An Active Collisional Cascade in the Old HD 157587 debris disk deduced from multi-band Gemini Planet Imager Polarimetry. **Bruzzone, J. S.**, Metchev, S., Duchene, G., Esposito, T. and the GPI team. *to be submitted.*

- A decadal survey of the Daytime Arietid meteor shower using the Canadian Meteor Orbit Radar, **Bruzzone, J.S.**, Brown P., R.J. Weryk and Campbell-Brown M.D., 2015, MNRAS 446, 1625-1640
- GPI observational calibrations XIV: polarimetric contrasts and new data reduction techniques, Maxwell A. Millar-Blanchaer, Marshall D. Perrin, Li-Wei Hung, Michael P. Fitzgerald, Jason J. Wang, Jeffrey K. Chilcote, James R. Graham, **Sebastian Bruzzone**, Paul R. Kalas, Proceedings of SPIE Vol. 9908, 990836 (2016)
- The HD 35841 Dust Ring Resolved with the Gemini Planet Imager, Tomas Esposito, Gaspard Duchene, Malena Rice, Paul Kalas, [.....], **Sebastian Bruzzone**, [.....], submitted to the Astrophysical Journal.
- Gemini Planet Imager observational calibrations XI: pipeline improvements and enhanced calibrations after two years on sky, Marshall D. Perrin, Patrick J. Ingraham, Katherine Brutlag Follette, Jerme Maire, Jason J. Wang, Dmitry Savransky, Pauline Arriaga, Vanessa P. Bailey, **Sebastian Bruzzone**, Jeffrey K. Chilcote, Rob de Rosa, Zachary H. Draper, Michael P. Fitzgerald, Alexandra Z. Greenbaum, Li-Wei Hung, Quinn M. Konopacky, Bruce A. Macintosh, Franck Marchis, Christian Marois, Maxwell A. Millar-Blanchaer, Eric Nielsen, Abhijith Rajan, Julien Rameau, Fredrik T. Rantakyro, Jean-Baptiste Ruffio, Kimberly Ward-Duong, Schuyler G. Wolff, Joe Zalesky, Proceedings of SPIE Vol. 9908, 990837 (2016)
- Observational calibration XII: photometric calibration in the polarimetry mode, Li-Wei Hung, **Sebastián Bruzzone**, Sebastian Bruzzone, Maxwell A. Millar-Blanchaer, Jason J. Wang, Pauline Arriaga, Stanimir Metchev, Michael P. Fitzgerald, Anand Sivaramakrishnan, Marshall D. Perrin, "Gemini planet imager ", Proceedings of SPIE Vol. 9908, 99083A (2016)
- Bringing The Moth to Light: A Planet-sculpting Scenario for the HD 61005 Debris

Disk, Esposito, Thomas M.; Fitzgerald, Michael P.; Graham, James R.; Kalas, Paul; Lee, Eve J.; Chiang, Eugene; Duchêne, Gaspard; Wang, Jason; Millar-Blanchaer, Maxwell A.; Nielsen, Eric; Ammons, S. Mark; **Bruzzone, Sebastian**; De Rosa, Robert J.; Draper, Zachary H.; Macintosh, Bruce; Marchis, Franck; Metchev, Stanimir A.; Perrin, Marshall; Pueyo, Laurent; Rajan, Abhijith; Rantakyr, Fredrik T.; Vega, David; Wolff, Schuyler, 2016, *The Astronomical Journal*, Volume 152, Issue 4, article id. 85, 16 pp.

- First Scattered-light Image of the Debris Disk around HD 131835 with the Gemini Planet Imager, Hung, L. W., and Duchêne, G. and Arriaga, P. and Fitzgerald, M.P. [.....] **Bruzzone, S.** [.....], 2015, *ApJ*, 815.
- Discovery and spectroscopy of the young jovian planet 51 Eri b with the Gemini Planet Imager, Macintosh, B. and Graham, J. R. and Barman, T. and De Rosa, R. J [.....] **Bruzzone, S.**, [.....], *Science*, 2015, 350, 64-67.
- Distribution of boulders and the gravity potential on asteroid Itokawa, G. Tancredi, S. Roland, **S. Bruzzone**, 2014, *Icarus* 247, 279290
- Size, shape, albedo, density and atmospheric limit of transneptunian object (50000) Quaoar from multi-chord stellar occultations. F. Braga-Ribas, ... **S. Bruzzone** [.....], 2013 *ApJ* 773 26 doi:10.1088/0004-637X/773/1/26
- Albedo and atmospheric constraints of dwarf planet Makemake from a stellar occultation. J L Ortiz, ... **S. Bruzzone** [.....], *Nature* 11/2012; 491(7425):566-9.
- 5088 TANCREDI: Rotation Period and Phase Coefficients. Tancredi G., **Bruzzone S.**, Roland S., Salvo R. *Minor Planet Bulletin*
- Stellar Occultations by TNOs: the January 08, 2011 by (208996) 2003 AZ84 and the May 04, 2011 by (50000) Quaoar, F. Braga-Ribas, ... **S. Bruzzone**, [.....], *EPSC Abstracts* Vol. 6, EPSC-DPS2011-PREVIEW, 2011, EPSC-DPS Joint Meeting 2011

- 2006 Observing Programs of the Observatorio Astronómico Los Molinos, G. Tancredi, S. Roland, R. Salvo, F. Benitez, **S. Bruzzone**, A. Ceretta, E. Acosta, Proceedings of Special Session on Astronomy in the Developing World, International Astronomical Union. Cambridge University Press, pp.71-76.

Publication in International Circulars

- 105 published reports to Minor Planet Center Circulars. Source: [Astrophysics Data System](#) Key: S. Bruzzone